

CHAPTER 1 – Introduction

1.1 MOTIVATION

The secretory pathway of eukaryotic cells is an important system facilitating the delivery of newly synthesized proteins, lipids, and carbohydrates to the cell surface. This transport is necessary for cell growth and homeostasis. Individual organelles including the endoplasmic reticulum (ER), Golgi apparatus, and plasma membrane (PM), provide a specialized environment facilitating the various stages of protein development, modification, sorting, and ultimately secretion. Secretory cargo is synthesized and assembled in the ER before being transported to the Golgi where it is further processed. Upon completion of Golgi maturation, the cargo is sorted and packaged into post-Golgi carriers that are responsible for transport of the cargo to its final destination. This directional transport of both newly synthesized and existing resident proteins is balanced by retrieval pathways that return membrane and selected proteins back to their compartments of origin.

Protein trafficking pathways are important to the study of cellular division, or mitosis. The Golgi apparatus has been shown to break down during the initial stages of mitosis and is later rebuilt in the two daughter cells (Lucocq et al., 1989; Lucocq et al., 1987; Maul and Brinkley, 1970). ER and Golgi membrane proteins are found in numerous dispersed vesicles in mitotic cells (Lucocq and Warren, 1987; Misteli and Warren, 1995). Investigation of interphase protein trafficking is important in not only understanding the partitioning properties of these Golgi resident proteins in mitotic cells, but also understanding the overall dynamics of mitosis.

The biotechnology industry has grown considerably since the early 1980s, led by advancements in the area of protein therapeutics (Henry, 2000). In recent years cells have become useful as practical, industrial-scale bioreactors (Cartwright, 1994). In particular, mammalian cell culture has been used to produce products including Herceptin™, a monoclonal antibody for treating breast cancer, and Vaqta™, an inactivated hepatitis A vaccine (Chu and Robinson, 2001). Another well known drug, Procrit®, is produced in Chinese hamster ovary cells and marketed by Amgen as an effective treatment for anemia resulting from cancer chemotherapy. Transgenic animal bioreactors have also been useful for the production of complex therapeutic proteins and are the most mature systems for expressing large amounts of the protein at a low cost (Houdebine, 2000; Houdebine, 2002a; Houdebine, 2002b; Van Cott and Velander, 1998). Protein secretion in the milk of these transgenic animals has become a useful source for the production of

recombinant protein pharmaceuticals (Soler et al., 2005). Our work is focused on understanding the mechanisms and pathways involved in the secretion of these proteins, both endogenous and recombinant. A better understanding may assist in the development of better strategies for producing recombinant proteins within these bioreactor systems.

Development of novel drug delivery strategies utilizing unique mechanisms is also currently a major area of interest as evidenced by the developing number of companies and new technologies available (Charman et al., 1999; Kaparissides et al., 2006). Conventional oral and intravenous routes of drug administration often do not provide ideal pharmacokinetic profiles, particularly involving drugs displaying a high degree of toxicity or narrow therapeutic widows. For these reasons, an emphasis has been placed on the development of new, innovative methods for the directed delivery of therapeutic agents. Toxins in particular have shown promise as potential vectors for directed intracellular drug delivery. The inherent ability of certain toxins to enter the cell and travel along existing secretory trafficking pathways have also made them useful in the study of these intracellular pathways. Increased knowledge about the mechanisms involved in secretory membrane transport will not only provide us with greater understanding of toxin infection but may also expose opportunities for the therapeutic use of these toxins as vaccinations or in the targeted elimination of cells. Our research has attempted to better understand these trafficking pathways using a quantitative approach to analysis.

Fluorescent microscopy has been a useful tool for the visualization and *qualitative* analysis of intracellular proteins for many years. However, with our work we have introduced a novel method for the *quantitative* analysis of intracellular protein distributions using fluorescent microscopy. The methods presented in the following chapters for the quantitative analysis of Golgi resident proteins are applicable for the study of other intracellular processes. The research presented in this dissertation is an excellent example of how engineering analysis can be used to better understand a basic biological process. Combining both disciplines furthers our understanding of current biological processes as well as increasing the possibilities for the discovery of new information.

1.2 OBJECTIVE

This research consists of two primary parts. The initial focus centered on understanding the distribution of Golgi resident glycosyltransferases between the ER and Golgi at steady-state.

Retrograde trafficking of these Golgi proteins has been demonstrated experimentally mandating the existence of a dynamic equilibrium between the Golgi apparatus and ER (Cole et al., 1996; Pelham, 2001; Storrie and Nilsson, 2002; Storrie et al., 1998). Our studies also included the development of a quantitative method for analysis of data collected using fluorescent microscopy (Rhee et al., 2005). The second part focused on the quantification of a unique Golgi resident protein that cycles in the late endosome bypass pathway. Using the published method of analysis and techniques developed during the initial project, we endeavored to (1) determine the anterograde and retrograde transport kinetics of this Golgi protein, (2) develop a compartmental model for the pH sensitive trafficking of this protein in the bypass pathway, and (3) investigate the spatial Golgi distribution of the protein during retrograde transport to the Golgi following endosomal exit.

This research lies at the interface of experimental cell biology and quantitative computational analysis. These experiments combined more traditional experimental biological approaches with more recent computational approaches to understanding cellular mechanisms. Additionally, development of a quantitative method of analysis validated the use of fluorescent microscopy as a quantitative tool for studying intracellular proteins.

1.3 SPECIFIC AIMS

Aim 1. Determine a quantitative process for analyzing fluorescent microscopy data. Use this process to determine the steady-state value of the ER pool of a specific subset of Golgi resident proteins for HeLa cells.

Aim 2. Quantify and characterize cycling rates of the Golgi resident protein GPP130 between the Golgi and endosomes

Aim 3. Spatial characterization of Golgi localized GPP130 during retrograde transport between the endosomes and the cis Golgi.

1.3.1 Aim1. Determine a quantitative process for analyzing fluorescent microscopy data. Use this process to determine the steady-state value of the ER pool of a specific subset of Golgi resident proteins for HeLa cells.

The Golgi apparatus forms the central hub of the secretory system and both anterograde and retrograde trafficking between it and the ER is critical for proper activity. A strong prediction of constitutive recycling between the Golgi apparatus and the ER is the existence of a steady-state pool of Golgi enzymes within the ER. We showed, using three approaches to quantifying Golgi enzyme levels in the ER versus Golgi apparatus, that the Golgi apparatus to ER ratio steady-state distribution was approximately 90:10. The methods used were: fluorescence microscopy (single plane widefield and confocal), analysis of electron micrographs of immunogold labeling of cryosections, and pool size estimations from kinetic modeling of Golgi apparatus to ER recycling. Previous fluorescent image analysis has used visual identification for determining protein distributions in the cell. Our analysis used a more quantitative approach involving calculated thresholds and deconvolution analysis. All experiments were done in the presence of cycloheximide to inhibit protein synthesis as a way to demonstrate whether or not enzyme distributions were metabolically stable. Based on our results, we concluded that a finite portion of Golgi enzymes resides in the ER at steady-state and that the outcome of quantifying this distribution is remarkably similar whether by electron microscopy, mathematical modeling or fluorescence microscopy through calculated threshold or deconvolution.

1.3.2 Aim 2. Quantify and characterize cycling rates of the Golgi resident protein GPP130 between the Golgi and endosomes

The early endosomal pathway has been studied in connection with viral entry into cells. Knockdown studies performed in the Linstedt laboratory (Puthenveedu et al., 2003) showed that the Golgi apparatus protein GPP130 mediated endosome to Golgi trafficking of Shiga toxin. Cells lacking GPP130 showed a significant delay of toxin transport to the Golgi consistent with a kinetic block during early endosome exit. Understanding of this unusual Golgi recycling pathway will contribute to the understanding of viral infection kinetics and the possible use of this pathway for drug delivery.

The drug monensin has been shown to increase intracellular pH, which in turn blocks protein exit from the endosomes and leads to an accumulation of GPP130 protein in these endosomes (Linstedt et al., 1997). The process is reversible and GPP130 returns to its steady-state distribution after drug washout. Using monensin to induce GPP130 redistribution, confocal fluorescent images stained for GPP130 at different time points and following deconvolution were

analyzed. Using data collected from the monensin redistribution and washout experiments, a two compartment kinetic model was used fit to the data and kinetic rates from the model determined for the forward and return rates of GPP130 between the Golgi and endosomes. Our data suggest that monensin not only inhibits endosomal exit to the Golgi, but also increases the rate of transport from the Golgi by almost 20 fold. Mechanisms behind this were not elucidated but suggest the presence of a pH sensitive rate-limiting step in the transport of GPP130 in between the Golgi and the endosomes.

1.3.3 Aim 3. Spatial Characterization of Golgi localized GPP130 during retrograde transport between the endosomes and the cis Golgi.

The specifics of how GPP130 traffics into the Golgi from the endosomes are still unknown. After exit from the endosomes, GPP130 has been shown to transport to its steady-state location in the cis Golgi (Linstedt et al., 1997). The goal of this aim was to determine if GPP130 was returned to the cis Golgi via the trans region after exiting the endosomes or if GPP130 trafficked directly to the cis Golgi. Using LSM510 laser scanning technology, a novel method for determining the distance between regions of high protein intensity was developed. The method involved determining the distances between GPP130 and both cis and trans Golgi markers from single plane images to determine the time evolution of GPP130 localization. Although quantification issues were identified, tenuous conclusions could be drawn based on the image analysis and further studies are needed.

1.4 DISSERTATION ROADMAP

Following a brief literature review presented in Chapter 2, our published work, to address Aim 1, is presented in Chapter 3. Research addressing Aims 2 and 3 is presented in Chapter 4. A discussion of all my previous work and suggestions for future work is described in Chapter 5. Finally, additional information concerning the electron micrograph analysis, stereology, pixel shift phenomenon, and general microscopy terminology described in chapters 3 and 4, is supplied in the appendices found at the end of the dissertation.

CHAPTER 2- LITERATURE REVIEW

In this chapter, background information will be presented that is relevant to the biological issues investigated in this dissertation. An overview of the secretory pathway is followed by a summary of the Golgi disturbing agents used. Finally, a review of both fluorescent and electron microscopy techniques is presented.

2.1 SECRETORY PATHWAY

The secretory pathway is a vital part of all eukaryotic cells and is responsible for protein folding, assembly, modification (i.e. glycosylation), sorting, and delivery (Figure 1). These mechanisms occur primarily in the endoplasmic reticulum (ER), Golgi apparatus, and various post Golgi organelles such as lysosomes, endosomes, secretory granules, and the plasma membrane (Watson P, 2005). Each compartment provides a specialized environment that facilitates the various stages of protein biogenesis.

2.1.1 ENDOPLASMIC RETICULUM

The endoplasmic reticulum (ER), an extensive network of continuous membrane stacks throughout the cytoplasm (Vertel et al., 1992), is comprised of the nuclear envelope, the rough ER, and the smooth ER. The rough ER, so named for the ribosomes that stud its surface, is a series of interconnected flattened stacks where some membrane and organelle proteins and almost all proteins secreted from the cell are synthesized. The smooth ER lacks the ribosomes characteristic of the rough ER and is responsible for the synthesis of fatty acids and phospholipids. Shortly after synthesis, proteins are translocated into the ER where they are subsequently folded. Misfolding or protein aggregation can result in retention of these proteins in the ER (Nishikawa et al., 2005). Properly folded proteins are packaged into coated vesicles for anterograde transport to the Golgi (Tang et al., 2005).

2.1.2 GOLGI APPARATUS

The Golgi apparatus, discovered in 1898 by Camillo Golgi, is the next station in protein maturation along the secretory pathway of eukaryotic cells (Farquhar and Palade, 1998). Debate as to the validity of the Golgi apparatus as an independent organelle was resolved with the introduction of cell fractionation and electron microscopy (EM). These quantitative techniques confirmed the role of the Golgi in protein glycosylation and secretion from the cell (Fleischer et al., 1969; Moore, 1974; Palade, 1975; Storrie, 2005). Immunofluorescence images indicate the Golgi to be a lacy, ribbon like structure ~5-7 μm in length, ~1-2 μm in width, and ~3-5 μm in

depth (Storrie et al., 1998). The functions of the Golgi include (1) protein glycosylation (Kornfeld and Kornfeld, 1985; Paulson and Colley, 1989; Roth, 1991), (2) sorting and delivery (Bonifacino and Glick, 2004; Watson P, 2005), and (3) recycling of receptors involved in endocytosis (i.e.mannose-6-phosphate receptor) (Carlton et al., 2004). These functions are performed by a population of proteins residing in three distinct regions of the Golgi apparatus: the cis Golgi/cis Golgi network (CGN), medial, and trans Golgi/trans Golgi network (TGN) (Mellman and Simons, 1992). Proteins localized to these sub-compartments are used as markers for their specific regions providing researchers with a novel way to study the maturation/ spatial progression of proteins traveling through the organelle.

Golgi resident proteins are categorized as belonging to either the trans-membrane or matrix families. Peripheral (matrix) proteins localized to the Golgi are thought to be responsible for the unique architecture of the organelle (Seemann et al., 2000). The best characterized of the matrix proteins are the fibrous, coiled-coil golgin family and the GRASP family of stacking proteins (Linstedt, 1999; Nakamura et al., 1995; Seemann et al., 2000). Recent research presents evidence for the role of matrix proteins in docking and tethering of trafficking vesicles and a role in cisternal adhesion through interactions with transmembrane proteins and lipids (Barr, 2005; Barr and Short, 2003; Linstedt, 1999; Nakamura et al., 1995; Seemann et al., 2000). The general assumption of matrix proteins as a static population stably associated with the Golgi is being challenged by increasing evidence of their dynamic interaction with both the cytosol and ER (Garcia-Mata et al., 2003; Mardones et al., 2006; Ward et al., 2001).

Posttranslational modifications, such as glycosylation, are the responsibility of individual glycosyltransferases (transmembrane family) distributed between Golgi compartments in a discrete gradient-like pattern. For example, while α 1,2 mannosidase I (MannI) exhibits a cis Golgi distribution (Balch and Keller, 1986), β 1,4-galactosyltransferase (GalT) has been shown to localize to the trans Golgi and TGN regions (Lucocq et al., 1989; Roth and Berger, 1982). These discrete distributions also define the role of the enzyme in the overall sequential modification of maturing proteins as they are received from the ER and mature through the Golgi. Most modifications occur in the medial Golgi compartment while the trans-Golgi/TGN aids in final glycosylation and sorting of plasma membrane, lysosomal, and secretory proteins to their respective final destinations. Distinct delineations of proteins between the compartments are not universal as appreciative overlap between cisternae for certain proteins has been shown, resulting in gradient like distributions (Axelsson et al., 2001). These proteins can be used as markers for a

broader region of the Golgi complex rather than specific cisternae. For example, ERGIC-53 is an enzyme localized to the cis Golgi and CGN. β 1,2 N-acetylglucosaminyltransferase I (NAGT I) and α -mannosidase II (Mann-II) are medial enzymes which tend to overlap some with the trans enzymes GalT and α -2,6-sialytransferase in distribution (Rabouille et al., 1995; Yang and Storrie, 1998). (Table 1).

With his work on the exocrine pancreas, George Palade established the vectorial transport of secretory vesicles through the ER and Golgi culminating in the export/excretion of the cargo molecules at the plasma membrane (Figure 1). Secretory proteins, membrane glycoproteins, and lysosomal enzymes are synthesized on polyribosomes and translocated to the ER where they undergo cotranslational and posttranslational processing. After exiting the ER, coated vesicles shuttle them to the cis Golgi where they are processed and sorted in a cis to trans manner. Sorting occurs in the trans cisternae or TGN where, for example, proteins marked with mannose 6-phosphate receptors are bound by lysosomal enzymes and delivered to endosomes to be degraded. Membrane and secretory proteins are sorted to the secretory or constitutive pathways in clathrin coated vesicles by exocytosis (Balch et al., 1994; Farquhar and Palade, 1998). Previous evidence has suggested that after exiting the TGN, secretory traffic is capable of traversing endocytic compartments on route to the plasma membrane (Ang et al., 2004; Futter et al., 1995; Hedman et al., 1987; Orzech et al., 2000). This co-operation between the biosynthetic and endocytic routes is not generally understood and may be partially due to the complexity of the endosomal population.

2.1.3 ENDOSOMES

Traditionally, endocytosis has been credited with the transport of hormones, nutrients, plasma membrane proteins, and ligands into the cell. A variety of endocytic mechanisms exist including phagocytosis, pinocytosis, and receptor-mediated endocytosis. After internalization the cargo can follow multiple pathways including (1) early endosomes (EE)/ sorting endosomes (SE), (2) lysosomes for degradation, (3) recycling endosomes (RE) for recycling back to the cell surface i.e. transferrin receptor, and (4) transcytosis from one plasma membrane to opposite plasma membrane in polarized cells (Figure 2). The interior endosomal environment is acidified by ATP-dependant proton pumps (Nishi and Forgac, 2002). Control of this interior pH can influence the trafficking route of the cargo and can aid in receptor/ligand dissociation (EE, RE) and lysosomal degradation, for example (Baravalle et al., 2005). More recent discoveries have begun to explore the role of endosomes in protein sorting (Ang et al., 2004; Lock and Stow, 2005), external stimuli response (Chow et al., 2002; Karylowksi et al., 2004), and cell signaling (Miaczynska et al.,

2004). Continued discovery of new endosomal functions only goes to illustrate the variety and complexity of the endosomal population present in eukaryotic cells. This complexity is increased in polarized cells, which interact with apical, and basolateral extracellular environments (Perret et al., 2005).

Several protein toxins produced by bacteria, including Shiga toxin, with intracellular targets ranging from kinases, to actin, to ribosomal subunits (Sandvig and van Deurs, 2002; Schirmer and Aktories, 2004) use endocytosis to enter the cell. In order to exert an effect, the toxins must also gain access to the cytosol. Most toxins use two main pathways for entering the cytosol; (1) direct transfer from the endosomes in response to low pH or (2) retrograde transport along the Golgi and ER before transfer to the cytosol (Figure 3). This exploitation of the endocytic machinery for entry into the cell and subsequent transport to the cytosol provides a useful tool for studying the retrograde transport routes of the secretory pathway. Shiga toxin is internalized via clathrin-dependant mechanisms (Sandvig et al., 1989) and transported from endosomes via the TGN/Golgi to the ER (Johannes et al., 1997; Kim et al., 1998; Sandvig et al., 1992). The existence of a bypass pathway connecting the EE/RE and TGN is supported by the rapid transport of Shiga toxin B-fragment as well as the transport of Golgi localized proteins TGN38 and furin (Chapman and Munro, 1994; Humphrey et al., 1993; Molloy et al., 1994).

2.1.4 MATURATION VERSUS VESICULAR TRANSPORT MODELS

Two opposing models have been put forward to explain the bi-directional vesicular traffic between the ER and Golgi (Figure 4). The classical vesicular-transport model views the Golgi as a stable stack of cisternae linked by transporting vesicles containing the secretory cargo. Specific subsets of enzymes residing in each cisternae act on the newly synthesized proteins and lipids in a step-wise manner as they are transported through the Golgi with the aid of small-coated vesicles (Palade, 1975; Pfeffer and Rothman, 1987). Simultaneously, retrograde transport recycles the coat proteins to earlier compartments for later use. Arguments for this anterograde vesicle model are based on the Golgi having a set structure, a fixed number of cisternae, and the presence of distinct populations of Golgi enzymes within these cisternae (Dunphy et al., 1985; Nilsson et al., 1993; Rambour et al., 1987; Roth and Berger, 1982).

Alternatively, cisternal maturation predicts the formation Golgi cisternae results from continuous ER derived vesicle fusion. The cisternae act as carriers for the newly synthesized proteins en route to the plasma membrane and are eventually consumed in the trans region thereby releasing

their cargo for transport to various post-Golgi destinations. Forward bulk flow is balanced by the presence of constant retrograde trafficking of Golgi resident enzymes (Glick and Malhotra, 1998; Pelham, 1998). In this manner, the maturing proteins are able to travel in an anterograde manner while the resident Golgi proteins are being recycled back for future use in protein modification and transport. A major finding in support of cisternal maturation was the discovery of transport of molecules too large to be contained in vesicular intermediates through the secretory system. In particular, studies involving the transport and modification of cell/wall scale formation in algae, a molecule almost as wide as the Golgi stack itself, illustrate the transport of cargo too large for vesicular transport alone (Becker et al., 1995; Brown, 1969). Other evidence includes the finding that Golgi transport vesicles contain resident Golgi enzymes that are depleted in secretory cargo suggesting their possible role in retrograde recycling (Love et al., 1998; Sonnichsen et al., 1996). Finally, evidence has been shown that illustrates, in living cells, cargo being carried from the ER to cis Golgi in structures larger than vesicles (Presley et al., 1997). It is suggested that this cargo accumulates in the cis cisternae and in so doing is consistent with the cisternal maturation model (Pelham, 1997). In reality, the transport of cargo through the Golgi from the ER is most likely some combination of both models but additional research is needed to work out the details (Orci et al., 1997; Ostermann et al., 1993; Pelham, 2001).

2.2 PROTEIN LABELING FOR VISUALIZATION

A variety of labeling techniques are available for visualizing intracellular proteins, including antibody staining and recombinant tagged proteins. Short descriptions of the imaging techniques used in this dissertation follow.

2.2.1 IMMUNOFLUORESCENCE

Immunofluorescence is a commonly used approach for the detection of intracellular proteins and can be used to study their localization and relative concentrations. Primary antibodies specific to an antigen are used in conjunction with fluorescently tagged secondary antibodies to identify the protein of interest (Figure 5). Antibodies can be made in the laboratory by injecting an animal (i.e. mouse, rabbit, sheep, goat) with the antigen. These repeated injections stimulate B cells, a special subpopulation of white blood cells responsible for antibody production, to secrete large amounts of antibody against the injected antigen (protein). Because a variety of B cells are stimulated, the isolated serum will consist of a mixed population of antibodies against various epitopes of the protein (polyclonal). Monoclonal antibodies recognize a single protein epitope and

are more specific, although harder to isolate and reproduce. Fluorescently conjugated secondary antibodies bind to the primary antibody (Figure 5) making it possible to detect the protein using methods such as fluorescent microscopy and western blotting. Antibody staining does, however require the cells to be fixed first. Although the development of recombinant proteins containing fluorescent protein domains (i.e. GFP) has introduced alternate methods for studying intracellular proteins, the wide range of available antibodies still makes immunofluorescence a commonly used technique.

2.2.2 GREEN FLUORESCENT PROTEIN (GFP)

Green fluorescent protein (GFP) was discovered in 1962 by Shimomura et al. and was isolated from the light-emitting organ of the jellyfish *Aequorea victoria* (Shimomura et al., 1962). Its ability to generate a highly visible fluorescent signal has made it a widely used marker for both gene expression and protein visualization in intact cells and organisms (Miyawaki et al., 2003; Stephens and Allan, 2003; Tsien, 1998). The GFP molecule has allowed specific labeling of biological molecules and cellular structures that can be detected using a variety of sensitive optical methods (Ehrhardt, 2003). The relatively non-invasive nature of the GFP molecules (beyond transfection) allows the researchers to observe and measure the molecules in living tissue and gather information on transient and dynamic events.

After the gene was cloned (Prasher et al., 1992), it was shown that GFP can be expressed in other organisms and remain capable of fluorescence (Chalfie et al., 1994; Inouye and Tsuji, 1994). This indicated that no jellyfish specific genes were required for the posttranslational synthesis of the chromophore (Tsien, 1998). GFP can be attached to almost any protein of interest and still fold into a fluorescent molecule without affecting the protein's function. One of the most successful applications of GFP has been its genetic fusion to host proteins in order to monitor their localization and movement (Tsien, 1998). The GFP gene is fused in frame with the protein of interest and the resulting chimera sequence is expressed in the organism of interest (example illustrated in Figure 6). This results in a new protein capable of fluorescence but still able to maintain its functions and localization capabilities. GFP has been fused to proteins of almost every major organelle of the cell including the plasma membrane (Barak et al., 1997; Hanakam et al., 1996; Marshall et al., 1995; Yokoe and Meyer, 1996), nucleus (De Giorgi et al., 1996; Hanakam et al., 1996; Lim et al., 1995; Rizzuto et al., 1996), ER (Miyawaki et al., 1997; Presley et al., 1997; Subramanian and Meyer, 1997), the Golgi apparatus (Presley et al., 1997), secretory

vesicles (Kaether and Gerdes, 1995; Lang et al., 1997), and mitochondria (De Giorgi et al., 1996; Murray and Kirschner, 1989; Rizzuto et al., 1996; Yano et al., 1997).

GFP is an 11-stranded β -barrel with an α -helix running up the center of the cylinder (Tsien, 1998). The chromophore is attached to the α -helix and resides in almost the exact center of the cylinder (Phillips, 1997; Yang et al., 1996). The emission spectrum of GFP peaks at 508 nm and it has two excitation peaks, at 395 nm and 470 nm. If exposed to fluorescent light for too long, the GFP molecule can become photobleached and lose its signal. However, most GFPs are relatively resistant to photobleaching, most likely due to the shielding of the chromophore by the structure itself (Cubitt et al., 1995; Swaminathan et al., 1997).

GFP, a 27 kDa protein, has been used widely as a fluorescent marker for proteins in living cells (Lippincott-Schwartz et al., 1998). These applications include quantitative imaging to measure the amount of protein localized to a particular site in the cell (Kahn et al., 1997; Niswender et al., 1995; Potter et al., 1996; Rhee et al., 2005), time lapse imaging to follow protein distributions (Kaether and Gerdes, 1995; Presley et al., 1997; Wacker et al., 1997), and photobleaching recovery experiments (Cole et al., 1996; Henkel et al., 1996). In particular, there have been many application opportunities for the GFP molecule in studying the secretory pathway, and in particular the Golgi apparatus. Presely et al. have used temperature sensitive VSV-G proteins tagged with GFP to look at the pre-Golgi intermediates and their relationship to the Golgi complex (Presley et al., 1997). Photobleaching and fluorescence recovery after photobleaching (FRAP) experiments have been used to study the diffusional mobility of Golgi resident proteins (Zaal et al., 1999). A problem that is often encountered when using GFP protein chimeras is the relatively large size of the GFP molecule interfering with the folding of the host protein (for example, relative sizes of truncated GalNAcT2 and GFP illustrated in Figure 6). When this occurs, transfected proteins can become trapped and accumulate in the ER. On a positive note however, only correctly folded GFP molecules will fluoresce. So, although there may be a large accumulation of unfolded protein in the ER, this pool will not affect fluorescent measurements. When using antibodies however, ER retention of incorrectly folded proteins can be an issue due to the fact that regardless of its conformational state, the antibody will bind to the protein epitope. For example, GalNAcT2-GFP cells stained for anti-GFP antibody showed a stronger ER staining pattern compared to live cell images (Figure 7).

2.2.3 VESICULAR STOMATITIS VIRUS (VSV)

Vesicular stomatitis virus glycoprotein (VSV-G) has unique properties that have made it a desirable model for studying the maturation and intracellular transport of membrane proteins. In particular, temperature sensitive mutants (i.e. ts045-VSV membrane protein) and VSV-G epitope tagged proteins (i.e. GalNAcT2-VSV) have been used to study the transport of proteins in the secretory pathway (Kreis, 1986; Rivas and Moore, 1989; Storrie et al., 1994). The VSV-G cytoplasmic domain, a 29 amino acid carboxyl-terminal sequence, has been shown to be required for normal transport to the cell surface (Rose and Bergmann, 1983). Alterations to this sequence affect the rate and extent of VSV-G delivery to the surface. The temperature sensitive mutant tsO45-G has been shown to accumulate in the ER at 39.5°C (Bergmann et al., 1981) and the trans Golgi-network (TGN) at 20°C (Saraste and Kuismanen, 1984) making it a useful tool for studying membrane transport kinetics. Additionally, transfected cell lines expressing VSV-G tagged proteins have been used to study the concentration and relative distributions of these proteins (Rhee et al., 2005; Röttger et al., 1998; Storrie et al., 1998). Unlike GFP, the VSV-G tag is not inherently fluorescent and requires primary and secondary antibodies to detect.

2.3 GOLGI DISTURBING AGENTS

Pharmacological agents, such as nocodazole, brefeldin A (BFA), monensin, and baflomycin, have proven useful in helping to understand the fundamental properties of the Golgi as an organelle. Perturbation of the Golgi function as a result of drug addition usually manifests itself as a loss of cisternal adhesion, Golgi dispersal, a block in secretion, or inhibition of vesicular traffic.

2.3.1 NOCODAZOLE

Within the interphase cell (Figure 8), the Golgi complex exists as a ribbon of interconnected stacks with a network of interconnecting tubules (Yang and Storrie, 1998). From this ribbon there is continuous trafficking of proteins to and from the ER. This trafficking between compartments is facilitated by microtubules. The microtubules and microtubule organizing center (MTOC) act to stabilize the juxtanuclear Golgi complex. The drug nocodazole acts to depolymerize the microtubules causing the Golgi stacks to fragment (Figure 9A). Golgi proteins leave the ER at a limited number of ER exit sites. Intact microtubules facilitate the transport of cargo to the Golgi. In the presence of nocodazole however, the microtubules are depolymerized and the Golgi

proteins cluster at these ER exit sites eventually coalescing into mini *de novo* Golgi stacks near the exit sites (Kasap et al., 2004; Storrie et al., 1998; Yang and Storrie, 1998).

Experiments involving Golgi protein chimeras (GFP, VSV-G, epitope tags) have shown that microtubules play an important role in the interphase mammalian cell. Key discoveries include finding that microtubules (1) are important in the juxtanuclear accumulation of Golgi complex intermediates which eventually assemble into the Golgi complex, (2) represent a direct pathway for retrograde recycling of Golgi proteins to the ER, and (3) provide evidence for the different cycling rates of various Golgi compartment resident proteins (Yang and Storrie, 1998). Evidence has been presented suggesting protein traffic between the Golgi and ER is a three stage process. The first step is budding from the scattered ER exit sites followed by coalescence of coated vesicles to form the intermediate compartment and finally the transport of these pre-Golgi structures to the Golgi complex. With regard to microtubules, these observations suggest an important role in providing the tracks for the congregation of these continuously forming Golgi intermediates. Agents that alter the distribution of these microtubules have a dramatic effect on the morphology and distribution of the Golgi apparatus. Nocodazole is an example of this reversible depolymerization of microtubules. Upon nocodazole addition, the Golgi separates into fragments that appear as short, stacked cisternae in EM micrographs (Yang and Storrie, 1998). The idea that upon microtubule depolymerization, the Golgi ribbon separates and the Golgi fragments slowly scatter to the cell periphery fails to account for the dense cytoplasmic medium in which they would have to travel. A different mechanism suggested is that upon microtubule depolymerization, the Golgi components redistribute to the ER exit sites where functional Golgi stacks are reformed.

Similarly, during mitosis of mammalian cells, the Golgi apparatus and ER undergo extensive fragmentation. This fragmentation is thought to help in the partitioning of the organelles between the daughter cells (Warren, 1993). The Golgi is converted into vesicles and short tubules that are dispersed throughout the cell (Jesch and Linstedt, 1998). After mitosis is completed, the Golgi quickly reassembles. The pathway of Golgi inheritance is not completely understood. Debate exists as to whether the Golgi breaks down directly and is inherited as fragments between the daughter cells or if the Golgi collapses into the ER only to reform after cell division is complete (Cole et al., 1996). Nocadazole provides a useful tool for studying the Golgi architecture during mitosis as it causes the Golgi to fragment in a similar manner as seen during mitosis.

2.3.2 BREFELDIN A

Brefeldin A (BFA) is a metabolite of the fungus *Eupenicillium brefeldianum*. BFA reversibly blocks protein transport from the ER to the Golgi (Klausner et al., 1992; Pelham, 1991) and has also been shown to block secretion, vesicular assembly, antigen presentation, viral assembly and budding. These changes usually result in morphological changes, including the collapse of the Golgi. The mechanism of action of BFA is believed to involve an interference with ADP-ribosylation factor (ARF) which functions in the association of the coat proteins with the membrane (Randazzo et al., 1993). In a study by Lippincott-Schwartz et al. BFA was shown to cause the Golgi resident protein mannosidase II to redistribute into the ER (Lippincott-Schwartz et al., 1989). It was also shown that VSV-G proteins undergo retrograde transport from the Golgi to the ER in the presence of BFA (Ivessa et al., 1995; Lippincott-Schwartz et al., 1989). Although Golgi morphology is dramatically disrupted during BFA treatment, it has been proven that the vesicular and tubular remnants of the Golgi remain after treatment and retain some of their function (Hendricks et al., 1992; Hidalgo et al., 1992) (Figure 9B).

2.3.3 MONENSIN AND BAFILEOMYCIN

Monensin is a carboxylic ionophore known to affect the Na⁺/H⁺ exchange of intracellular compartments, such as the Golgi and endosomes, causing an increase in their luminal pH (Mollenhauer et al., 1990). The exact nature of how the drug acts is till unknown. Its hydrophobicity allows it to be easily incorporated into biological membranes (Pressman, 1968) where it exchanges protons for Na⁺. Osmotic swelling accompanies the ion exchange, manifesting itself in light micrographs as dilated ring-like structures (Mollenhauer et al., 1990; Tartakoff and Vassalli, 1977). The ability of monensin to block secretion at the cellular level is also believed to be related to the breakdown of acidification mechanisms (Mollenhauer et al., 1990; Tartakoff, 1983; Yamashina, 1995). Golgi phosphoprotein of 130 kDa (GPP130), a cis Golgi integral membrane protein, has been shown to accumulate in early endosomal structures during monensin treatment, suggesting a pH-sensitive endosomal exiting mechanism and supporting the presence of an underlying cycling pathway between the biosynthetic and endocytic pathways (Bachert et al., 2001; Linstedt et al., 1997; Puri et al., 2002). Additionally, this continuous cycling of certain Golgi resident proteins between a steady-state Golgi distribution and post-Golgi intermediates is further supported by observations of monensin induced redistribution of other Golgi localized proteins, GalT, α1,3 fuc-T6, TGN 36/48 (Puranam et al., 1993) (Figure 9C). Similar endosomal accumulations have been demonstrated for clathrin mediated endocytosed toxins in the presence of monensin. Whether this is the result of a direct

effect on the toxin or a consequence of neutralized pH is still under investigation (Marnell et al., 1982; Orlandi et al., 1993).

Similar to monensin, the pH disrupting drug bafilomycin causes the reversible redistribution of GPP130 to early endosomal structures while blocking secretion from the cell as evidenced by studies involving VSV-G and Semliki forest virus (SFV) proteins. However unlike monensin, bafilomycin neutralizes luminal pH through the inhibition of vacuolar ATPases (Moriyama and Nelson, 1989).

2.4 MICROSCOPY

Microscopy has seen vast improvements over the last hundred years, from the introduction of phase contrast to the development of confocal imaging to the more recent introduction of Fluorescence Resonance Energy Transfer (FRET) for studying protein-protein interactions (Reviewed in Presley, 2005). With these advances has come a better understanding of the cellular processes that elude the human eye. Issues plaguing early microscopists, such as optical aberrations, blurred images and poor lens design, are continuing to be resolved with the introduction of new techniques like high-resolution objectives and laser scanning technologies, to name a few (Davidson MW; Michalet et al., 2003). Just in the past decade we have seen a rapid development of fluorescent techniques, advances in digital imaging, and improvements in optical microscopy. All of these advances combined have helped to propel the field of cell biology forward and help researchers gain a better understanding of basic cellular processes.

2.4.1 FLUORESCENT MICROSCOPY

Fluorescent microscopy, in particular, has become an important non-invasive tool for the study of cell structure and function. It allows the researcher access to information about the dynamics of a cellular environment *in vivo*. By observing the cell under normal physiological conditions, understanding of intracellular mechanisms can be studied without changing the conformation and structure of the cell itself (Saino and Satoh, 2004). Advances in optical (non-fluorescence, transmitted) microscopy have been the results of imaging innovations such as phase contrast, Nomarski's interference (differential interference contrast, DIC), and Hoffman's contrast (Davidson MW; Michalet et al., 2003). With the development of immunocytochemistry and the ability to do live cell imaging, fluorescence microscopy has become an extremely useful laboratory technique.

Fluorescence is the result of a three-stage process, excitation, excited-state lifetime, and emission (Figure 10). Fluorescent probes are designed to illuminate an area of interest for visualization using a fluorescent microscope. Excitation of the probe occurs when an external source, such as an ultraviolet lamp or laser, supplies a photon of energy that is absorbed by the probe. This creates an electronic singlet state that lasts for a finite amount of time, usually 1-10 nanoseconds (Michalet et al., 2003). At emission, a photon of energy is emitted at a longer wavelength, due to the partial dissipation of energy during the excited state. For example, the green fluorescent protein (GFP) is excited at 488 nm and has a major emission peak at 508 nm. Once the fluorophore has returned to its ground state, the excitation process may begin again. This repeatable process allows for high sensitivity of the fluorescent signal. One caveat when using fluorescent probes is the need to avoid photobleaching, a phenomenon caused by extended high-intensity illumination. Photobleaching is the irreversible destruction of the excited fluorophore and can be avoided by maximizing the detection properties of the microscope while simultaneously reducing the illumination intensity.

Fluorescence microscopes require an excitation source, wavelength filters that isolate emission and excitation photons, and a detector that captures and translates the emission into a measurable output (Figure 11). An important requirement to consider when using fluorescence microscopy is the background fluorescence. Background can detract from the actual signal and may occur from endogenous surroundings (auto-fluorescence) or non-specific binding of the fluorophore. The signal-to-noise ratio can also cause complications in the detection of the fluorescence intensity. Increasing the collection efficiency can help to increase the signal-to-noise ratio (Michalet et al., 2003).

Airy discs are the small circular diffraction discs that are projected onto the image plane (Davidson MW) (Appendix 4). The resulting image at the eyepiece is actually a combination of Airy discs perceived as light and dark regions. The highest resolution a microscope can achieve between two points is when the center spots of nearby airy discs can be distinguished from one another. When the two dark center spots overlap considerably, the details represented by these two discs are not resolved and they appear as one unit. Higher numerical aperture lenses capture more diffracted discs therefore creating smaller disc sizes and better resolution. Numerical aperture is defined as the light acceptance angle of the objective, which in turn determines the light gathering power and resolving power of that objective. A higher numerical aperture results

in a larger cone of light being admitted into the lens. This larger cone of light allows more diffraction patterns of the airy disc to be captured, resulting in a higher resolving power of the lens and more available information about the sample. Another advantage of using a high numerical aperture is the increase in light allowed into the lens generally produces brighter images. When light travels through the components of an optical system (i.e. condensor, filter, objective), the image is distorted and convolved by the optical system's point spread function (PSF). This PSF describes the manner in which the light of a point source is rendered by the optical system. Convolution can result in blurring and distortion of the original image, but is reversible using deconvolution. Deconvolution is the recovery of an object from an image that is degraded by blurring and noise (Landmann, 2002; Wallace et al., 2001). If the PSF is known, the majority of the convolution can be undone mathematically and the original shape of the object restored. The improvement due to mathematical deconvolution of an image is readily apparent in Figure 12.

Because the resolving power of a microscope is more limited in the axial versus lateral direction, the results of deconvolution are most dramatic along this axis. There are multiple ways to deconvolve an image, including the maximum likelihood estimation (MLE) used by the Huygens Essential software, a software package used in the research described in this dissertation. This method estimates the objects distribution with the highest likelihood of having produced the output image, while taking into account the nature of the noise and imaging properties of the microscope. In order for deconvolution to be affective, the images must be properly oversampled per Nyquist criteria. The Nyquist criterion determines the minimum sampling density necessary to capture all available information from the microscopic sample. Nyquist determined that the specimen signal must be sampled at least 2 times its highest spatial frequency (Nyquist, 1928; Webb RH, 1995). If this criterion is not met, undersampling can give rise to artifacts such as fringes and jagged edges. Therefore, when using deconvolution software, proper image sampling per Nyquist is essential.

2.4.2 CONFOCAL MICROSCOPY

Confocal microscopy, both spinning disk and laser scanning (LSM), offers several advantages over conventional widefield microscopy including reduced background, serial sectioning (Figure 13), and depth of field control. Using both the three-dimensional (3-D) and four-dimensional (3-D with time as fourth dimension) aspects available with confocal technologies, researchers have investigated motion/dynamics of organelle structures over time, protein-protein interactions,

membrane diffusion, and specific protein locations, to name a few (Bevis et al., 2002; Brismar et al., 1995; Egner et al., 2004; Elsner et al., 2003; Haustein and Schwille, 2004; Kreitzer et al., 2003; Stephens and Allan, 2003; Storrie et al., 1994). The key feature of confocal microscopy is the use of spatial filtering techniques to exclude out-of-focus light contributed by adjacent focal planes. A pinhole is used to block light from nearby focal planes resulting in reduced background emission while providing a more accurate visualization of sub-cellular membranes, vesicles, and organelle systems within eukaryotic cells (Zemanova et al., 2003). In addition, high numerical apertures used to focus the excitation light and sensitive detectors, i.e. photomultiplier tubes, combine to make confocal microscopy a useful technique for studies involving multiple fluorescing samples, small quantities (as little as femtoliter volumes), and fluorescence photobleaching (Zemanova et al., 2003).

Scanning confocal systems allow simultaneous imaging of multiple probes. The sample is illuminated in a point-by-point manner that provides the precision necessary for photobleaching experiments, but also limits the acquisition speed. Also, the number of laser lines available limits the excitation wavelengths available and switching between beams is slow which also affects the rate of acquisition. Alternatively, spinning disk confocal microscopes incorporate a rotating array of microlenses and pinholes to focus illumination and eliminate out-of-focus signal. A charge coupled device (CCD) camera captures the light from all the pinholes simultaneously increasing the rate of acquisition while reducing the photodamage to the sample. (Reviewed in Stephens and Allan, 2003).

Emerging confocal technologies, such as 4Pi and total internal reflection fluorescence microscopy (TIRF), continue to push the limitations of fluorescence microscopy steadily increasing our knowledge of the secretory pathway and the Golgi apparatus in particular (Axelrod, 1989; Egner et al., 2004; Lang et al., 1997).

2.4.3 ELECTRON MICROSCOPY

Electron Microscopy (EM) is an established high-resolution technique for the quantification and visualization of sub-cellular organelle and protein distributions. Using EM, the relationship between proteins and substructure of intracellular compartments has been investigated (Koster and Klumperman, 2003). Sample preparation usually involves (1) cell immobilization by either cryofixation or more traditional chemical fixation, (2) sectioning of the sample (usually cryosectioning), (3) followed by protein labeling and imaging. Colloidal gold particle conjugated

antibodies are the preferred method of labeling for immunoEM (antibody staining electron microscopy imaging) experiments. The availability of different gold particle sizes allows several protein subpopulations to be labeled and separately identified based on particle size. Using gold particle quantification in conjunction with stereological techniques (Appendix 1), it is possible to determine relative protein distributions, total protein concentrations, and specific spatial compartmental distributions (i.e. cis vs medial vs trans Golgi) (Koster and Klumperman, 2003). Drawbacks of this microscopy technique include cell destruction and the inability to collect real time data. Although fluorescent microscopy overcomes these specific limitations, it is at the expense of reduced resolution (best light microscope resolution ~ 200nm versus EM resolution < 1nm).

Table 1. Examples of Golgi Associated Proteins

LOCATION	PROTEIN	FAMILY
<i>cis</i> Golgi/ CGN	General vesicular transport protein (p115)	transmembrane
	Golgi Phosphoprotein of 130 kDa (GPP130)	transmembrane
	α 1,2 Mannosidase I (Mann I)	transmembrane
	ER-Golgi Intermediate Compartment protein of 53 kDa (ERGIC-53)	transmembrane
	Golgi Matrix protein of 130 kDa (GM130)	matrix
<i>medial</i> Golgi	β 1,2 N-acetylglucosaminyltransferase (NAGT I)	transmembrane
	α 1,3-1,6 Mannosidase II (Mann II)	transmembrane
	Golgi Reassembly Stacking protein of 55 kDa	matrix
<i>trans</i> Golgi/ TGN	β 1,4 galactosyltransferase (GalT)	transmembrane
	α 2,6 sialytransferase (SialylT)	transmembrane
	Rab6	GTP-binding protein
	N-acetylgalactosaminyltransferase-2 (GalNAcT2)	transmembrane

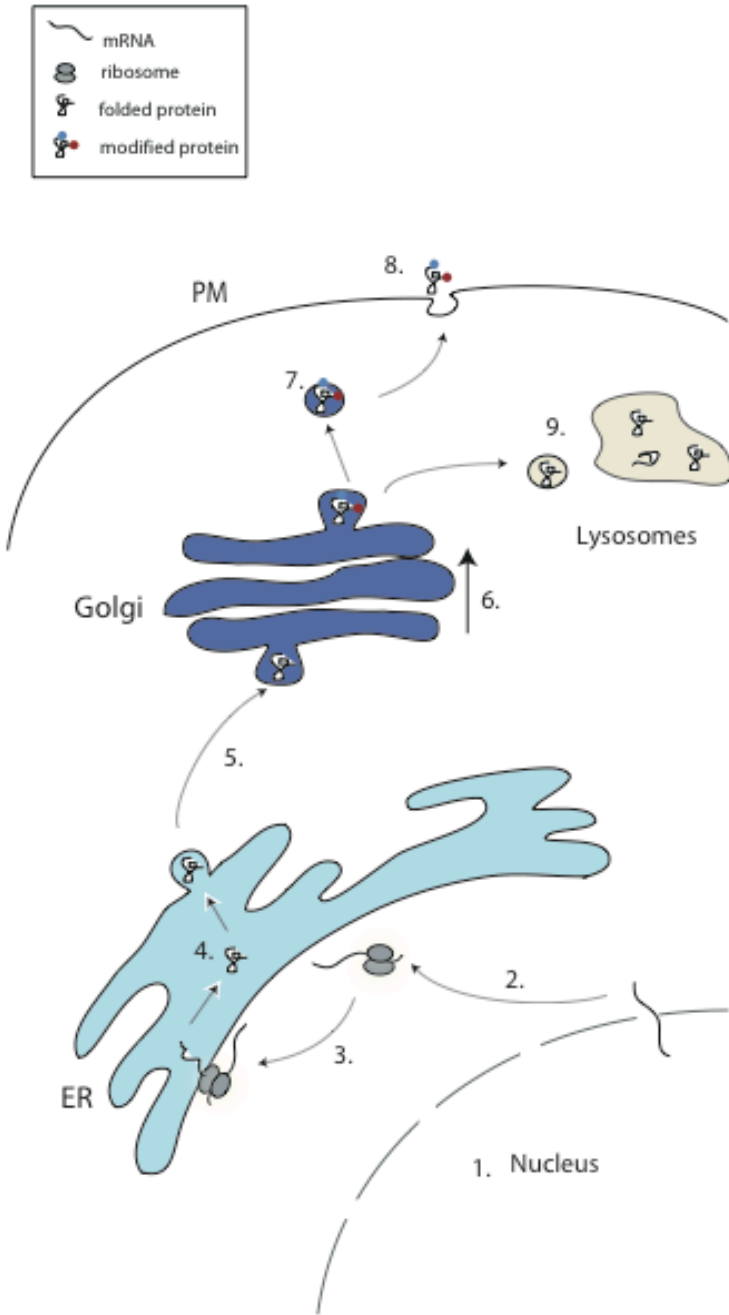


Figure 1. Secretory Pathway in Eukaryotic Cells. DNA is transcribed into RNA in the nucleus of the cell (1). After transcription, mRNA leaves the nucleus and enters the cytoplasm where it is bound by ribosomes (2). These ribosomes attach to the rough endoplasmic reticulum (ER) where they facilitate cotranslational transport of the protein into the ER lumen (3). After the protein is folded into its final conformation (4), it exits the ER and it transported to the Golgi (5). Enzymes

(Figure 1 continued)

localized in the Golgi are responsible for modification of the protein as it travels from cis to trans cisternae (6). These mature proteins can then be transported to the plasma membrane (PM) for secretion (7,8) or to other post-Golgi structures such as lysosomes for degradation (9).

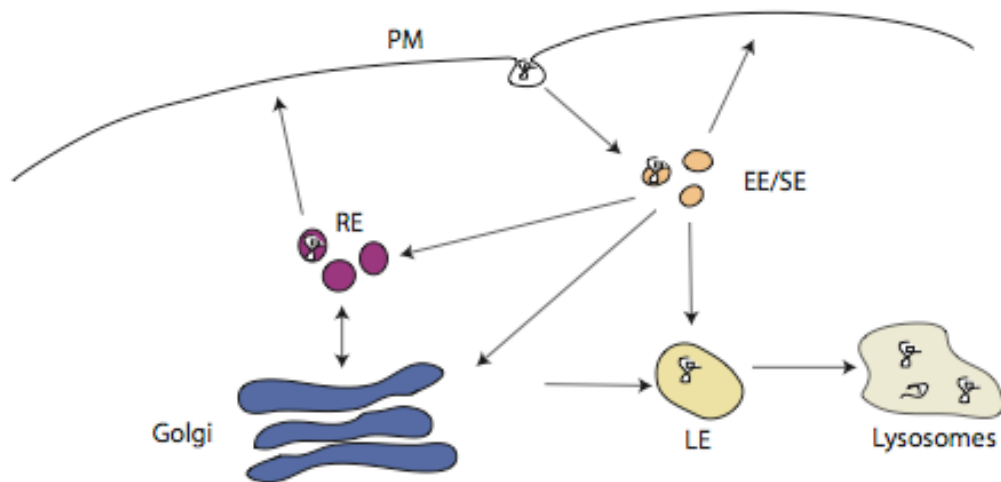


Figure 2. Endosomal Sorting. Ligand-receptor complexes from the plasma membrane (PM) internalized into early endosomes (EE)/sorting endosomes (SE) are separated for subsequent sorting. The dissociated receptors are often sorted to the recycling endosomes (RE) for transport back to the surface. Ligands can be transported to (1) the late endosomes (LE) before being sent to the lysosomes to be degraded, (2) the recycling endosomes for transport to the PM or Golgi, (3) the Golgi directly, a pathway used by many toxins, and (4) the PM for secretion.

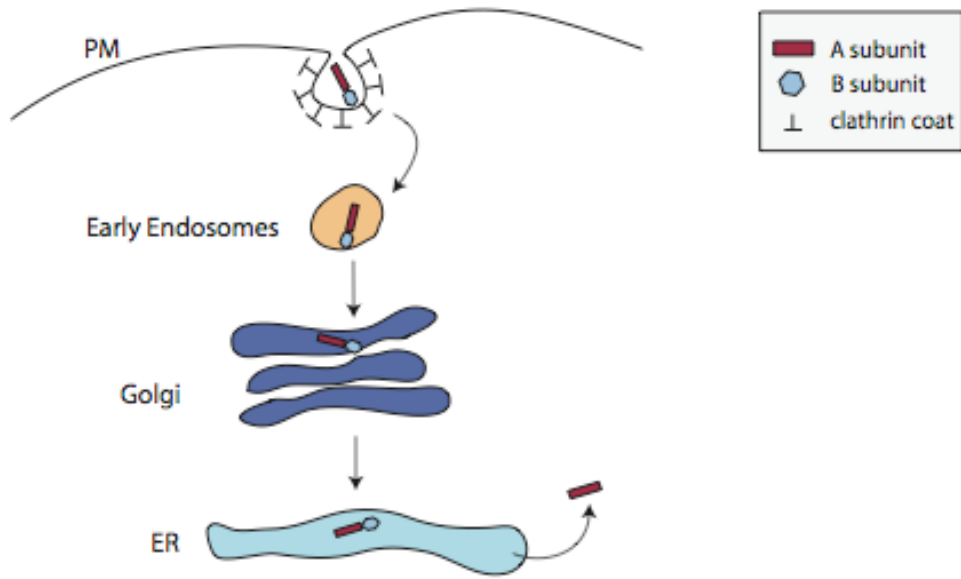
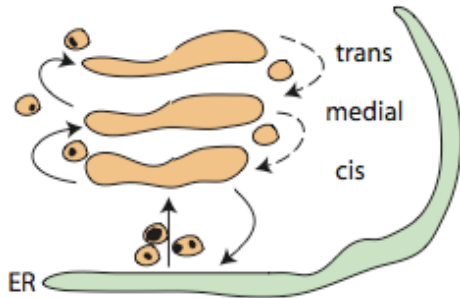


Figure 3. Shiga toxin Internalization Pathway. Shiga toxin, a bacterial toxin, binds to the cell before being endocytosed in clathrin-coated pits. It undergoes retrograde transport from early endosomes to the Golgi before traveling to the endoplasmic reticulum (ER). Shiga toxin consists of two subunits, A and B. The B subunit binds a receptor on the cell surface facilitating endocytosis while the enzymatically active subunit, A, is translocated from the ER lumen to the cytosol.

A. Vesicular Transport Model



B. Cisternal Maturation Model

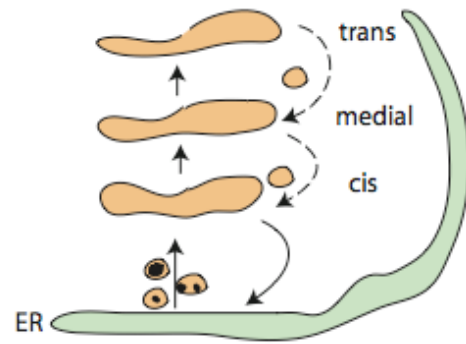


Figure 4. Transport Models for the Golgi Apparatus. In the vesicular transport model, small coated vesicles are used to transport cargo between the essentially stationary Golgi cisternae. Each stable cisterna has a fixed composition of resident enzymes. The cisternal maturation model uses vesicles for the retrograde recycling of resident Golgi enzymes while the cisternae act as bulk carriers for the cargo transporting through the Golgi. New cisternae are formed at the cis Golgi face with each round of cargo transport

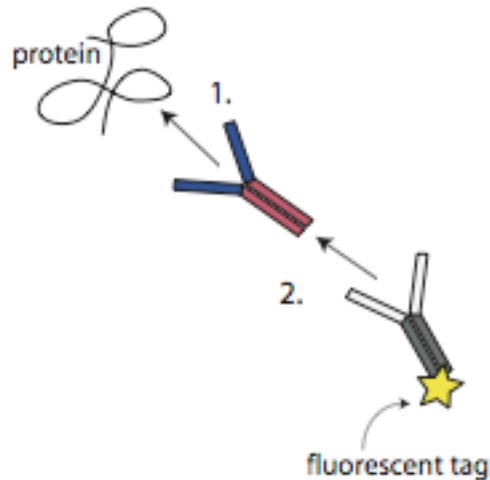


Figure 5. Antibody Detection. (1) Primary antibodies directed against a small epitope of the protein of interest bind to the protein specifically if that portion is accessible. (2) A secondary antibody designed to recognize the conserved region of the primary antibody is conjugated with a fluorescent tag making it possible to visualize the protein using fluorescent microscopy.



Figure 6. GalNAcT2-GFP protein. Truncated stem region of GalNAcT2 protein (338-bp fragment, (Storrie et al., 1998)) was fused to the NH₂ terminus of the GFP protein (~27 kDa (Tsien, 1998)).

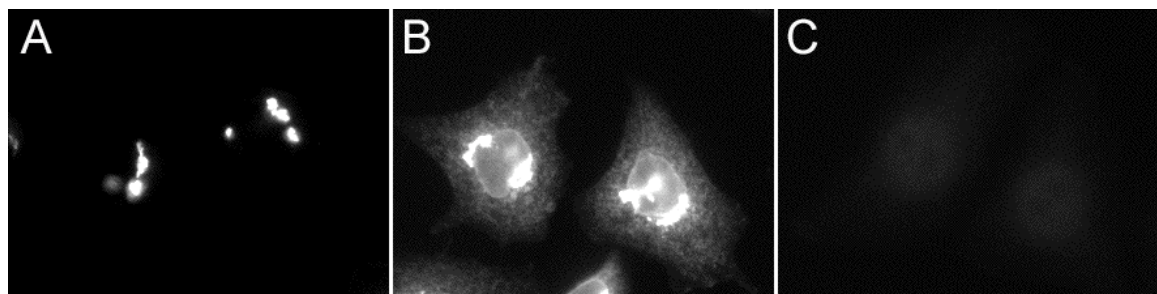


Figure 7. GFP Protein Distribution. Cells stably transfected to express GalNAcT2-GFP (A, B) exhibit different ER staining patterns depending on the method used to visualize the protein. Live cells imaged using a fluorescent microscope (A) have a weaker ER signal compared to cells stained with anti-GFP antibody (B). This increased ER signal is due in part to the non-specific antibody background of the antibody (C, anti-GFP staining of wild-type HeLa cells) and due in part to the antibody recognition of misfolded GalNAcT2-GFP protein retained in the ER.

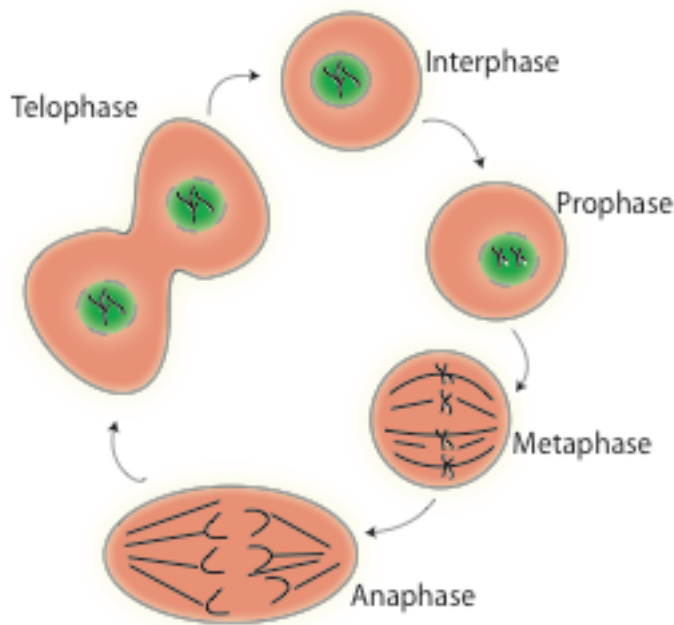
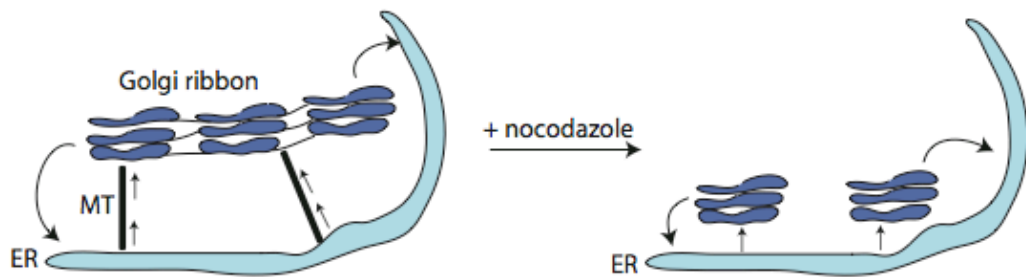
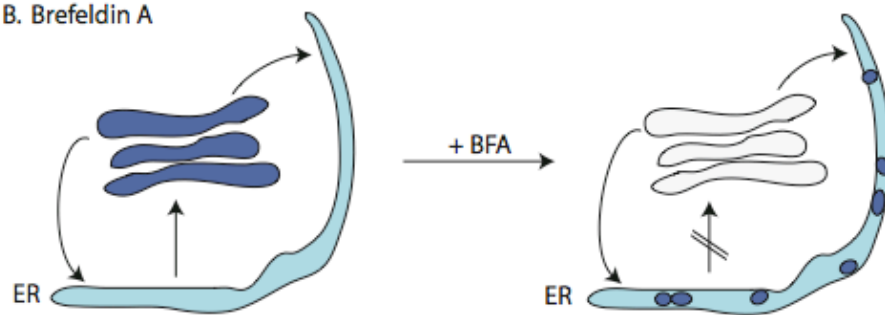


Figure 8. Mitosis in the Eukaryotic cell. Mitosis is the process used for cell division and begins in prophase when the nuclear envelope dissolves and the chromosomes are condensed. In metaphase the condensed chromosomes line up in the middle of the cell before being separated and pulled to opposite ends of the cell during anaphase. During telophase the nuclear envelope reforms and the cell division is completed. The majority of the time the cell is in interphase where the DNA is duplicated.

A. Nocodazole



B. Brefeldin A



C. Monensin/ Bafilomycin A1

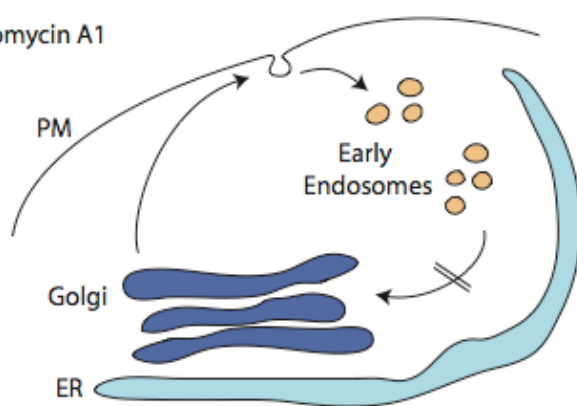


Figure 9. Effects of Golgi Disturbing Agents. (A) Nocodazole addition causes the reversible depolymerization of microtubules, which in turn fragments the Golgi ribbon resulting in small-dispersed Golgi stacks. (B) Brefeldin A addition blocks ER exit of proteins leading to the

(Figure 9 continued)

accumulation of Golgi enzymes in the ER. Although the enzymes are retained in the ER, the peripheral (matrix) proteins remain in the Golgi. (C) Monensin and Bafilomycin addition have been shown to block protein export from endosomal compartments through inhibition of vacuolar ATPases leading to an increase in luminal pH of the Golgi apparatus. Golgi proteins that cycle through the endosomes can accumulate under monensin/bafilomycin addition.

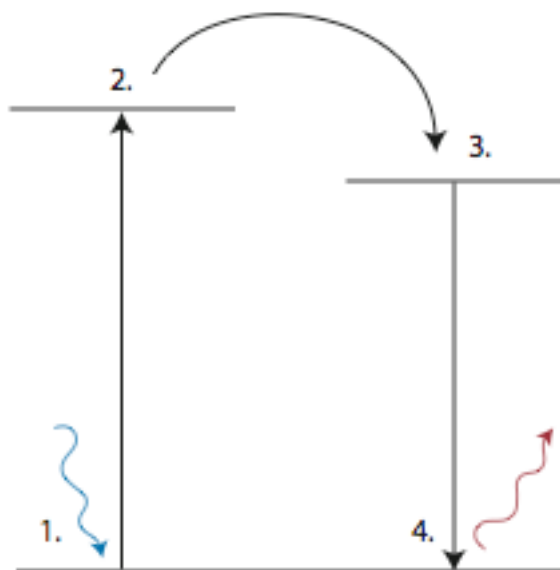


Figure 10. Fluorescence excitation and emission diagram. When a fluorescent molecule is excited (1), it absorbs the energy prompting electrons to a higher energy state (2). A small amount of energy is lost due to heat (3) before the electron returns to its lowest energy state (4) while emitting a longer wavelength of light.

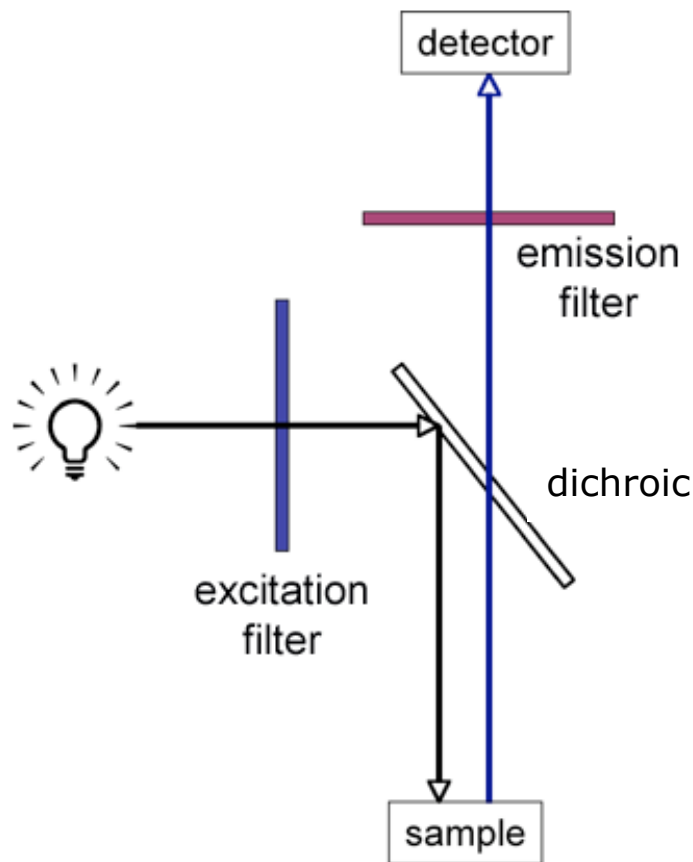


Figure 11. Fluorescent Microscopy Diagram. Light from the excitation source passes through a filter before being reflected off the dichroic mirror onto the sample. The sample emits light at a longer wavelength (as illustrated in Figure 10) that passes through the dichroic mirror before encountering the emission filter and eventually the detector.

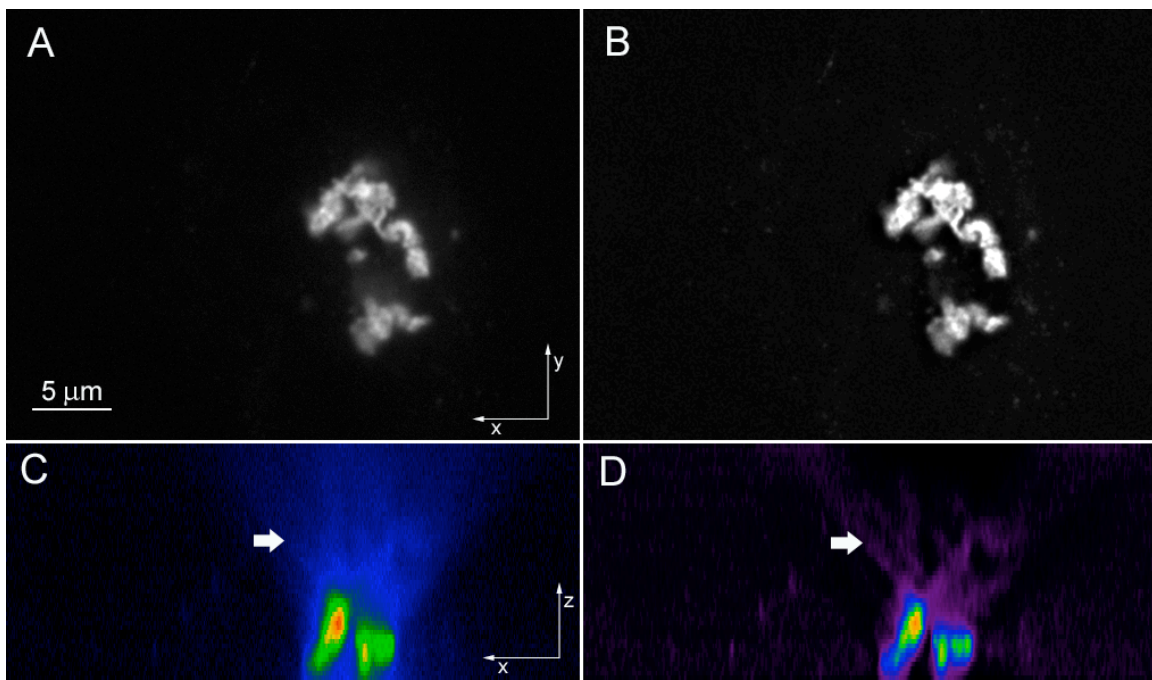


Figure 12. Impact of Deconvolution on Visualized Signal. GalNAcT2-GFP cell before (A,C) and after (B,D) deconvolution using Huygens software. Deconvolution increases the brightness and contrast as evidenced by the XY-plane of a HeLa cell transfected to express GalNAcT2-GFP (A, B) from a spinning disk confocal image stack. These enhancements are most apparent when viewed along the axial direction (XZ-plane) using a rainbow look-up table to better illustrate the decrease in light spread after deconvolution analysis (compare arrows in C, D).

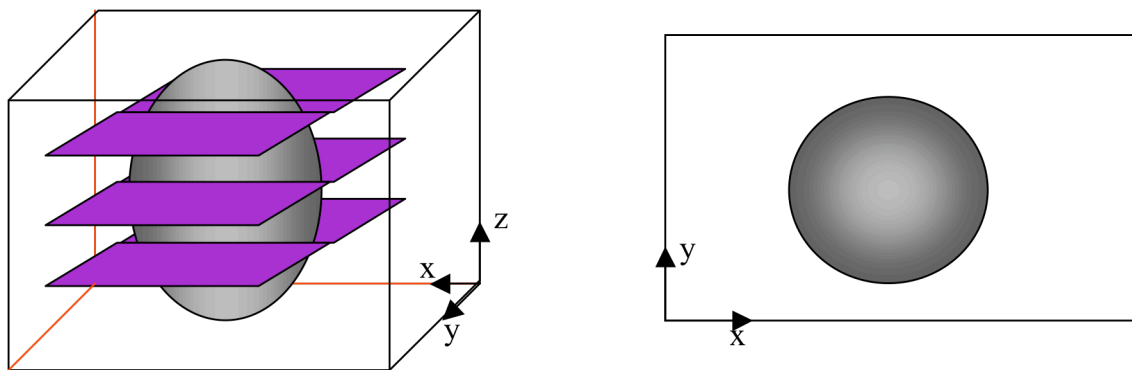


Figure 13. Confocal Microscopy. Confocal sectioning capabilities allow serial XY-slices to be acquired along the Z-axis of a sample providing the researcher with a 3-dimensional representation of the specimen.

CHAPTER 3– The Steady-State Distribution of Glycosyltransferases Between the Golgi Apparatus and the Endoplasmic Reticulum is Approximately 90:10.

3.1 INTRODUCTION

Two separate models for the transport of proteins through the Golgi apparatus have been proposed: the vesicular transport and cisternal maturation model. The first asserts that the Golgi apparatus is an independent, stable organelle consisting of stacked, individual cisternae connected by anterograde vesicular cargo transport (Rothman, 1994; Rothman and Wieland, 1996). The latter asserts that the Golgi apparatus is a dynamic, functional extension of the endoplasmic reticulum (ER) involving retrograde recycling (Glick and Malhotra, 1998; Pelham, 1998). Support for the cisternal maturation model comes from several avenues. Presence of an underlying recycling between the two organelles is supported by experiments involving the addition of the drugs brefeldin A and nocodazole, retrograde trafficking of toxins, fluorescence recovery after photobleaching studies (FRAP), and ER exit block experiments. Brefeldin A addition caused the Golgi to rapidly redistribute to the ER while nocodazole, acting at a slower rate, resulted in the dispersal of Golgi to peripheral ER sites (Cole et al., 1996; Doms et al., 1989; Lippincott-Schwartz et al., 1989; Yang and Storrie, 1998). Microinjection of a dominant negative mutant of Sar1 (Sar1p^{dn}), a small GTPase needed for COP II-mediated export from the ER, resulted in the accumulation of Golgi proteins in the ER (Storrie et al., 1998). Many bacterial toxins, such as Shiga and cholera toxin, use the retrograde machinery of the secretory pathway to enter the ER via the Golgi before being transferred to the cytosol (Sandvig and van Deurs, 2002). Finally, irreversible photobleaching (FRAP) of Golgi and ER pools of a Golgi resident protein were used to measure the recovery of the protein from the non-bleached pool (Zaal et al., 1999). These experiments suggest an underlying recycling pathway through the ER, which in turn should lead to a pool of some concentration of Golgi proteins in the ER at steady-state.

What that steady-state concentration of Golgi proteins within the ER is is not universally agreed upon. A value of ~30% resident Golgi proteins within the ER, based on GFP-tagged Golgi resident protein studies, has been suggested (Cole et al., 1996; Zaal et al., 1999). Alternatively, cell fractionation studies support an ER presence but suggest a value of ~5-10% in the ER (Farmaki et al., 1999; Jesch and Linstedt, 1998; Jokitalo et al., 2001; Moore, 1974; Pelletier et al., 2000). A large pool of Golgi enzyme protein in the ER should lead to Golgi glycosylation within the ER, for which there is no evidence (Kornfeld and Kornfeld, 1985). This also begs the question as to whether the Golgi can be considered a separate organelle, independent of the ER (Pelletier

et al., 2000). The question remains: what is the true distribution of resident Golgi apparatus enzymes in the Golgi and endoplasmic reticulum (ER) at steady-state?

For our studies we focused on the Golgi glycosyltransferases β 1,4-galactosyltransferase (GalT) and UDP-N-acetylglucosamine:polypeptide N-acetylgalactosaminyltransferase 2 (GalNAcT2). Both proteins are characteristic type II, transmembrane, resident Golgi enzymes involved in glycosylation, the major posttranslational modification of most extracellular and cell surface membrane proteins. GalT proteins are mostly found in the trans Golgi and trans Golgi network (TGN) (Nilsson et al., 1993) as compared to GalNAcT2, which is distributed throughout the Golgi (cis to trans) with some preference for the trans region (Röttger et al., 1998). For our studies, we used HeLa cells stably transfected to overexpress GalNAcT2 protein fused with either a green fluorescent protein tag (GalNAcT2-GFP) or epitope tagged with vesicular stromatitis virus (GalNAcT2-VSV). Previous studies (Röttger et al., 1998; Storrie et al., 1998) have demonstrated that these overexpressing tagged systems retain the normal GalNAcT2 distribution in the Golgi.

Ideally there would be continuity between all available analysis methods and the true protein distribution could be easily determined. Unfortunately this is not the case. Although electron microscopy is the more quantitative approach, it is time consuming and can not be done with live cells. Fluorescent microscopy is a commonly available technique that can be used for live cell *in situ* experiments but has lower resolution capabilities. Our goals are to (1) develop a quantitative methodology for analyzing protein distribution using fluorescent microscopy, (2) determine the true steady-state concentrations in the Golgi apparatus and ER of two Golgi resident proteins, and (3) reconcile the discrepancy found within the literature regarding the steady-state distribution. To do this, we used a combination of qualitative and quantitative experiments to test for Golgi resident protein distribution. These studies included fluorescent microscopy (widefield and confocal) experiments, high resolution electron microscopy, and a mathematical approach involving a kinetic two-compartment transport model. Our results indicate an approximate 90:10% Golgi: ER protein distribution for both GalNAcT2 and GalT. These results were not affected by the presence of cyclohexamide, a protein synthesis inhibitor, providing further evidence for the existence of a continuous Golgi-ER recycling pathway. In addition, the results prove that accurate protein quantification is possible using fluorescent microscopy with the aid of image enhancement software and digital technology.

3.2 MATERIALS AND METHODS

3.2.1 Cell Culture

Wild-type (WT) HeLa cells were cultured in Dulbecco's Modified Eagle Medium (DMEM) supplemented with 10% fetal bovine serum (FBS, Hyclone, Logan, UT). HeLa cells stably expressing GalNAcT2-GFP and GalNAcT2-VSV (Storrie et al., 1998; Yang and Storrie, 1998) were cultured in the presence of 0.45 mg/ml of geneticin sulfate (Sigma-Aldrich, St. Louis, MO). One or two days before studies were initiated, transfected cells were co-plated with WT cells in medium without geneticin and grown to ~70% confluence in 100 mm polystyrene culture dishes containing 11 mm glass cover slips for fixation. For cycloheximide (CHX) treatments, cover slips from one 100 mm dish were transferred into two 35 mm dishes, one of which had 50 µg/ml of CHX, and both were incubated for 4 hours before being fixed and stained.

3.2.2 Kinetic Modeling - Experimental Details

Images collected in an earlier publication from the Storrie laboratory (Miles et al., 2001) were analyzed. Briefly, for FRAP experiments, GalNAcT2-GFP relative fluorescence over the ER for three cells was recorded after 35% photobleaching of the ER with a Zeiss LSM 510 laser scanning microscope (Carl Zeiss, Jena, Germany). For ER exit block experiments, Sar1p^{dn} protein was directly injected into the cytoplasm in the presence of 100 µg/ml CHX causing an acute block. Visually identifiable Golgi areas were scored and averaged for 10 cells at each time point and the decrease in area was obtained as a rate from an exponential fit using Kaleidagraph 3.5 software (Synergy Software, Reading, PA). Note that exact knowledge of the total ER/Golgi fluorescence intensity or further image enhancement through deconvolution was not required for these rate measurements.

3.2.3 Electron Microscopy

Electron microscope images collected in an earlier publication from the Storrie laboratory (Storrie et al., 1998) were analyzed. Labeling densities of GalNAcT2 (identified by antibodies attached to 10 nm gold particles) over Golgi cisternae, tubules, ER, nucleus, and mitochondria were tabulated (34,000 magnification, n=15). Note that at 34,000 magnification the area between the individual cisternae can be readily distinguished (Figure 2A). This is not the case at the lower magnifications (Figure 2C). The area of each organelle was determined using stereology with a 1.7cm x 1.7cm grid (actual grid size: 0.20µm x 0.20µm) (Appendix 1). Two approximate Golgi

areas were calculated: (1) cisternal area only and (2) area that included the regions between cisternae (referred to as block Golgi). Using the number of intersections and the volume of each grid square ($0.04 \mu\text{m}^2$) it is possible to determine the approximate area of each organelle (details provided in Appendix 1). The particle density (number/ μm^2) of each organelle was calculated by dividing the gold particle count (number) by the relative area (μm^2). The protein density of the cisternae was calculated with and without the area between the cisternae included.

The relative areas of the Golgi and ER were found by random sampling of EM images at 10,000 and 16,000 magnification using stereology (Appendix 1). A 0.5 mm x 0.5 mm grid was used for all images (10,000 magnification, n=33; 16,000 magnification, n=61). Note that at the lower magnifications it is not possible to see the Golgi tubules or distinguish the area between cisternae as it was at the higher magnification. Therefore, the measured areas at the lower magnifications are of the cisternae and the area between (block Golgi). This makes it necessary to calculate the tubular area contribution using the tubule and block Golgi relative area ratio found at the higher magnification (See Appendix 2 for calculations). Using the relative area ratio of the block Golgi and cisterna, we were also able to correct for the cisternal area contribution thereby excluding the area in between cisternae. The relative protein distributions for the Golgi, ER, and tubules were determined by multiplying the protein densities determined at the higher magnification (34,000) with the relative areas measured at the lower magnifications. The combined contributions from the cisternae and tubules yield the overall Golgi relative protein distribution.

3.2.4 Conventional Widefield Microscopy and Spinning Disk Confocal Microscopy

For light microscopy experiments, cells cultured on cover slips were fixed with 3% formaldehyde in PBS and permeabilized with 0.1% saponin. Fish skin gelatin was used as blocking reagent in all steps (Jiang and Storrie, 2005). WT or GalNAcT2-VSV expressing HeLa cells were stained with monoclonal antibodies against endogenous GalT (a gift from Dr. Tommy Nilsson, Cell Biology and Biophysics Programme, EMBL-Heidelberg) at 1:10 dilution or affinity-purified rabbit polyclonal antibodies directed against the VSV-G epitope (Jokitalo et al., 2001) at 1:1000 dilution, and Cy3-conjugated donkey anti-rabbit or mouse IgG antibodies (Jackson ImmunoResearch Laboratories, West Grove, PA) at 1:1000 dilution were used as second antibodies. The cover slips were mounted in buffered solution of the water-soluble plastic, Mowiol.

Single-plane widefield images were taken using a Zeiss Axiovert 200M microscope with 63x 1.4 NA objective, 1.6x optovar and a Roper CoolSNAP HQ CCD camera (RoperPhotometrics, Tucson, AZ). The camera was operated at 1x1 binning. Spinning disk confocal image stacks were obtained using a CARV accessory (Atto Bioscience, Rockville, MD) mounted to the sideport of the Zeiss Axiovert 200M microscope. An 100x, 1.4 NA objective was used and images were captured to a Retiga EXi camera (QImaging, Burnaby, British Columbia, Canada). Illumination was with an X-Cite 120 light source (Hg-halide lamp, Exfo Life Sciences, Mississauga, Ontario, Canada). Nyquist oversampling criteria was met at 100 nm pixel size for single-plane widefield images and a voxel size of 72 nm x 72 nm x 150 nm for spinning disk confocal image stacks. Each image in the confocal stack was taken at 1.5 s exposure time and a camera gain of 400 for endogenous GalT and 1000 for GalNAcT2-VSV. Fluorescence bleaching while capturing a typical stack consisting of 40 slices was < 3% based on capturing an equivalent stack a second time. All images were acquired as 12-bit data utilizing most of the available 4096 grayscales. Image capture software was IPLab 3.9 (Scanalytics, Fairfax, VA) for Mac OS X.

3.2.5 Laser Scanning Confocal Microscopy

GalNAcT2-VSV cells were co-plated with WT cells and fixed on glass cover slips and antibody stained as described for conventional microscopy. Images were taken at the Keck Imaging Center, Virginia Polytechnic Institute and State University, Blacksburg, VA on a Zeiss LSM 510 microscope using 543 nm laser excitation with pinhole diameters set at 1 Airy unit. A 63x 1.4 NA objective was used with a zoom factor of 4.5 to achieve a voxel size of 60 nm x 60 nm x 150 nm. Eight-bit single pass scanning with pixel dwell time of 2.56 μ s was used to minimize photobleaching.

3.2.6 Fluorescence Image Processing and Analysis

Images were analyzed for intensity as raw and deconvolved data arrays. Raw spinning disk images were background corrected by subtracting a 16-frame average of a blank field image with an added offset value of 128 to avoid zero-intensity pixels. The raw images were then deconvolved with Huygens Essential 2.7 software (Scientific Volume Imaging, Hilversum, The Netherlands). An iterated maximum likelihood estimation algorithm was used. To avoid amplification of speckling, deconvolution iteration was limited to five for widefield GalNAcT2-VSV images and ten for other widefield images or spinning disk confocal VSV images. All other spinning disk or laser scanning confocal images were deconvolved for the number of iterations required to meet the pre-set Huygens software quality criterion.

Cell boundaries were outlined visually with a gamma value of 0.4 to show dimmer structures. The gamma function in the IPLab software is a contrast function that can help compensate for non-linearities in the image capture process. Or, as in our case, allow us to visualize the dimmer ER signal in the same image as the brighter Golgi signal. The total fluorescence intensity of the pixels within the boundary were then summed using IPLab software and corrected for the mean WT cell intensity or non-cell background in the case of endogenous GalT. WT cells were, with the exception of the GalT experiments, intermixed in the image field with the GFP or VSV tagged cells. A visual Golgi apparatus threshold was drawn with the IPLab software segmentation-drawing tool and determined as an intensity value by sliding the selection bar in the segmentation menu of IPLab to flood the outlined area. A calculated Golgi apparatus threshold was determined using the mean ER intensity (average value in a region from the juxtanuclear Golgi apparatus) plus two times the standard deviation of the intensity for that pixel region. Pixels within the cell boundary were then tested for brightness over a (visual or calculated) threshold value and the clusters of these bright pixels larger than a cutoff area ($1.0 \mu\text{m}^2$ for widefield images and $0.5 \mu\text{m}^2$ for slices of confocal sets) were considered as Golgi pixels. The total intensity of the Golgi pixels was summed and corrected for the mean ER value. In short, the Golgi fraction was calculated by the following equation,

$$\text{(Golgi fraction)} = \frac{\text{(total intensity in Golgi)} - (\text{mean ER intensity}) \times (\text{total Golgi area})}{\text{(total cell intensity)} - (\text{mean background}) \times (\text{total cell area})}$$

For confocal image stacks, the mean and standard deviation of the ER varied little between different slices within a stack. The mean of the ER values over the entire stack was used to calculate the Golgi threshold in the equation above. Surface plots were done with ImageJ software (freeware, Research Resources, NIH, Bethesda, MD) and IPLab was used for all image measurements.

3.3 RESULTS

3.3.1 Golgi to ER exchange kinetics indicate an ~90:10 Golgi to ER distribution

The cisternal maturation model requires that glycosyltransferases “resident” in the Golgi apparatus actively recycle during each round of transport. Much of this recycling must be within the Golgi cisternal stack. However, a portion may well be recycled between the Golgi apparatus and ER as part of an ongoing need to balance membrane flows (Storrie et al., 2000). Hence, a quantifiable fraction of fully processed Golgi enzymes should be normally found in the ER.

Fluorescence microscopy data from Zaal et al. (Zaal et al., 1999) suggested that ~67% of GalT-GFP was Golgi localized and the remaining 33% in the ER. A high ER value was surprising given that Golgi-specific glycosyltransferases and glycosidases do not normally modify ER resident glycoproteins (for review, see Storrie, 2005). We therefore looked at quantifying this distribution using direct kinetic rate measurements.

Assuming the transport time between the Golgi and the ER is much shorter than the residence times within, we modeled the Golgi and the ER as two separate compartments connected by first-order transport processes (Figure 1A). The change in ER enzymes as a function of time can be described by:

$$\frac{dE}{dt} = -k_{ER} E + k_{GA} (1 - E), \quad (1)$$

where E is the relative concentration of proteins in the ER and k_{GA} and k_{ER} are the rate constants for transport between the Golgi and the ER in the retrograde and anterograde directions, respectively. Degradation and synthesis are neglected in our analysis due to experimental conditions investigated (i.e. CHX addition and relatively long life of the proteins within the scope of these experiments). The general solution of the differential equation can be written as

$$E(t) = E_{ss} + C \exp [- (k_{GA} + k_{ER}) t], \quad (2)$$

where the integration constant C is determined from the initial condition. The steady-state solution, E_{ss} , is given by a ratio of the rate constants:

$$E_{ss} = k_{GA} / (k_{GA} + k_{ER}). \quad (3)$$

Using GalNAcT2-GFP transfected HeLa cells, Miles et al. collected fluorescent microscopy data in the presence of cycloheximide (CHX), with and without mSar1p^{dn} protein as an ER exit block, that can now be used to determine the steady-state distribution (Miles et al., 2001). In the presence of mSar1p^{dn}, a small GTPase involved in COPII mediated ER exit (Miles et al., 2001; Storrie et al., 1998), GalNAcT2-GFP loss from the Golgi and accumulation in the ER was recorded and quantified as previously described and briefly outlined in Material and Methods in this chapter. For this analysis, k_{ER} was set equal to zero by definition (i.e. ER exit block prevented transport out of the ER to the Golgi) and the final steady-state was reached when all proteins relocate at the rate k_{GA} into the ER ($E_{ss} = 1$). A value of $0.57 \pm 0.04 \text{ h}^{-1}$ for k_{GA} was reported. In the absence of mSar1p^{dn}, FRAP experiments were done following photo-bleaching of $\sim 35\%$ of ER fluorescence. Equation 2 was then fit to the intensity recovery data from the time-lapse image set using Kaleidograph and from three separate measurements we found $k_{GA} + k_{ER}$ to be $4.00 \pm 0.42 \text{ h}^{-1}$ (Figure 1B). Substituting these measured values into equation 3 yields an ER pool value for GalNAcT2-GFP to be $14 \pm 2\%$ and, hence, a distribution of $\sim 90:10$ Golgi to ER. Given these values as measured rate constants, one can say that GalNAcT2-GFP would exit the Golgi apparatus at a rate of $1.0\% \text{ min}^{-1}$ and exit the ER at a rate of $5.7\% \text{ min}^{-1}$. The reciprocals of these values yields the mean residence times of $106 \pm 8 \text{ min}$ in the GA and $17.8 \pm 2.2 \text{ min}$ in the ER for a total cycle time of $124 \pm 8 \text{ min}$ for GalNAcT2, in contrast with previously estimated total residence times of $84.6 \pm 11.3 \text{ min}$ for GalT (Zaal et al., 1999). The major difference in results between our lab and the Zaal lab was again due to the method used to measure the fluorescent intensities that were then used to fit the model parameters. The calculated rate constants were affected by the incorrectly measured ER and Golgi pool intensities that were used in the fit of the data versus time.

3.3.2 Immunogold electron microscopy indicates $\sim 90:10$ distribution of GalNAcT2-VSV between the Golgi Apparatus and ER

Given the difference in distribution values between the kinetic model analysis of fluorescent microscopy data for GalNAcT2 and the previously reported direct fluorescent microscopy results for GalT (Zaal et al., 1999), we wanted to validate our fluorescent results for GalNAcT2 distribution by electron microscopy (EM). In contrast to light microscopy, the resolution of the electron microscope is high relative to the underlying structures. Based on our kinetic modeling

results, we expected the level of ER labeling to be low for any given glycosyltransferase. Therefore, for the immunogold experiments, we chose to use stably transfected GalNAcT2-VSV. At five-fold overexpression, GalNAcT2-VSV has the same cellular distribution as that of an endogenous protein (Röttger et al., 1998) and has been found repeatedly to have the same cycling kinetics between the Golgi apparatus and ER as other Golgi enzymes (Girod et al., 1999; Miles et al., 2001; Storrie et al., 1998).

Three sets of electron micrographs had been previously taken (Storrie et al., 1998), one at a magnification of 34,000 and two at lower magnifications (10,000 and 16,000). The higher magnification set was used to quantify immunogold labeling density and the lower images used to score overall Golgi and ER areas. For immunogold labeling, cryosections were incubated sequentially with anti-VSV primary antibody attached to 10 nm immunogold particles to localize GalNAcT2 and with anti-protein disulfide isomerase (PDI) attached to 5 nm immunogold particles to identify ER. GalNAcT2-positive regions that had been photographed at random were scored morphometrically (Storrie et al., 1998). For overall area stereology, cells that had been photographed at random at the lower magnifications of 10,000 or 16,000 were used to identify organelles by their characteristic morphology. Consistent with previous results (Jokitalo et al., 2001; Storrie et al., 1998), GalNAcT2 labeling was heavily concentrated over Golgi cisternae (arrowhead, Figure 2A) and associated tubules (arrows, Figure 2A) with occasional GalNAcT2 labeling (arrowhead, Figure 2B) in association with the PDI-positive ER (arrow, Figure 2B). As shown in Figure 2C, Golgi cisternal stacks (arrowheads) and ER (arrow) could be readily distinguished morphologically in the lower magnification micrographs.

As expected the GalNAcT2 labeling density was much higher over Golgi cisternae and associated tubules than over the ER, mitochondria, or nucleus. We took the average of both mitochondrial and nuclear labeling as an indicator of non-specific reactivity. The level of non-specific labeling was ~30% of that observed over the ER. The mitochondrial/nuclear labeling density was subtracted from all values to give a corrected Golgi apparatus and ER labeling density for GalNAcT2-VSV. Labeling density over the Golgi apparatus was ~80 to a 100 fold higher than that over the ER. In order to convert labeling density to the total distribution of GalNAcT2-VSV between Golgi apparatus and ER, we determined the relative area of ER and Golgi apparatus (cisternae plus tubules) in low magnification, random cell sections. As summarized in Table 1, the Golgi apparatus area was ~12% of the ER. In total, 90% of the GalNAcT2 labeling was associated with the Golgi apparatus and 10% with the ER (Table 1).

3.3.3 Widefield fluorescence microscopy yields ~90:10 Golgi to ER steady-state distribution for Golgi glycosyltransferases

The EM and kinetic analysis distribution values indicated a ~90:10 distribution for GalNAcT2 leading us to investigate whether a similar steady-state distribution of GalNAcT2 between the Golgi apparatus and ER would be obtained using fluorescence microscopy. HeLa cells are fairly thin, ~6-7 μm thick, when imaged as fixed, plastic mounted samples. As such, widefield images focused for bright Golgi apparatus sampling should contain intensity information from the full cell volume; the Golgi apparatus is located at approximately mid-cell height. This was essentially the approach used by Zaal et al. (Zaal et al., 1999) in quantifying GalT-GFP distribution in single plane images collected with a laser scanning fluorescence microscope operated with the pinholes wide open. For our studies, all widefield images were collected at a resolution sufficient for deconvolution analysis (high numerical aperture, 1.4 NA, objectives and ~2x oversampling to give images that met Nyquist sampling criteria).

GalNAcT2-VSV, GalNAcT2-GFP, and GalT all distributed in a similar manner when imaged using wide-field fluorescence microscopy (Figure 3). Antibody staining was used to reveal GalNAcT2-VSV and GalT distributions and the inherent fluorescence of the GFP moiety to reveal the distribution of GalNAcT2-GFP. In images displayed with a normal grayscale range (100-3000 grayscale levels, 12 bit camera), all had a distinct juxtanuclear Golgi-like fluorescence distribution with little detectable fluorescence observed over the cytoplasm (Figure 3A,B,C). When the same images were displayed with a compressed grayscale range that accentuated the display of low intensity fluorescence (100-300 grayscale levels), three striking distributional features were now apparent (Figure 3, A',B',C'). First, the bright, juxtanuclear Golgi apparatus area was now much larger. This was an expected outcome for out-of-focus plane Golgi intensity (i.e., blur) and light spread by the objective, also known as point spread function. Second, there was cytoplasmic fluorescence apparent for all three. Third, particularly obvious for GalNAcT2-GFP (Figure 3B') and GalT (Figure 3C'), the fluorescence pattern gave a rim-like fluorescence staining about the nuclear envelope, typical of an ER distribution. For GalNAcT2-VSV, this was less obvious. This is not unusual for antibody staining as even antibodies against bona fide ER proteins such as p63 often give a somewhat granular staining pattern (see, e.g., Figure 1 in (Girod et al., 1999)). In double label experiments with Sec61p, an ER marker, near complete overlap between the cytoplasmic GalNAcT2-GFP fluorescence and Sec61p staining was observed (personal communication with Dr. S Rhee). We conclude from this that there is a low level of

both GalNAcT2 and GalT present in the ER. At first glance, the intensity of GalNAcT2-VSV staining over the ER was slightly more intense than that of GalNAcT2-GFP or GalT (compare Figure 3A',B',C'). The overall background brightness of the GalNAcT2-VSV labeling was slightly higher than that for GalNAcT2-GFP or GalT (summarized in Table 3).

As a first approximation to determining the apportionment of GalNAcT2 and GalT between the Golgi apparatus and ER, wild type (WT) and tagged HeLa cells were imaged in the same field at a constant illumination intensity and exposure that did not saturate the CCD camera (Figure 4A). To draw organellar and cell boundaries, images were displayed non-linearly (technically, gamma = 0.4) and cell boundaries and the Golgi apparatus were outlined by eye (visual threshold, Figure 4B). Under these conditions, the boundaries of cytoplasmic fluorescence were apparent and little detail was lost due to image display saturation. We then calculated the fraction of total fluorescence intensity from the Golgi apparatus compared to that of the whole cell to be ~63-64% for either GalNAcT2 (epitope or GFP tagged) or GalT (Table 2). Values were the same whether or not the cells had been cultured for 4 h in the presence of cycloheximide to inhibit protein synthesis. Note that all values were corrected for non-specific background fluorescence. For tagged cells, the correction was based on the mean fluorescence level found in co-cultured and co-imaged wild type cells (WT, Figure 4A,B). For endogenous GalT, the level of intensity found between cells was subtracted. Quantitatively these results are essentially the same as those found by Zaal et al. (Zaal et al., 1999) for the visual quantification of a concatenated GalT-GFP-GFP-GFP chimera using widefield microscopy (laser scanning microscope operated with wide open pinholes). Wild type cytoplasmic intensity was about 40% of the total signal found over the ER region of GalNAcT2-VSV and 30% for GalNAcT2-GFP (Table 3). As wide field microscopy is a high signal-to-noise ratio technique (>100, Table 3), the background corrected ER values are significant.

As indicated in Figure 3 (A',B',C'), the actual spread of Golgi specific fluorescence in wide-field images was greater than that apparent to the eye. This was readily apparent in a quantitative manner when the image was reformatted as a surface plot of fluorescence intensity versus XY coordinates (Figure 4C). The Golgi signal surface plotted was a clustered set of intensity peaks much like a mountain range and the visual threshold marked by an arrowhead considerably underestimated the perimeter of the mountain range. To include the whole Golgi signal within the boundary, we measured the average ER intensity within a region far from the Golgi (arrowhead, Figure 4D), calculated a standard deviation based on the individual pixel values in

this region, and used the average intensity value plus two standard deviations as a calculated threshold. Negligible amounts of the ER in dispersed spots were above this calculated threshold as tested in HeLa cells stained for Sec61p, an ER marker (personal communication with Dr. S Rhee). Moreover, the Sec61p distribution indicated that the ER distribution was uniform about the cytoplasm (personal communication with Dr. S Rhee). Such scattered spots were excluded from a Golgi intensity calculation by setting a minimum area limit. The Golgi intensity within the area defined by the calculated threshold was measured and corrected for maximal underlying ER contribution by subtracting with the average ER intensity value from each pixel. This approach yielded a Golgi fraction of almost 90% for both the transfected/overexpressing GalNAcT2-VSV and GalNAcT2-GFP and the endogenous GalT (Table 2, raw, calculated). Addition of cycloheximide did not affect the results.

We thus reasoned that the discrepancy between visual and calculated threshold was an outcome of the objective point spread function. If so, it should be resolved by deconvolution, a mathematical method to reassign light to its source (Swedlow, 2003). After applying iterative maximum likelihood estimation deconvolution to the raw image, we observed that the gap between visual and calculated thresholds was greatly reduced and the two almost overlapped in the XY fluorescence image (Figure 4E). The surface plot showed sharper peaks with reduced perimeter and near overlap of the two thresholds (Figure 4F). Golgi fractions obtained from the deconvolved widefield images using a visual threshold were 85-89% for GalNAcT2 whether VSV or GFP tagged and endogenous GalT, plus and minus cycloheximide, and 87-91% using a calculated threshold (Table 2, deconvolved). This confirmed our hypothesis that objective light spread was responsible for the difference in two different methods for raw images and more importantly indicates that the correct number for distribution of Golgi glycosyltransferases between the Golgi apparatus and ER was ~90:10. As the same result is obtained in the presence of cycloheximide, we infer that this is a steady-state measurement of the Golgi:ER distribution.

Technically, these results strongly indicate that visually identifying the Golgi apparatus from raw images underestimates the Golgi fraction of the glycosyltransferases at ~65% (present work and Zaal et al. 1999). The use of a calculated threshold and/or deconvolution produced a decidedly higher outcome, ~90%, which agreed with both the EM and kinetic modeling quantification. Based on our results, the best practice for widefield microscopy would be to determine a calculated threshold on a deconvolved image, as it applies an objective method to the corrected image (Table 2, bold). Using a calculated threshold on raw images provided a good practical

approximation, as it gave only a slightly lower number than the best practice result and can be applied to undersampled images. In support of the assumption of these experiments that single plane, widefield images focused on bright Golgi apparatus captured fluorescence intensity in a representative manner from the full depth of fixed HeLa cells (~6-7 μ m), we found no statistically significant change in total fluorescence intensity following brefeldin A (BFA) treatment, a condition that disperses Golgi glycosyltransferases into the ER (personal communication with Dr. S Rhee).

3.3.4 Best-practice confocal microscopy also yields an approximately ~90:10 distribution

Having shown that the light spread has to be corrected for best practice scoring of Golgi apparatus and ER fluorescence in widefield images, we decided to test whether the light rejection properties of confocal microscopy reduced and/or eliminated this problem. Moreover, with the optical sectioning properties of confocal microscopy, we can test directly the assumption that widefield fluorescence microscopy provides representative intensity information for the entire cell. Therefore, we imaged HeLa cells as stacks of optical sections at spatial intervals that provide near optimal oversampling for three-dimensional (3D) deconvolution (~70 nm XY pixel spacing and 150 nm Z spacing).

A. Laser scanning confocal microscopy

Initial optical sectioning experiments were performed with a Zeiss LSM510 microscope set to give optimal stray light rejection, 1 Airy unit pinholes, and little to no photobleaching. As expected (Murphy, 2001), these conditions resulted in a low signal-to-noise-ratio image (Figure 5, Table 3). As shown in Figure 5A,A', bright Golgi apparatus staining was observed for GalNAcT2-VSV in raw, unprocessed images. The average Golgi signal-to-noise ratio was 3 (Table 3). When the intensity display was remapped to show dim fluorescence, very slightly brighter fluorescence was observed over the cytoplasm of tagged than wild type cells (Figure 5C). This putative ER fluorescence was ~50% brighter than the wild type background (Table 3). Using either visual or calculated thresholds, the wild-type corrected, stack summated Golgi fraction was ~80%. (Table 4). GalNAcT2-VSV distributions became slightly sharper and had more contrast after deconvolution (Figure 5B,B',D). However, as shown in Figure 5C,D, the visual and calculated thresholds were approximately the same before and after deconvolution and the stack summated Golgi fraction was again ~80% (Table 4). As indicated by the low signal-to-noise ratio, the information content embodied in these average values is limited and therefore further accumulation of cell data by laser scanning microscopy was not pursued.

B. Spinning disk confocal microscopy

Having eliminated laser scanning microscopy optical sectioning due to low signal-to-noise ratio, we next investigated spinning disk confocal microscopy as a potentially much higher signal-to-noise technique. The pinhole size of the ATTO CARV unit at 1.22 Airy units approached that of the Zeiss LSM510 and other optical properties were similar. We found that complete HeLa cell image stacks for GalNAcT2-VSV and GalT staining could be collected without bleaching. As expected (Murphy, 2001), spinning disk confocal microscopy at values of 30-54 gave a considerably higher average Golgi signal-to-noise-ratio than laser scanning confocal microscopy (Table 3). As shown in Figure 6, an individual optical section at approximately mid-Golgi apparatus for GalNAcT2-VSV appeared relatively blur-free compared to widefield microscopy (Figure 2A versus Figure 5A). Similar results were seen for GalT (personal communication with Dr. S Rhee).

When viewed with a non-linear grayscale range (technically, gamma = 0.4), cytoplasmic fluorescence due to ER staining for GalNAcT2-VSV was obvious compared to weak background fluorescence in adjacent wild type cells (Figure 6C) as illustrated in the accompanying surface plot (Figure 6E). For GalNAcT2-VSV, the average ER fluorescence intensity was 2-fold that of background wild type fluorescence, a visually and statistically significant value (Table 3, Figure 6). Using raw, unprocessed image stacks and a visual threshold, the Golgi fraction for both GalNAcT2-VSV and GalT staining was ~65% (Table 5), very similar to that found for widefield microscopy in a single image plane. When a calculated ER threshold was applied to the raw, unprocessed image stacks, the Golgi fraction for GalNAcT2-VSV and GalT was now ~85%, again similar to that found for widefield microscopy in a single image plane. These values confirm the supposition that the single plane widefield images contain intensity information from the entire HeLa cell. Moreover, comparison of the widefield images with the spinning disk confocal images (Figures 4,6) lead to the conclusion that reduced blur with confocal imaging does lead to the calculated threshold being closer to the visual threshold in XY images. With deconvolution, as expected, the brightness and contrast of the juxtanuclear Golgi apparatus staining increased and Z dimension blur (Figure 5A',B'), in particular, decreased. As summarized in Table 5, the Golgi fraction for GalNAcT2-VSV and GalT was ~65% with visual thresholding and ~90% with calculated thresholding of deconvolved image stacks. The deconvolved, calculated threshold values in Table 5 are bolded to indicate best practice values.

3.4 DISCUSSION

Despite the general acceptance that many Golgi proteins cycle through the ER, the extent of Golgi protein residence within the ER and more importantly how such residency can be compatible with the functional properties of the two organelles remain highly controversial. In terms of quantification, the controversy is particularly acute for GFP chimeric proteins with Golgi glycosyltransferases (Axelsson and Warren, 2004; Jokitalo et al., 2001; Zaal et al., 1999). The fraction of Golgi glycosyltransferases residing in the ER at steady-state and the most reliable method for measuring this pool is also a subject of debate. Techniques used to quantify this ER pool, such as cell fractionation, electron microscopy, and fluorescence microscopy, have reported fractions ranging in value from ~30% to ~10% to < 1% (Jokitalo et al., 2001; Puri and Linstedt, 2003; Zaal et al., 1999). Although cell fractionation is an established quantitative approach, it requires destruction of the cells and membranes within. Electron microscopy, in conjunction with gold labeled antibodies, offers a high resolution approach to analysis; but again, cannot be done with live cells. Fluorescent microscopy can be used with immunolabeled and live fluorescently tagged cells, but comes at the expense of much lower resolution and signal-to-noise issues.

The goal of our research was to determine the real steady-state distribution and resolve the quantitative differences found between fluorescent microscopy, cell fractionation, and EM. With this work we have conclusively shown using three different methods, fluorescent microscopy, EM, and kinetic modeling, that a stable pool of Golgi protein exists in the ER and was measured to be ~10% for both overexpressed and endogenous glycosyltransferases. This result conflicted with previous work by Zaal et al. which suggested that the distribution of the glycosyltransferase GalT was ~70:30 Golgi to ER. To verify that the difference was not protein specific, we showed that endogenous GalT in our hands also was found in a 90:10 distribution. Using similar experimental conditions as the Zaal group, however we were able to reproduce their result of 70:30 Golgi to ER distribution for the GalT protein. A large ER pool of Golgi proteins should indicate some enzymatic activity of these proteins in the ER, which has been shown not to be the case. Also, quantitative experiments such as EM, have shown the presence of a smaller ER pool that is more consistent with the observed activities of these proteins in the organelle. The major discrepancy in results found between our laboratories was a consequence of our chosen methods of image analysis. Zaal et al. followed the established, previously accepted method of identifying the Golgi signal by using a visual threshold. Our approach, however, of treating the images as two-dimensional data arrays with each pixel representing a separate point

in the array, yields information that was not otherwise apparent from the visual analysis alone. This provided a solution to the problem of how to objectively draw a perimeter between the Golgi apparatus and ER in the light micrographs. Because of the sampling and detection limitations involved with fluorescent microscopy, point light spread is a legitimate concern. Although Zaal et al. reported the use of a laser scanning confocal microscope (LSM), the pinhole was set wide open thereby negating its purpose. LSM is reported to have a low signal-to-noise ratio making it difficult to reliably distinguish the diffuse ER signal from non-specific background. Because of the inability to quantitatively measure the portion of signal in the ER, laser-scanning microscopy analysis was not pursued. Our use of the spinning disk confocal microscope, a higher signal-to-noise technique, did reduce the presence of light spread in most cases, but did not entirely eliminate the problem. Using deconvolution as an added restoration step resulted in sharper and more defined Golgi signal.

Reviews of the literature call into question the reliability of the term ‘quantitative’. The actual methods of analysis used by most attempt to be as objective as possible, but usually fall short when user defined thresholding and boundary definitions are introduced. This is most apparent for experimental systems involving fluorescent microscopy. While fluorescent probes provide methods to *qualitatively* study proteins in a variety of systems, the correct way to *quantitatively* analyze the results is a debatable issue. Most researchers end up using visual thresholds whether it be for spatially differentiating between regions of a cell (Belichenko et al., 1996; Peet et al., 2004) or determining protein concentrations in these regions (Chen et al., 1994). By using visually identified boundaries separating the ER and Golgi, Zaal et al. inadvertently underrepresented the actual amount of protein present in the Golgi. These issues are generally related to the limited resolution of light microscopy, a factor not associated with EM. Another commonly overlooked factor when doing quantitative research is correct image acquisition techniques. Proper image sampling is critical for quantitative analysis. It is important to properly oversample (per Nyquist theorem), avoid photobleaching, and to operate within the limits of the detector (overexposure). Deconvolution requires that these conditions be met before processing. The general scientific community is slowly becoming aware of the details involved with proper quantitative analysis as evidenced by the increase in literature citing the use of image enhancement software. These imaging techniques, if applied correctly, can be used in a variety of areas. For example, deconvolution technology has been used to study the dynamics of DNA chromatin (Aten et al., 2004), the kinetics of surface glycoproteins during endocytosis (Engstler et al., 2004), and to visualize polarized cell membrane lipids (Wustner, 2005), to name a few.

Finally, as fluorescent technology continues to develop, more quantitative methods of analysis will also emerge.

In conclusion, the results presented here dispel the myth that fluorescent microscopy is incapable of obtaining similar results as higher resolution techniques. With proper image oversampling and a quantitative approach to analysis, including deconvolution and computer calculated boundaries, it is possible to extract real data using both conventional and confocal fluorescent microscopy systems. In addition, these low ER residency values of Golgi glycosyltransferases are consistent with the functional distinctions between the two organelles. Finally, the research and theories presented here provide a multi-approach analysis for the quantification of a small ER pool of Golgi proteins, while at the same time supporting the existence of a cycling equilibrium between the Golgi apparatus and ER at steady-state.

Table 1. GalNAcT2-VSV relative protein distribution by immunogold labeling

	Golgi Cisternae	Golgi Tubules	ER
Particle Density (number/ μm^2)	227	166	2.86
Relative Area Average (n=2)	5.57 ± 0.4	7.09 ± 0.5	100
Relative Protein Average (n=2)	90 ± 1.5		10 ± 1.5

GalNAcT2-VSV gold particle labeling density over Golgi cisternae, associated Golgi tubules, and ER was determined as described in Materials and Methods. Values were corrected for background, non-specific labeling by subtraction using the average of the labeling density over mitochondria (2.0 particles per μm^2) and nucleus (1.1 particles per μm^2). Similarly, stereology was used to determine the relative area of the Golgi cisternae, Golgi tubules and ER. n=2 for the number of determinations. \pm values indicate range of the data.

Number of Gold particles counted: Golgi cisternae, 1339; Golgi tubules, 1248; ER, 24; mitochondria, 8; nucleus, 26.

Table 2. Percentage of glycosyltransferases found in the Golgi apparatus measured from single-plane widefield images.

Image	Threshold	GalNAcT2-VSV		GalNAcT2-GFP		Endogenous GalT	
		-CHX	+CHX	-CHX	+CHX	-CHX	+CHX
Raw	Visual	61 ± 5	62 ± 5	64 ± 5	64 ± 5	65 ± 7	66 ± 4
	Calc.	85 ± 5	84 ± 6	90 ± 3	88 ± 4	87 ± 4	89 ± 3
Decon.	Visual	85 ± 6	84 ± 8	89 ± 4	87 ± 5	88 ± 4	89 ± 3
	Calc.	88 ± 7	87 ± 8	91 ± 4	91 ± 4	91 ± 3	91 ± 3

HeLa cells expressing GalNAcT2-GFP or GalNAcT2-VSV and wild-type cells were cultured \pm cyclohexamide (CHX, 50 $\mu\text{g}/\text{ml}$, 4 hours), fixed and stained (VSV and endogenous GalT), and imaged for fluorescence at Nyquist criterion (100 nm/pixel) as single-plane widefield images as described in the Materials and Methods. At least 30 cells were analyzed for each group using raw and deconvolved (Decon.) images with visual and calculated (Calc.) thresholds as described in Material and Methods. Percentage of fluorescence found in the Golgi fraction is given in the table (mean \pm SEM). Results from best possible practice of using calculated threshold on deconvolved images are shown in bold.

Table 3. Comparison of grayscale fluorescence intensity parameters by three fluorescence microscopy methods.

Method	Marker	Wild Type	ER	Golgi (vis)	signal-to-noise (Golgi)	N
Widefield	T2-VSV	20.7 \pm 7.8	48.4 \pm 21	1392 \pm 383	190 \pm 50	30
	T2-GFP	4.1 \pm 2.0	13.7 \pm 5.9	732 \pm 508	110 \pm 70	30
	GalT	0	15.3 \pm 6.7	1260 \pm 391	200 \pm 60	30
Laser scanning	T2-VSV	0.83 \pm 0.50	1.30 \pm 0.29	31.6 \pm 6.6	3.0 \pm 0.6	10
Spinning disk	T2-VSV	13.2 \pm 4.3	25.8 \pm 8.6	701 \pm 90	30 \pm 6	25
	GalT	0	4.0 \pm 1.1	409 \pm 68	54 \pm 9	30

Average grayscale pixel intensities of the wild-type (WT) and ER signal as well as average net intensity of visually identified Golgi apparatus are corrected as shown in the equations below. The non-cell background was ~100 (12-bit camera, 4095 maximum grayscale value) for widefield and spinning disk images and was ~2 (8-bit photomultiplier scaling, 255 maximum grayscale) for laser scanning images. Each of these values corresponds to what can be considered as the dark current sensor set point. For widefield and spinning disk images, the signal-to-noise ratio for average Golgi intensity was calculated by dividing the signal with the background noise in units of photoelectrons. The conversion factor of electrons/(analog-to-digital unit) was obtained from the mean and variance of two flat field images. For laser scanning images, signal-to-noise ratio was calculated from the square root of signal divided by average single-photon hit in the background. All numbers are calculated for N individual cells and shown as mean \pm SEM.

Equations:

Wild-type (WT) = average grayscale value – intercellular background (BG)

ER = average grayscale value – BG

Golgi = average grayscale value over visually outlined Golgi apparatus – (ER + BG)

Table 4. Percentage of glycosyltransferases found in the Golgi measured from laser scanning image stacks.

Image	Threshold	GalNAcT2-VSV
Raw	Visual	77 \pm 9
	Calculated	81 \pm 11
Deconvolved	Visual	78 \pm 8
	Calculated	81 \pm 11

HeLa cells expressing GalNAcT2-VSV were fixed and stained for VSV. Cells (n=10) were imaged and analyzed as confocal stacks as described in Materials and Methods. Results are the percentage of fluorescence intensity found in the Golgi fraction (mean \pm SEM).

Table 5. Percentage of glycosyltransferases found in the Golgi measured from spinning disk image stacks.

Image	Threshold	GalNAcT2-VSV	Endogenous GalT
Raw	Visual	64 <u>±</u> 6	65 <u>±</u> 7
	Calculated	83±4	89 <u>±</u> 5
Deconvolved	Visual	81 <u>±</u> 5	87 <u>±</u> 5
	Calculated	88<u>±</u>6	91<u>±</u>4

HeLa cells expressing GalNAcT2-VSV and wild-type HeLa were fixed and stained for VSV and endogenous GalT. Cells (n = 25, 30) were imaged and analyzed as confocal stacks as described in Materials and Methods. Results are the percentage of fluorescence intensity found in the Golgi fraction (mean \pm SEM). Best practice results are highlighted in bold.

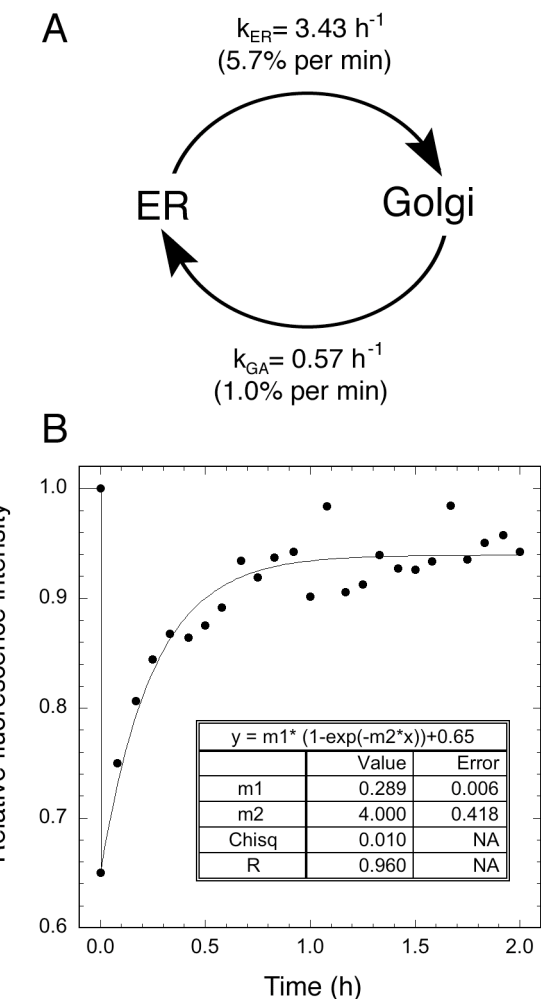


Figure 1. Two compartment model for Golgi glycosyltransferase cycling. A) Schematic diagram of the two compartment kinetic model. The ER and the Golgi apparatus are considered as two separate compartments connected by first-order transport processes. The rate constants k_{ER} and k_{GA} are the ER-to-Golgi (anterograde) and Golgi-to-ER (retrograde) transport rates, respectively. Golgi-to-ER transport rate $k_{GA}=0.57 \pm 0.04 \text{ h}^{-1}$ was measured from an ER exit block experiment using mutant Sar1p^{dn} proteins by Miles et al. (Miles et al., 2001). B) Measured fluorescence recovery after 35% photobleaching of the ER in HeLa cells expressing GalNAcT2-GFP. Relative ER fluorescence was averaged over three separate HeLa cells. Data are redrawn from Miles et al. (2001). The solid curve reflects the fit of the data points to the exponential equation shown. The fitted parameter m_2 in the table inset represents the sum of rate constants $k_{ER}+k_{GA}$. Both rate measurements were done in the presence of protein synthesis inhibitor cycloheximide.

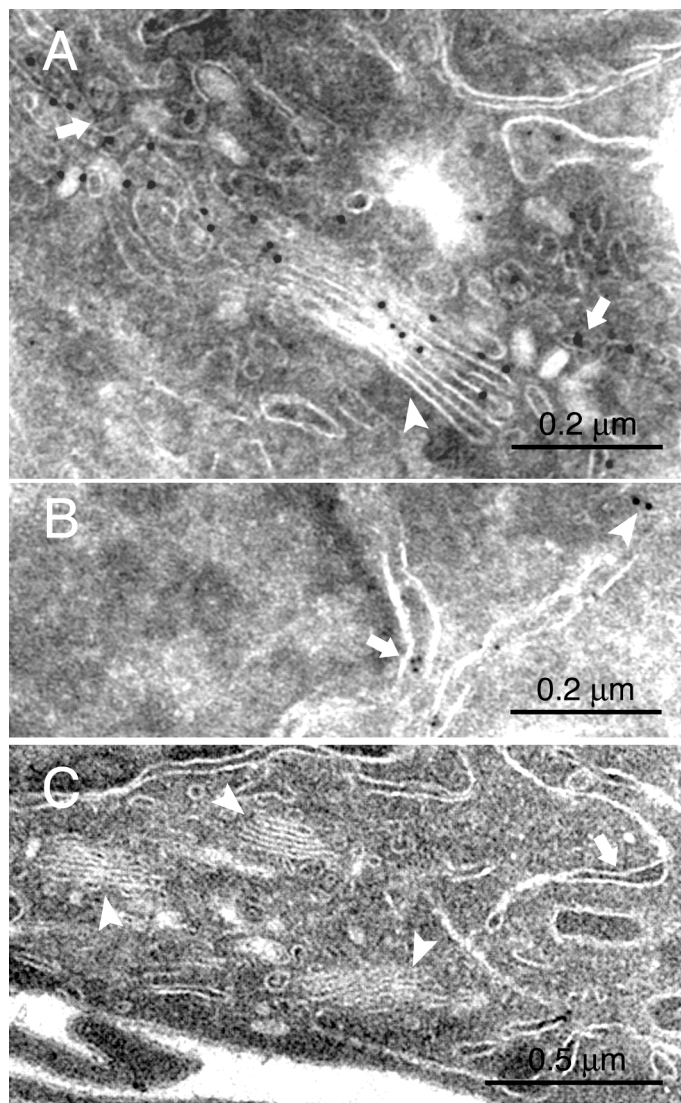


Figure 2. Electron micrographs of GalNAcT2-VSV HeLa cells with immunogold labeling (A,B) and without (C). A) Electron micrograph acquired at 34,000 magnification showing Golgi cisternae (arrowhead) and Golgi tubules (arrow) where 10 nm gold particles indicate VSV labeling as described in the Materials and Methods. B) 34,000 magnification acquired image depicting ER immunolabeled for GalNAcT2 with 10 nm gold particles (arrowheads) and 5 nm gold particles labeling PDI (protein disulfide isomerase), an ER marker (arrow). C) An example of a randomly selected image acquired at 16,000 magnification and illustrating Golgi stacks (arrowheads) and ER ribbon (arrow). Note that the Golgi tubules are not readily apparent and spacing between cisternae is difficult to reliably distinguish at this magnification.

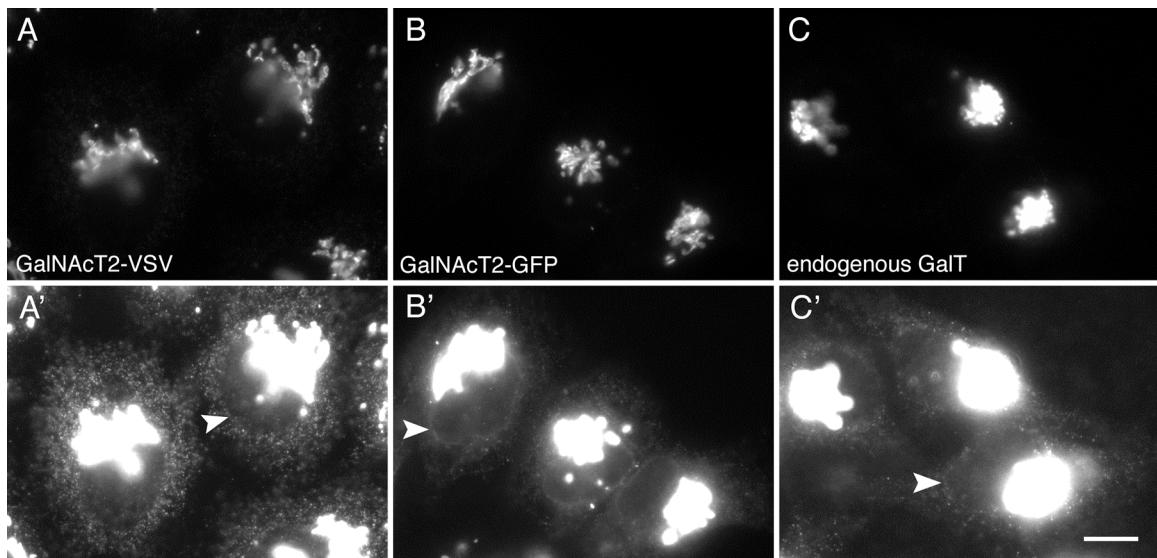


Figure 3. Golgi enzymes are found in the ER at lower concentrations by widefield light microscopy. HeLa cells stably expressing GalNAcT2-VSV (A, A') stained for VSV, expressing fluorescent GalNAcT2-GFP (B, B') fixed and mounted, and wild-type cells stained for endogenous GalT (C, C') are shown as single-plane widefield images. Identical images are shown at normal (A-C, linear mapping of 100-3000 grayscale levels out of 0-4095) and high (A'-C', 100-300 grayscale levels out of 0-4095) brightness. Note that the nuclear envelope (arrowheads) typical of the ER distribution only becomes visible under high brightness (A'-C'). Bar, 10 μ m.

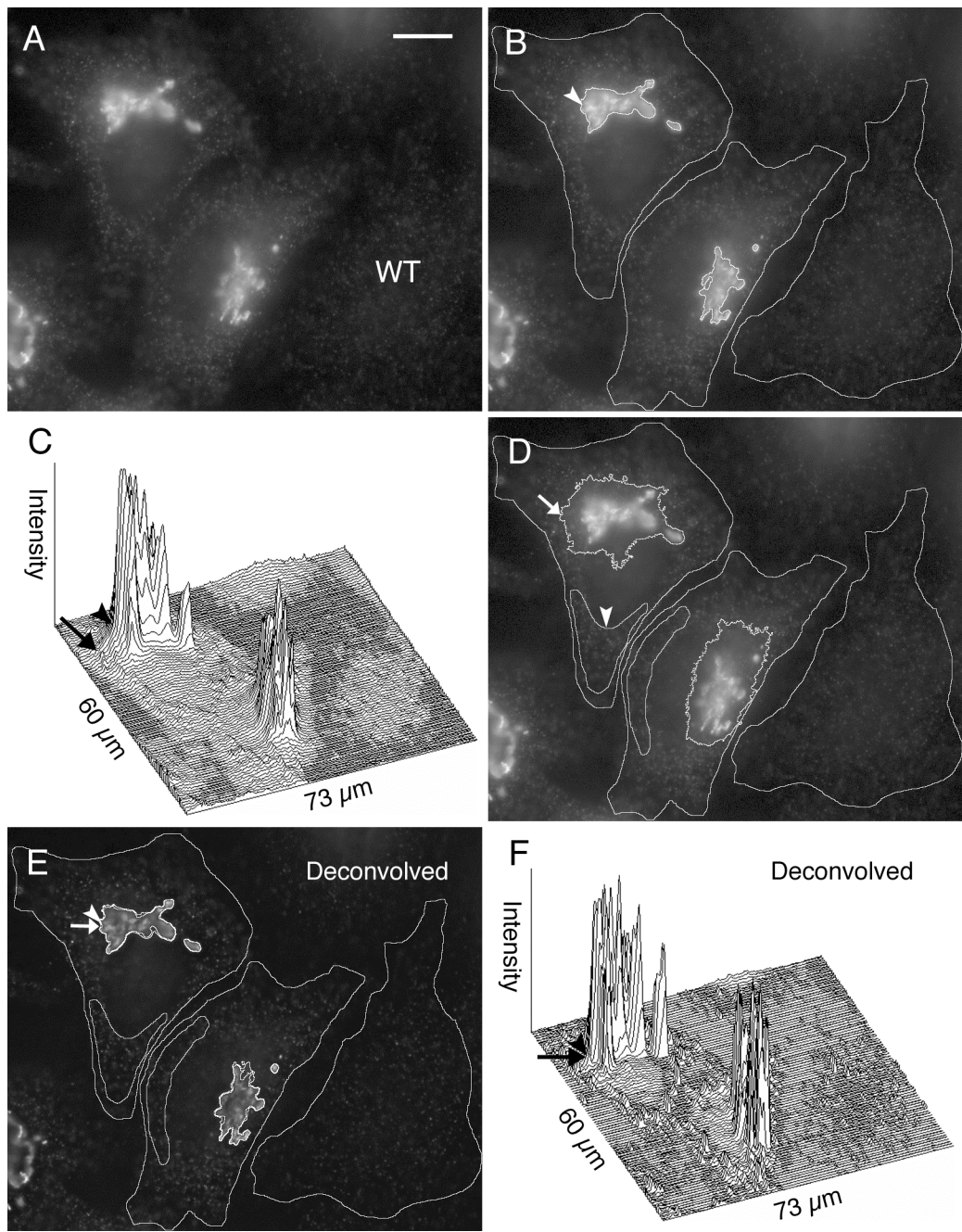


Figure 4. Single-plane widefield images were analyzed before and after deconvolution using visual and calculated thresholds. A) Shown is a fluorescence image of HeLa cells stably expressing GalNAcT2-VSV stained for VSV, as well as a wild-type HeLa cell (WT). A non-linear intensity display ($\gamma = 0.4$) was used to bring out dimmer structures. Bar, $10 \mu\text{m}$. B) Cell outlines are shown as well as the Golgi apparatus as identified visually (visual threshold, arrowhead). C) Shown is the surface plot of the fluorescence intensity. The visual threshold (arrowhead) underestimates the Golgi intensity peak and the calculated threshold (arrow) is needed to account for the total intensity of the peak. D) The average ER intensity plus two standard deviations is indicated by a white circle.

(Figure 4 continued)

standard deviations in the region (arrowhead) far from the Golgi was used for the calculated threshold (arrow). E, F) Shown are the image and its surface plot after 5 iterations of deconvolution. The Golgi apparatus as determined from the visual (arrowhead) and calculated (arrow) thresholds of intensity is outlined or marked. Note the overlap between visual and calculated thresholds. All fluorescence images are shown with gamma = 0.4 while surface plots are drawn with actual pixel values (gamma = 1.0).

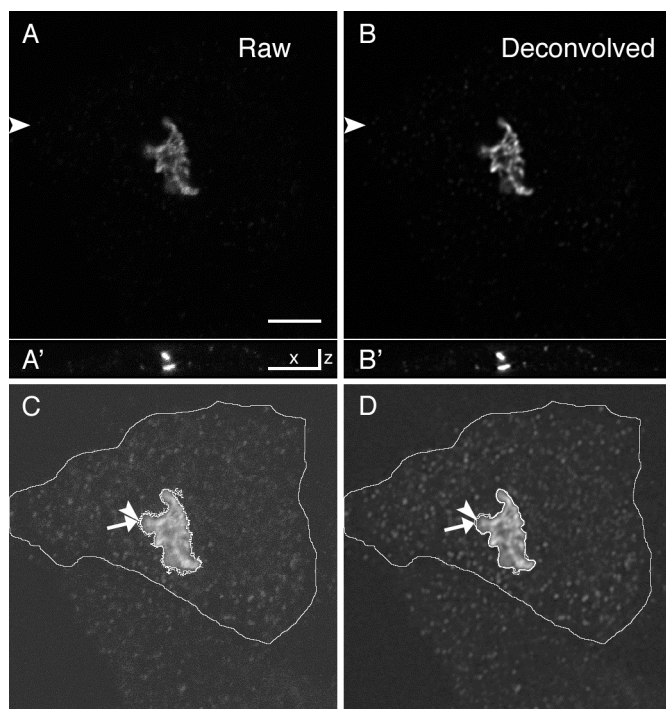


Figure 5. Laser scanning confocal images. A-B') Shown are slices in XY-plane (A, B) and XZ-plane (A', B') from image stacks of one HeLa cell expressing GalNAcT2-VSV and stained for VSV, imaged with a laser scanning confocal microscope (63x, 1.4 NA oil immersion objective, voxel volume: 60 nm x 60nm x 150nm). Identical cells are shown before (A, A') and after (B, B') deconvolution. The arrowheads in (A, B) correspond to the Y-position of the slices in (A', B'). To illustrate light spread better, the grayscale mapping was changed to 0-85 in (A', B') from 0-255 in (A, B). Bars, 5 μ m. C, D) Shown are identical slices from (A, B) with cell outlines and visual (arrowheads) and calculated (arrows) thresholds at gamma = 0.4. Note the overlap between the two thresholds in both images (C, D). Typically 40 XY-slices constituting a complete stack (~6 μ m in cell thickness) were analyzed.

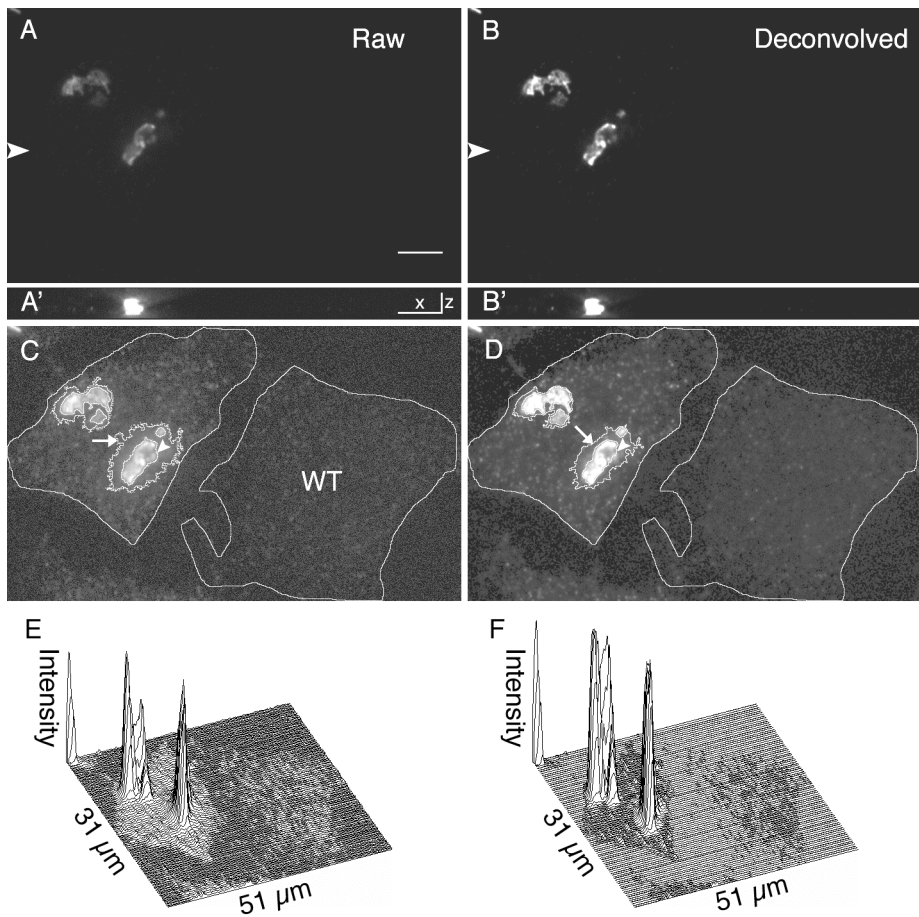


Figure 6. Spinning disk confocal images. A-B') Shown are representative slices in XY-plane (A,B) and XZ-plane (A',B') from image stacks of one HeLa cell expressing GalNAcT2-VSV and a neighboring wild-type HeLa fixed and stained for VSV, imaged with a Nipkow confocal microscope (100x, 1.4NA oil immersion objective, voxel volume: 72 nm x 72nm x 150nm). Identical cells are shown before (A, A') and after (B, B') deconvolution (10 iterations). The arrowheads in (A, B) correspond to the Y-position of the slices in (A', B'). Higher brightness (grayscale mapping of 100-1200 from 0-4095) was used in (A', B') to show light spread in the Z-direction. Bars, 5 μ m. C, D) Shown are identical slices from (A, B) with cell outlines and visual (arrowheads) and calculated (arrows) thresholds at gamma = 0.4. Typically 40 XY-slices constituting a complete stack (~6 μ m in cell thickness) were analyzed.

CHAPTER 4 – Quantification of GPP130 Trafficking through Endosomes

4.1 INTRODUCTION

The existence of retrograde transport along the biosynthetic and secretory pathways was first demonstrated in studies involving the retrieval of endoplasmic reticulum (ER) luminal proteins containing the KDEL sequence from post-ER compartments (Pelham et al. 1988). Similarly, Golgi proteins have also been shown to be involved in retrograde trafficking, both within the Golgi itself and cycling between the plasma membrane (PM) and the ER (Cole et al., 1996; Pelham, 2001; Storrie et al., 1998). In particular, several retrograde pathways between the endocytic route and trans Golgi network have been identified including late endosome to trans Golgi network (TGN) transport of mannose 6-phosphate receptors (Green and Kelly, 1992; Jin et al., 1989) and furin (Mallet and Maxfield, 1999). The more recently discovered pathway between the early endosomes and TGN suggests an alternative specialized route where proteins bypass the degradative environment of late endosomes (Mallard et al., 1998). The discovery of this pathway is especially important in the study of viral infection, and in particular toxins that utilize the cells retrograde transport machinery to travel from the PM to ER before infecting the cytosol (Mallard et al., 1998). Trans Golgi network protein of 46 kDa (TGN46) and the rat homolog TGN38 (TGN38) (Mallet and Maxfield, 1999), a TGN resident Golgi protein, have also been shown to utilize this pathway when cycling to and from the PM (Girotti and Banting, 1996). Characterized proteins that travel in this late endosomal bypass pathway have been either trans Golgi residents or receptor/ligands involved in the endocytic pathway. For this reason, the discovery of a cis Golgi localized protein that cycled between its steady-state distribution in the Golgi and early endosomes came as a surprise (Linstedt et al., 1997).

Golgi phosphoprotein of 130 kDa (GPP130) was first characterized in the Hauri laboratory as a type II transmembrane protein of unknown origin residing in the cis Golgi (Linstedt et al., 1997). It has a predicted molecular weight of ~82 kDa and is rich in acidic residues. This high concentration of acidic residues may explain the retarded mobility seen during SDS-PAGE migration, prompting researchers to assign a molecular weight of 130 kDa. Like most previously characterized Golgi integral membrane proteins, it has a short cytoplasmic domain (12 residue), a membrane-spanning domain (20 amino acid), and a large luminal domain (665 residue) (Linstedt et al., 1997). Unlike most Golgi resident transmembrane proteins, it has been shown to cycle to endosomes via the PM in response to an increase in the luminal pH of the Golgi by drugs such as monensin and bafilomycin (Linstedt et al., 1997; Puri et al., 2002). Upon drug washout and

restoration of pH, GPP130 has been localized back to the cis region of the Golgi. This pH sensitive cycling suggests the presence of selective Golgi and endosome targeting domains. GPP130 also appears to play a critical role as a mediator of endosome to Golgi trafficking of other proteins that utilize this pathway (Natarajan and Linstedt, 2004). GPP130 contains three mapped targeting domains in the coiled-coil segment of its lumen domain, adjacent to the membrane (Bachert et al., 2001). A single pH sensitive domain responsible for endosomal targeting is surrounded by two determinants mediating endosome to Golgi retrieval. Biotinylation of GPP130 at the cell surface was demonstrated in both monensin treated and untreated cells indicating some residence time at the surface (Puri et al., 2002). Additionally, uptake of exogenously added anti-GPP130 antibody confirmed the existence of GPP130 cycling to the plasma membrane (PM), while simultaneous uptake of anti-GPP130 and anti-TGN38 antibodies in the presence of monensin demonstrated their coincidence in the late endosome bypass pathway following endocytosis (Puri et al., 2002). Colocalization of GPP130 and internalized fluorescent dextran further validated the presence of GPP130 in endosomal structures (Linstedt et al., 1997; Puri et al., 2002). The identity of these endosomes was investigated using colocalization analysis of GPP130 with known early/recycling endosome (FITC-transferrin and transferrin receptor, EEA1), late endosome (mannose-6-phosphate receptor), and late endosome/lysosomes (LAMP2) (Linstedt et al., 1997; Puri et al., 2002). Although no coincidence was found, there was a high level of colocalization between GPP130 and TGN46 proteins during monensin induced redistribution, suggesting again the novelty of this newly discovered late endosome bypass pathway (Puri et al., 2002).

GPP130 has been shown to redistribute during both brefeldin A (Linstedt et al., 1997) and nocodazole treatments (Linstedt et al., 1997; Puri et al., 2002) in a manner similar to other Golgi integral membrane proteins, such as giantin and galactosyltransferase (GalT). Interestingly, in the presence of both nocodazole and monensin, GPP130 redistributes to the endosomes suggesting this cycling pathway to be dominant. Upon monensin washout, GPP130 resumes its dispersed nocodazole-induced distribution as evidenced by coincidence with giantin. Unlike the late endosome to Golgi trafficking pathway, these studies suggest the microtubule independent nature of this late endosomal bypass cycling pathway (Puri et al., 2002).

In this chapter we characterized the kinetics of GPP130 cycling along this late endosomal bypass pathway. Using monensin induced redistribution and subsequent washout, we quantified the transport of GPP130 between the endosomes and the Golgi apparatus. Collected data was

analyzed using a two-compartment kinetic model to fit simple transport rates. Inconsistencies between the monensin addition and washout calculated rate constants for the transport of GPP130 between the Golgi and endosomes were observed. An approximate 20 fold increase in the rate of transport to the endosomes was seen, suggesting monensin treatment may facilitate transport of GPP130 to the endosomes from the Golgi apparatus. Retrograde transport of Shiga toxin B-fragment was also characterized to validate our washout endosomal transport rate for GPP130. Finally, the spatial distribution of GPP130 retrograde trafficking from endosomes to Golgi was investigated with respect to cis and trans Golgi proteins as a first step in defining the return pathway. This work provides multiple approaches for studying the cycling of proteins in the late endosomal bypass pathway and contributes to the growing understanding of overall protein trafficking in the secretory pathway.

4.2 MATERIALS AND METHODS

4.2.1 Cell Culture

Wild-type (WT) HeLa cells were cultured in Dulbecco's Modified Eagle Medium (DMEM) supplemented with 10% fetal bovine serum (FBS, Hyclone, Logan, UT). HeLa cells stably expressing GalNAcT2-GFP (Storrie et al., 1998) were cultured in the presence of 0.45 mg/ml of geneticin sulfate (Sigma-Aldrich, St. Louis, MO). One or two days before studies were initiated, transfected cells were plated and grown to ~70% confluence in 100 mm polystyrene culture dishes containing 11 mm glass cover slips for fixation. All experiments were done in the presence of cycloheximide (CHX, Sigma St. Louis, MO) to inhibit protein synthesis. Cells were incubated with 100 µg/mL CHX for 30 minutes before beginning each experiment.

4.2.2 Antibodies and Reagents

Cells cultured on cover slips were either fixed with 3% formaldehyde and permeabilized with 0.1% saponin or fixed and permeabilized in cold methanol (-20°C) for 4 minutes. Fish skin gelatin was used as blocking reagent in all steps (Jiang and Storrie, 2005). WT or GalNAcT2-GFP expressing HeLa cells were stained with monoclonal antibodies against endogenous GPP130 (a gift from Dr. Adam Linstedt, Carnegie Mellon University) at 1:200 dilution and against endogenous p115 (Waters et al., 1992) at 1:100 dilution. Polyclonal antibodies against endogenous rab6 protein (Santa Cruz Biotechnology, Santa Cruz, CA) at 1:100 dilution, endogenous EEA1 (Santa Cruz Biotechnology, Sata Cruz, CA) at 1:100 dilution, and endogenous GM130 (BD Biosciences, San Jose, CA) at 1:200 dilution were also used. Cy3-conjugated donkey anti-rabbit or mouse IgG antibodies (Jackson ImmunoResearch Laboratories, West Grove, PA) at 1:1000 dilutions, Cy2-conjugated donkey anti-mouse IgG antibodies at 1:100 dilution, and Cy5-conjugated donkey anti-mouse IgG antibodies at 1:100 dilution were used as secondary antibodies. Cy3-conjugated Shiga toxin B-fragment (Tarrago-Trani and Storrie, 2004) was also used. The cover slips were mounted in buffered solution of the water-soluble plastic, Mowiol (Sigma, St. Louis, MO).

4.2.3 Widefield and Spinning Disk Confocal Microscopy

Single-plane widefield images were taken using a Zeiss Axiovert 200M microscope with 100x 1.4 NA objective and a Roper CoolSNAP HQ CCD camera (RoperPhotometrics, Tucson, AZ). The camera was operated at 1x1 binning. Spinning disk confocal image stacks were obtained using a CARV accessory (Atto Bioscience, Rockville, MD) mounted to the sideport of the Zeiss

Axiovert 200M microscope. A 100x 1.4 NA objective was used and images were captured to a Retiga EXi camera (QImaging, Burnaby, British Columbia, Canada). Illumination was with an X-Cite 120 light source (Hg-halide lamp, Exfo Life Sciences, Mississauga, Ontario, Canada). Nyquist oversampling criteria was met at 100 nm pixel size for single-plane widefield images and a voxel size of 72 nm x 72 nm x 150 nm for spinning disk confocal image stacks. The widefield images were taken at 0.150 s exposure time and a camera gain of 1 for Cy3-conjugated Shiga toxin. Exposure times for the endogenous GPP130, GalNAcT2-GFP, and Cy3-conjugated Shiga-toxin B fragment using the spinning disk confocal microscope were optimized per individual experiment to maximize the signal while minimizing photobleaching of the sample. All images were acquired as 12-bit data utilizing the maximum range possible of the available 4096 grayscales. Image capture software used was IPLab 3.9 (Scanalytics, Fairfax, VA) for Mac OS X.

4.2.4 Laser Scanning Confocal Microscopy

GalNAcT2-GFP cells were plated and fixed on glass cover slips and antibody stained for endogenous rab6, p115, and GPP130 as described above. Single plane images were taken on a Zeiss LSM 510 microscope using a 488 nm laser (5%) excitation with pinhole diameter set at 1 Airy unit (124 μm), a 561 nm laser (10%) excitation with pinhole diameter 1 Airy unit (122 μm), and 633nm laser (18%) excitation with pinhole diameter 1.12 Airy unit (122 μm). A 63x 1.4 NA objective was used with a zoom factor of 3 to achieve a voxel size of 100 nm x 100 nm. Twelve-bit single pass scanning with a pixel dwell time of 2.69 μs and averaging of 4 was used to minimize photobleaching while maximizing signal intensity.

4.2.5 Monensin Induced GPP130 Redistribution and Washout

GalNAcT2-GFP cells plated on glass coverslips were treated with CHX for 30 minutes prior to addition of 10 μM monensin (Calbiochem-Behring Corporation, La Jolla, CA). Coverslips were fixed in methanol for 4 minutes at -20°C and stained for endogenous GPP130 at 0, 5, 10, 15, 20, 30, 45, and 60 minutes after monensin addition. For the washout experiments, cells on glass coverslips were pre-treated with CHX for 30 minutes followed by monensin treatment for 1 hour. Coverslips were dipped in pre-warmed media 4x and transferred to complete media containing CHX (no monensin). The coverslips were fixed and stained for GPP130 at 0, 20, 40, 60, 90, and 120 minutes following monensin washout. Spinning disk confocal image stacks were acquired, as described above, for GPP130 and GalNAcT2-GFP simultaneously using the IPLab software Multi-D option.

4.2.6 Shiga toxin B-fragment Internalization

GalNAcT2-GFP cells plated on glass coverslips were treated with monensin for 1 hour before being transferred to individual wells of a 24-well plate containing ice cold CO₂-independent DMEM (Invitrogen, Carlsbad, CA) supplemented with 10% FBS and 10 mM monensin. 70 µg/mL of Cy3-conjugated Shiga toxin B-fragment was added to each well and the coverslips were incubated on ice for 30 minutes to allow binding of toxin to the surface. The cells were washed with ice-cold CO₂-independent media before adding warm (19.5°C) CO₂-independent media with monensin to each well. The plate was placed in a 19.5°C water bath for 1 hour to allow Shiga toxin to accumulate in the endosomes. The coverslips were dipped 4x in DMEM supplemented media and fixed with formaldehyde following 0, 10, 20, 30, 40, 45, and 60 minutes monensin and Shiga toxin washout. Also, cells treated with Shiga toxin in the absence of monensin were fixed at 0, 20, 40, and 60 minutes following washout. All steps were carried out in the presence of CHX. Spinning disk confocal image stacks were acquired for Cy3-conjugated Shiga toxin and GalNAcT2-GFP simultaneously using the IPLab software Multi-D option. Widefield microscope images of Cy3-conjugated Shiga toxin were taken for cells with and without monensin treatment.

4.2.7 Quantitative Analysis of GPP130

Following collection of confocal image stacks and deconvolution using Huygens Essential 2.7 software (Scientific Volume Imaging, Hilversum, The Netherlands), we analyzed the data to determine the fraction of GPP130 within the Golgi apparatus and endosomes. Colocalization analysis excluded any low intensity cytoplasm-ER signal and regions of low intensity light spread. The total intensity of GPP130 in the cytoplasm-ER, Golgi, and endosomes was calculated. With these intensities, the fractions of GPP130 in the endosomes and Golgi for the entire cell were calculated. This was accomplished as outlined in the procedure below.

For our analysis an endosome was defined using size criteria and as having GPP130 present but excluding GalNAcT2-GFP protein. In order to determine what was Golgi and what was endosomes, we used colocalization analysis with GalNAcT2-GFP as the Golgi marker. The instrument resolution in the z-dimension is ~ 500nm. However, per Nyquist sampling, the confocal image stacks used in this analysis were collected every 150 nm resulting in significant overlap between slices. This appears in the individual slices as light spread from adjacent planes. Although confocal pinhole and deconvolution technology eliminate the majority of this unfocused light from adjacent planes, there is still a small portion present that interferes with our

colocalization analysis (Figure 1). Signal from above or below the plane being analyzed (Figure 1 arrows) will produce false positives during the colocalization analysis and the true distribution of GPP130 in the endosomes will be misrepresented. For these reasons, it was necessary to use a stringent threshold during the colocalization analysis, one that would neglect the majority of the out-of-focus light, but include the signal for that plane.

To begin, the average background intensity for the cytoplasmic and non-cell regions were measured (B_{cyt} and $B_{non-cell}$, respectively). Background non-cell region is defined as an area outside of the cell, while the background cytoplasm was measured for a region not including Golgi or endosome signal (Figure 2). Using the average intensity/area background cytoplasmic values (B_{cyt}) for both the GalNAcT2-GFP and GPP130 channels, thresholds were calculated that would be used for the colocalization analysis. These thresholds correspond to ~3 times the cytoplasmic values (B_{cyt}) and were chosen so as to neglect the light spread mentioned above. Using the FCV-Colocalization function in IPLab, the degree of overlap between the GPP130 protein and GalNAcT2-GFP protein was determined. The colocalization algorithms in the IPLab software allows the user to set an intensity threshold for each channel individually and then identifies the location of each pixel where both channels exceed their defined thresholds simultaneously. The final result was a xy-pixel mask for each slice in the stack (Figure 3B) that was used to distinguish the regions in the original GPP130 image stack that are Golgi (colocalized with GalNAcT2-GFP) and endosomes (not colocalized with GalNAcT2-GFP). Using the mask as an overlay (Figure 3C), we summed the pixel intensities and areas of the GPP130 protein that colocalized with GalNAcT2-GFP ($GPP130_{cl\ int}$ and $GPP130_{cl\ area}$). We also measured the intensity and area of GPP130 for all the pixels above the colocalization threshold ($GPP130_{total\ int}$ and $GPP130_{total\ area}$). Using these measured values, background corrected intensities were calculated for the Golgi and endosome portions of GPP130 above the colocalization threshold ($GPP130_{cl}$ and $GPP130_{total}$, respectively).

$$\begin{aligned} GPP130_{cl} &= GPP130_{cl\ int} - (GPP130_{cl\ area} * B_{non-cell}) \\ GPP130_{total} &= GPP130_{total\ int} - (GPP130_{total\ area} * B_{non-cell}) \end{aligned} \quad (1\&2)$$

Using the background non-cell intensity/area measured previously ($B_{non-cell}$), the background intensity ($GPP130_{total\ area} * B_{non-cell}$) for the region was subtracted from the sum of the pixel intensities ($GPP130_{total\ int}$) in that region resulting in the background corrected total intensity of GPP130 above the colocalization threshold ($GPP130_{total}$). This background calculation ($GPP130_{cl}$

$\text{area} * B_{\text{non-cell}}$) was also subtracted from the sum of the pixel intensities in the colocalized mask region ($GPP130_{\text{cl int}}$). With these corrected intensities, the fraction of GPP130 in the Golgi and endosomes measured above the colocalization threshold were calculated (G_{cl} and E_{cl}).

$$G_{\text{cl}} = \frac{GPP130_{\text{cl}}}{GPP130_{\text{total}}} \quad (3&4)$$

$$E_{\text{cl}} = 1 - G_{\text{cl}}$$

The Golgi fraction of GPP130 (G_{cl}) is identified as the background corrected sum of the intensity of GPP130 that colocalized with GalNAcT2-GFP ($GPP130_{\text{cl}}$) divided by the background corrected sum of the total GPP130 intensity above the colocalization threshold ($GPP130_{\text{total}}$). The endosomal fraction (E_{cl}) is the remaining fraction of GPP130 above this threshold.

We note that our analysis assumes that GPP130 localized only to the Golgi apparatus and endosomes and no other organelle. We observed that at time zero monensin addition the colocalization analysis was identifying an unusually large portion of GPP130 in the endosomes. On closer inspection of the images, this high portion appeared to be an artifact caused by the presence of a pixel shift between the channels (Figure 3C arrow, see Appendix 3). To correct for this artifact, we subtracted the average endosomal fraction at time zero ($E_{\text{cl average @t=0min}}$) from all time points in the series ending with an adjusted endosomal fraction ($E_{\text{cl adjusted}}$). By definition, $E_{\text{cl adjusted}}$ is zero at time zero. This was also done for the monensin washout experiments using instead the average E_{cl} at the end of the washout (2 hours) for subtraction from all the data points. This adjusted portion was reattributed to the Golgi and the GPP130 Golgi fraction (G_{cl}) was adjusted accordingly ($G_{\text{cl adjusted}}$).

$$E_{\text{cl adjusted}} = E_{\text{cl}} - E_{\text{cl average @t=0m, 120m}} \quad (5)$$

As mentioned above, these calculated endosome and Golgi fractions ($E_{\text{cl adjusted}}$ and $G_{\text{cl adjusted}}$) are based on the measurement of pixels whose intensity exceeds a threshold defined with the intention of neglecting the light spread from adjacent planes. However, as shown in our previous work (Chapter 3, Rhee 2005), the true measured total intensity of a protein includes the light spread signal. Also, at the earlier monensin treatment and later monensin washout time points, the

colocalization threshold neglects the weak intensity GPP130 fraction of endosomes found in the cytoplasm (Figure 4A, C blue outline and arrowheads). For these reasons we next determined the total fractions of GPP130 in the Golgi, endosomes and cytoplasm of the cell. In Chapter 3, we showed that the average background cytoplasmic signal intensity (B_{cyt}) plus two standard deviations (stdev) was sufficient to define a threshold (Figure 4A, red outline) that would neglect the ER-cytoplasm portion of the protein while still including the light spread (Figure 4A arrow) signal attributed to the Golgi. Therefore, using the same method, a threshold was calculated to measure the total intensity of GPP130 in the Golgi and endosomes, including the light spread. Using this new lower threshold ($B_{cyt} + 2*stdev$), the GPP130 images were analyzed for the sum of the pixel intensities and areas ($GPP130_{lower\ int}$ and $GPP130_{lower\ area}$) above the threshold. The total intensity and area for the entire cell were also measured ($GPP130_{cell\ int}$ and $GPP130_{cell\ area}$, respectively). These total cell measurements include GPP130 signal for the entire cell (Golgi, endosomes, and cytoplasm) whereas the lower threshold measurements ($GPP130_{lower\ int}$ and $GPP130_{lower\ area}$) neglect the cytoplasmic portion of the signal. Our method allowed us to identify and measure Golgi and endosomal structures positive for GPP130 within the resolution of the microscope ($\geq 0.36 \mu m^2$) (Figure 4A, red outline). Note that because these lower threshold measurements include the light spread that was neglected with the previous colocalization threshold analysis, they are representative of the total protein present in the Golgi and endosomes. As before, the non-cell background was subtracted to give us the total protein intensity for the cell ($GPP130_{cell}$) and total intensity above the lower threshold ($GPP130_{lower}$).

$$\begin{aligned} GPP130_{cell} &= GPP130_{cell\ int} - (GPP130_{cell\ area} * B_{non-cell}) \\ GPP130_{lower} &= GPP130_{lower\ int} - (GPP130_{lower\ area} * B_{non-cell}) \end{aligned} \quad (6\&7)$$

The $GPP130_{lower}$ intensity measurement is a combination of the GPP130 located in both the Golgi and endosomes. In order to determine the individual protein intensities for these two regions, we used the relative fractions calculated during the colocalization analysis, $E_{cl\ adjusted}$ and $G_{cl\ adjusted}$. The total intensity of GPP130 in the Golgi, $GPP130_{Golgi}$, was calculated as follows:

$$GPP130_{Golgi} = G_{cl\ adjusted} * GPP130_{lower} \quad (8)$$

The remaining $GPP130_{lower}$ measured intensity is the endosomal portion, $GPP130_{endosome}$.

In addition to the Golgi and endosomal GPP130 signal measured above, we also used the lower threshold to measure the endosomal GPP130 found in the cytoplasm (structures $\sim 0.23 - 0.36 \mu\text{m}^2$ in size) (Figure 4A and C, blue outline and arrowheads). After measuring the intensity and area of GPP130 in these structures ($\text{GPP130}_{\text{small int}}$ and $\text{GPP130}_{\text{small area}}$), we subtracted the non-cell background to determine the total GPP130 intensity for these small endosomes ($\text{GPP130}_{\text{small}}$).

$$\text{GPP130}_{\text{small}} = \text{GPP130}_{\text{small int}} - (\text{GPP130}_{\text{small area}} * \text{B}_{\text{non-cell}}) \quad (9)$$

The total intensity of GPP130 in the endosomes is the sum of the $\text{GPP130}_{\text{small}}$ and $\text{GPP130}_{\text{endosome}}$ intensities.

Using all of these background corrected measured intensities ($\text{GPP130}_{\text{cell}}$, $\text{GPP130}_{\text{Golgi}}$, $\text{GPP130}_{\text{small}}$, and $\text{GPP130}_{\text{endosome}}$), we calculated the fraction of GPP130 in the endosomes (N_{GPP130}), the Golgi (G_{GPP130}), and the ER ($\text{ER}_{\text{GPP130}}$).

$$\begin{aligned} \text{N}_{\text{GPP130}} &= \frac{\text{GPP130}_{\text{small}} + \text{GPP130}_{\text{endosome}}}{\text{GPP130}_{\text{cell}}} \\ \text{G}_{\text{GPP130}} &= \frac{\text{GPP130}_{\text{Golgi}}}{\text{GPP130}_{\text{cell}}} \\ \text{ER}_{\text{GPP130}} &= 1 - \text{G}_{\text{GPP130}} - \text{N}_{\text{GPP130}} \end{aligned} \quad (10, 11, \& 12)$$

It should be noted that the limitations associated with light microscopy make it difficult to identify and ultimately determine what this ‘cytoplasmic-ER’ portion of GPP130 is. No discernable structure was evident (Figure 4B) and this signal likely reflects low-level non-specific binding of the primary antibody. Thus, we neglected this ‘cytoplasmic-ER’ portion of GPP130 signal as non-specific staining. This assumption requires that the final fractions of GPP130 in the Golgi and endosomes be adjusted to exclude this portion of signal ($\text{G}_{\text{GPP130, final fraction}}$ and $\text{N}_{\text{GPP130, final fraction}}$).

$$\begin{aligned} \text{G}_{\text{GPP130, final fraction}} &= \frac{\text{G}_{\text{GPP130}}}{(\text{N}_{\text{GPP130}} + \text{G}_{\text{GPP130}})} \\ \text{N}_{\text{GPP130, final fraction}} &= \frac{\text{N}_{\text{GPP130}}}{(\text{N}_{\text{GPP130}} + \text{G}_{\text{GPP130}})} \end{aligned} \quad (13\&14)$$

4.2.8 Quantitative analysis of Shiga toxin

The endosomal and Golgi fractions of Cy3-conjugated Shiga toxin were calculated in a manner similar to GPP130 quantification. The average cytoplasmic intensity of Shiga toxin and GalNAcT2-GFP were measured and used to define colocalization thresholds. Shiga toxin transports to the ER after exiting the Golgi, so the measured intensity in the cytoplasm/ER at the later time points was stronger than the endogenous protein signal seen in non-infected cells above, making it unnecessary to define separate colocalization and lower thresholds for the quantification of Shiga toxin in the Golgi and endosomes over time. Colocalization analysis was performed using the FCV software and the calculated thresholds for both GalNAcT2-GFP and Shiga toxin proteins, similar to above. The cytoplasmic/ER portion was neglected completely. Therefore, the measured amount of Shiga toxin that did not colocalize with GalNAcT2-GFP was used to determine the fraction of toxin in the endosomes and these fractions were plotted versus time, similar to the GPP130 analysis.

For the widefield microscopy analysis of Shiga toxin transport with and without monensin, the images were randomly scored to identify cells where the majority of the Shiga toxin was located in either the endosomes or Golgi. A cell was defined as having a majority of endosomal localized toxin if greater than ~50% of the toxin was localized to the endosomes during a visual analysis. At least 36 cells were analyzed for 0, 20, 40, and 60 minutes following washout for cells with and without monensin added. For each experiment ($n=3$), all time point images were opened and cells scored as either Golgi or endosome positive before tabulating the relative fraction of cells positive for GPP130 endosomal distribution.

4.2.9 Endosomal Markers: EEA1 and Cascade-blue dextran

Wild-type HeLa cells plated on glass coverslips were treated for 30 minutes with CHX prior to initiation of each experiment and CHX was present throughout incubation. Cells were incubated with and without monensin for 10 minutes followed by incubation with 1mg/mL of cascade blue-dextran for 20 and 40 minutes. The coverslips were dipped 4x in PBS and incubated for 10 minutes in the presence of monensin and absence of dextran before being fixed with formaldehyde and stained for GPP130 and early endosomal marker EEA1 (Bachert et al., 2001; Linstedt et al., 1997).

4.2.10 Quantitative Analysis of LSM510 images

GalNAcT2-GFP cells stained for a combination of 1) p115 and rab6, 2) GPP130 and rab6, and 3) GM130 with two distinct secondary antibodies were imaged using the LSM510 confocal microscope. The GM130 images were used to determine pixel shift distance between the Cy3 and Cy5 channels. Single plane images of GPP130, rab6, and p115 were analyzed for distance between peak intensities along a line drawn perpendicular to the Golgi ribbon. The plane with the brightest rab6 Golgi staining was selected for analysis. The pixel intensities along the line for both rab6-p115 costaining and rab6-GPP130 costaining were plotted versus distance and the distances between peaks measured. Two separate distance measurements per cell for each of the costaining experiments were taken for 30 cells at 0, 20, and 60 minutes following monensin washout. These profile distances between major peaks for each protein were averaged and plotted at each time to identify trends. Also, GPP130-rab6 line profiles were analyzed for the presence of a minor secondary GPP130 peak. For the fraction of profiles exhibiting a minor GPP130 peak, the distance between this secondary GPP130 peak and the primary GPP130 peak identified previously was measured. The fraction of the peak intensity of the secondary peak with respect to the primary GPP130 peak intensity was also calculated as the ratio of the secondary peak intensity to the sum of the peak intensities of the primary and secondary peaks.

4.2.11 Statistics

All monensin redistribution, washout, and Shiga toxin experimental results are reported as the mean \pm standard error of three independent experiments. The LSM510 spatial results are the mean \pm standard error for two independent experiments. Statistical analysis for significance was performed using a student t-test with two-tailed distribution and two samples with equal variance (Microsoft Excel software).

4.3 RESULTS

4.3.1 GPP130 Golgi protein cycles between the endosomes and Golgi apparatus

GPP130, a cis localized Golgi protein, has been shown to cycle between the Golgi apparatus and endosomes via the plasma membrane (Linstedt et al., 1997) and appears to play a critical role in the early endosomal bypass pathway as a mediator of endosome to Golgi trafficking of other proteins that utilize this pathway (Natarajan and Linstedt, 2004). Both the presence and importance of GPP130 within this cycling pathway suggests the existence of a steady-state pool of GPP130 in the endosomes and we thus sought to quantify this pool using fluorescent microscopy. Cells stably transfected to express GalNAcT2-GFP protein were fixed and stained for endogenous GPP130 and confocal image stacks of both proteins were analyzed for the presence of endosomal structures positive for GPP130. There is no evidence that the GalNAcT2-GFP protein cycles between the Golgi and endosomes making it an appropriate marker for the Golgi apparatus (Röttger et al., 1998). GPP130 intensity was evident in the Golgi apparatus, which co-stained with GalNAcT2-GFP (Figure 5A, B, C). However, GPP130 signal in endosomal structures at steady-state was evident but weak and difficult to distinguish from the general background signal. Therefore, intensity and size thresholds were used to distinguish regions positive for GPP130 from cytoplasmic/ non-specific antibody staining. The intensity threshold used was the average cytoplasm intensity plus two standard deviations of the individual pixel values in this region (Rhee et al., 2005). A size criterion range of ~0.23 to 0.36 μm^2 was employed in order to exclude large Golgi-like structures and smaller noise-like structures. Using these criteria, a small measurable portion of GPP130 (~1%) was found in the endosomes at steady-state which is more evident when the images are mapped appropriately (Figure 5A'). These structures were negative for GalNAcT2-GFP verifying their non-Golgi localization (Figure 5 C, C'). The images presented in Figure 5A', B', C' are normalized to a smaller grayscale range so that the endosomal structures are easier to visualize.

4.3.2 Monensin induces redistribution of GPP130 to endosomes

Addition of the drug monensin has been shown previously (Linstedt et al., 1997) to lead to a reversible accumulation of GPP130 in endosomal like structures and this was confirmed in our cells (Figure 6D, G). The identity of these non-Golgi, GPP130 positive structures was verified using uptake of fluorescent dextran as a marker for endosomes (Linstedt et al., 1997; Thilo et al., 1995). Cells treated with (Figure 6 D-F) and without (Figure 6 A-C) monensin were incubated in the presence of cascade blue dextran as described in the Material and Methods section. The

increased endosomal concentration of GPP130 in the presence of monensin makes it possible to identify structures positive for both GPP130 and internalized dextran (Figure 6F). We were unable to see any colocalization in the absence of monensin (Figure 6C). We note that our data suggests specificity to this localization as co-staining for GPP130 (Figure 6G) and the early endosomal marker EEA1 (Figure 6H) showed no colocalization (Figure 6I), similar to results published by the Linstedt laboratory (Linstedt et al., 1997).

4.3.3 Kinetic Analysis of GPP130 Cycling between Golgi and Endosomes

Redistribution of GPP130 to the endosomes was apparent within 60 minutes following monensin treatment. The Golgi localization of GPP130 (Figure 7A) at time zero was confirmed by its colocalization with GalNAcT2-GFP protein (Figure 7D) in the same cell. Redistribution was readily apparent by 30 minutes (Figure 7B) and appears to be maximal by 60 minutes (Figure 7C). During this GPP130 redistribution, GalNAcT2-GFP remained localized centrally within the cell in the Golgi region (Figure 7E, F). Cycling of GPP130 between Golgi and endosomes following monensin addition was quantified and ultimately used to determine kinetic rate measurements.

A two-compartment kinetic model connected by first order processes was used to represent transport between the Golgi and endosomal population (Figure 8). Although GPP130 most likely cycles to the ER similar to other Golgi resident proteins, as shown from brefeldin A addition experiments (Puri et al., 2002), this pool was neglected in the model as it has not been conclusively shown to reside in the ER at steady-state. Similarly, the possibility that GPP130 was transported to the plasma membrane before arriving in endosomes was included in the forward rate, k_1 , as surface levels of GPP130 were undetectable. Assuming no new protein generation and that the transport between compartments was much shorter than the life span of the protein, the change in endosome resident proteins as a function of time can be described by:

$$\begin{aligned} \frac{dE}{dt} &= k_1 G - k_{-1} E \\ 1 &= G + E \\ \frac{dE}{dt} &= k_1(1 - E) - k_{-1} E \end{aligned} \tag{15,16, &17}$$

where E and G are the relative concentrations of proteins in the endosomes and Golgi, respectively, and k_1 and k_{-1} are the rate constants for transport in the Golgi to endosome and

endosomes to Golgi directions, respectively. The general solution of the above differential equation (17) can be written as:

$$E(t) = \left(\frac{k_1}{k_1 + k_{-1}} \right) + C \exp[-(k_1 + k_{-1})t] \quad (18)$$

where C is a constant of integration and can be determined from the initial conditions. The steady-state solution, E_{ss} , is given by:

$$E_{ss} = \frac{k_1}{k_1 + k_{-1}}. \quad (19)$$

In the presence of monensin, GPP130 accumulation in the endosomes was quantified as described previously in Materials and Methods, and k_{-1} was neglected. The simplified rate equation is described by:

$$E(t) = 1 + C \exp(-k_1 t) \quad (20)$$

The endosome fraction versus time was quantified using the method outlined in Materials and Methods (Figure 9). The Golgi pool of GPP130 was never completely depleted, with only $\sim 50\%$ of the protein relocating to the endosomes in the presence of monensin (Figure 9). Redistribution of GPP130 to the endosomes was apparent within 10 minutes of treatment (Figure 10A arrows) with the redistribution appearing to be maximal within the hour. Extended treatment of the cells did not significantly affect the measurable fraction of GPP130 present in the endosomes, but did alter the spatial distribution of the endosomes relative to the Golgi. At earlier treatment times (0-60 minutes), the endosome population was primarily located in the periphery of the cell (Figure 10C) making it easier to distinguish from the Golgi. However, at time points greater than 90 minutes, the endosomes clustered near the Golgi (Figure 10E) hindering our ability to distinguish the two separate populations. For these reasons, data was collected and analyzed for time points between 0 and 60 minutes following monensin treatment. Again, GalNAcT2-GFP was used as a Golgi marker and its steady-state localization was not affected in the presence of monensin (Figure 10B, D, F). The transport data was analyzed and an average forward rate of $0.013 \pm 0.001/\text{min}$ for three independent experiments was determined. Using k_1 and the measured steady-state endosomal fraction of $\sim 1\%$, the model predicts a retrograde trafficking rate of k_{-1} of

1.28/min, an almost 100x increase in transport. If indeed $k_{-1} \gg k_1$, it would indicate a short residence time in the endosomes and explain the difficulty in visualizing endosome concentrations of GPP130 at steady-state. The reciprocals of the measured anterograde and calculated retrograde rates yield mean residence times of ~77 minutes in the Golgi and ~0.8 minutes in the endosomes for the GPP130 protein at steady-state.

GPP130 redistribution was reversible upon monensin washout making it possible to study the retrograde transport kinetics of GPP130 from endosomes to Golgi (Puri et al., 2002). Washout induced trafficking of GPP130 to the Golgi is illustrated in Figure 11 at 0, 20, and 120 minutes (Figure 11, A, B, C, respectively). GalNAcT2-GFP was used to identify the Golgi (Figure 11D, E, F). Quantification of the loss of GPP130 protein from the endosomes during monensin washout was monitored and results plotted using KaleidaGraph (Synergy Software) (Figure 12) to determine both the forward and reverse rates from a fit of equation (18) above. The reverse rate from three independent experiments was determined to be $0.034 \pm 0.010/\text{min}$, a value not in agreement with the predicted k_{-1} from the monensin redistribution experiments. Two possible explanations for this discrepancy are 1) that monensin addition affects forward trafficking of GPP130 and the measured k_1 is not representative of the steady-state rate, or 2) the simple model used to describe the transport is incomplete, and critical steps or components mediating the phenomena are not included. The anterograde rate calculated from a fit of the washout data yielded a k_1 value of $0.0006 \pm 4.08 \times 10^{-6}/\text{min}$. This rate was significantly smaller, approximately 20 fold, than the result measured in the monensin redistribution experiments reported above of $0.013/\text{min}$.

4.3.4 Shiga toxin B-Fragment Traffics from Endosomes to Golgi

Given the difference between the measured and predicted rates for the anterograde and retrograde transport of GPP130, trafficking of a different protein that uses the same endosome to Golgi pathway was investigated. Not only do GPP130 and Shiga toxin appear to utilize the same bypass pathway, research has shown that GPP130 is required for the efficient exit of Shiga toxin B-fragment from endosomes en route to the Golgi (Natarajan and Linstedt, 2004). Cy3-conjugated Shiga toxin B-fragment was allowed to accumulate in the endosomes of GalNAcT2-GFP cells using a temperature block (Natarajan and Linstedt, 2004) in the presence of monensin, similar to the GPP130 washout experiments. Following the washout of monensin and increase to 37°C , the Shiga toxin fragment was evident in the Golgi based on colocalization with GalNAcT2-GFP (Figure 13). Exit of Shiga toxin B-fragment from the endosomes was quantified with respect to

time for three independent experiments (Figure 14). Again, GalNAcT2-GFP was used as a marker for the Golgi and colocalization analysis between Shiga toxin and GalNAcT2-GFP was performed as described in Materials and Methods. Assuming no recycling into the endosomes, the endosomal portion of Shiga toxin fragment, E(t), at time t is described by:

$$E(t) = C \exp(-k_{-1}t) \quad (20)$$

where k_{-1} is the retrograde rate constant and C is a constant of integration that can be found using initial conditions. The average rate of Shiga toxin endosome to Golgi transport for the three separate experiments was found to be $0.034 \pm 0.007/\text{min}$, in agreement with the previously reported GPP130 monensin washout result (Table 1). To verify the transport was unaffected by monensin, the distribution of Shiga toxin B-fragment in the endosomes and the Golgi was also analyzed in the absence of monensin. The fraction of cells ($n > 36$) showing predominantly endosome localized B-fragment was determined as a function of time following treatments with and without monensin and subsequent washout (Figure 15). Average values for three independent experiments showed no significant difference suggesting that monensin had no discernable affect on the transport of Shiga toxin from the endosomes to the Golgi. Results also suggest that endosomal clearance is slow and therefore Golgi to endosome trafficking of GPP130 must be negligible.

4.3.5 Cisternal localization of retrograde trafficking GPP130 following monensin washout

Our data and that of others (Bachert et al., 2001; Puri et al., 2002; Puthenveedu et al., 2003) suggest that GPP130 does return to the Golgi apparatus following monensin washout and, as noted above, the literature (Natarajan and Linstedt, 2004) suggests that GPP130 may be a pivotal protein in this endosomal-Golgi pathway. The return transport route of cis Golgi localized GPP130 following its exit from the endosomes is therefore important to determine and was next investigated. Similar to GPP130, TGN38/46 and Shiga toxin both utilize the early endosomal bypass pathway (Natarajan and Linstedt, 2004). TGN38/46, a trans Golgi network (TGN) resident protein, returns to the TGN following endosomal exit, while Shiga toxin has also been shown to return to the Golgi following exit from endosomes as evidenced by its colocalization with TGN38/46 during transport between the plasma membrane and trans Golgi network (Mallard et al., 1998). The specifics of transport for these proteins from the endosomes to Golgi are still unknown. Using laser scanning confocal technology, we developed a novel approach for investigating the intra-Golgi spatial distribution of GPP130 during retrograde transport back to

the cis Golgi. Using rab6 and p115 as trans and cis Golgi markers respectively, we measured the relative distances between these proteins as well as GPP130 following monensin washout.

GalNAcT2-GFP cells stained with rab6 and either p115 or GPP130 were imaged using the LSM510 laser scanning confocal microscope. Using the profile function available with the LSM510 software, the intensities of the two proteins were plotted along a line perpendicular to the Golgi (Figure 16 and Figure 17). The distances between peak intensities for the two proteins along these lines were measured for 30 cells at 0, 20, and 60 minutes following monensin washout. Two profiles per cell were measured and the average distance values reported in Table 2. GalNAcT2-GFP was used as a general Golgi marker, and as evident in Figure 16, was relatively evenly distributed across the distance between the GPP130 primary peak and the rab6 peak. Despite pooling of GPP130 in the endosomes during monensin treatment, a large population of GPP130 protein remained in the Golgi and was identifiable as a large primary peak of intensity in our images (Figure 16A, D). Distinguishing between the existing Golgi localized GPP130 and newly arriving protein was difficult. However, we found that a secondary smaller peak localized closer to the rab6 protein was evident in many of the cells analyzed (Figure 16D). Secondary peaks were not evident in either the rab6 or p115 profiles, both of which do not cycle to the endosomes (Figure 17). The distance between the secondary GPP130 peak and the rab6 peak were measured as well as the fraction of secondary peak intensity with respect to the primary GPP130 peak (Tables 2 and 3). There was a general decrease in the distance between cis (p115 and the primary peak of GPP130) and trans peak of rab6 (Table 2) during monensin washout and is most likely due to the slight vesicle swelling associated with monensin treatment (Dinter and Berger, 1998). Also, the average distances between the cis localized primary GPP130 peak and p115 peak are significantly different ($p<0.05$) and are consistently separated for the three time points during monensin washout. Note that the primary GPP130 peak is closer in distance to p115 than rab6, verifying its cis localization (Table 2). Golgi associated protein p115 is actually a resident of the cis-Golgi network (CGN) known to cycle between the CGN and cis Golgi (Garcia-Mata et al., 2003), which may explain the small, but consistent separation of p115 and primary GPP130. The secondary GPP130 peak distances were significantly closer to the rab6 peak (Table 2) although the fraction of total cells displaying a secondary GPP130 peak was variable (Table 3). Also, the intensity fraction of GPP130 in the secondary peaks is reported in Table 3 and surprisingly, was not altered with respect to time. This result may be a reflection of the single plane/ single line artifact or non-inclusiveness of the analysis.

4.4 DISCUSSION

The cycling rates of Golgi protein GPP130 were measured and characterized in the late endosome bypass pathway with the purpose of providing a better understanding of the trafficking kinetics of proteins along this route. For the first time, we present a complete analysis of GPP130 protein cycling along this pathway using quantitative confocal stack analysis. In agreement with previous work (Linstedt et al., 1997; Puri et al., 2002), we found that under normal tissue culture conditions there was little GPP130 outside the Golgi apparatus with ~ 1% in the endosomes at steady-state. Using monensin treatment to inhibit exit of GPP130 from the endosomes, we found that ~ 50% was localized to the endosomes after 1 hour and using a two-compartment model, we measured a transport rate of 0.013/min from the Golgi to endosomes. This rate was faster than anticipated from the steady-state value and indicated a residence time in the endosomes of less than 1 minute. Parallel experiments measuring transport back to the Golgi yielded a return rate of ~ 0.034 and a forward transport rate of ~ 0.001/min. Surprisingly, the forward and retrograde measured rates were not in agreement with respect to predicted steady-state rate calculations. The presence of monensin may be responsible for a shift in the steady-state distributions and explain the inconsistency of our measured rates. Monensin is an ionophore drug capable of neutralizing the intracellular environment of cells in culture, thereby causing a block in secretion at the cellular level (Tartakoff and Vassalli, 1977). It has been shown to cause either partial or complete block of secretion at the plasma membrane for certain proteins and lipids (Andrieu et al., 1996; Herscovitz et al., 1995; Kallen et al., 1993), while other secretory products were expressed at the plasma membrane, but incompletely processed (Furukawa et al., 1992; Mollenhauer et al., 1990). Examples of the effect of monensin on secretion have been shown in multiple cell lines and in both plants and animals (see (Dinter and Berger, 1998) for review).

Alternatively, the model used for our analysis may be incomplete, neglecting the possibility of a limiting step. Transport in the secretory pathway involves the cooperation and recruitment of multiple proteins such as, for example coat proteins (Lee et al., 2004). Recruitment of an additional protein necessary for the transport of GPP130 may be limiting the trafficking of GPP130-protein complex under the experimental conditions tested. The limited availability of this complex protein may be responsible for altering the kinetics of normal GPP130 trafficking between the Golgi and endosomes. Shiga toxin B-fragment trafficking was also investigated as we sought to verify the transport rate of a protein traveling from endosomes to Golgi along this pathway. Although the two rates from the Shiga toxin fragment and GPP130 monensin washout experiments were in agreement, concerns regarding the validity of the model as an accurate

representation of steady-state cycling exist in both model systems, namely the accumulation of toxin in the endosomes and the presence of monensin. Accumulation of protein in the endosomes prior to washout analysis results in an experimental system that is unlike the steady-state distribution of GPP130. However, visualization of a quantifiable pool of toxin makes the need for accumulation of cargo in the endosomes prior to analysis necessary. Secondly, both sets of experiments were done in the presence of the drug monensin, which has been shown to morphologically alter the intracellular environment. However, with the Shiga toxin fragment experiments we showed that there was no change in overall toxin distribution in cells with or without monensin added, suggesting that monensin did not affect the retrograde transport of the toxin fragment directly. Therefore, the questions remain; what is the correct steady-state rate of cycling GPP130 in the late endosome bypass pathway and is our quantitative analysis of the rates representative of steady-state?

Assuming the two-compartment model is an accurate representation of steady-state trafficking, two possibilities exist to explain the variability of our data, 1) the rate of transport to the endosomes is accelerated in the presence of monensin, or 2) the return rate of transport from endosomes to Golgi is delayed. The presence of an accelerated rate of GPP130 cycling to the endosomes could be a peripherally associated result of monensin addition. However, literature cites multiple examples of evidence contrary to this accelerated rate, instead supporting the possibility of an inhibition of protein transport through the Golgi complex (Dinter and Berger, 1998). Monensin has been shown to alter the secretion and surface expression of multiple proteins (see (Dinter and Berger, 1998) for review). The effect of monensin in the Golgi is usually manifested as the partial or complete retention of the protein in the organelle or as a block in expression at the cell surface. The unique pH sensitive properties of GPP130 may cause its cycling properties to be more susceptible to monensin treatment compared to the newly synthesized proteins and more conventional Golgi resident transmembrane proteins. The precise effects of monensin on GPP130 cycling remain to be seen, as the exact nature and function of GPP130 are still mostly unknown (Linstedt et al., 1997). Evidence presenting the possibility of trafficking and sorting proteins in the recycling/sorting endosome compartment following TGN exit but prior to transport to the plasma membrane may provide another explanation for the accelerated rate of GPP130 redistribution as seen in our experiments. The TGN has been presumed to be the sorting site for all newly synthesized proteins trafficking in the secretory pathway (Griffiths and Simons, 1986; Hirschberg et al., 1998; Keller et al., 2001; Rindler et al., 1985). However, previous evidence from polarized cells has suggested the possibility that

secretory traffic can transverse endocytic compartments before trafficking to the plasma membrane (PM) (Orzech et al., 2000; Stoorvogel, 1998). Perhaps GPP130 accumulates in recycling endosomes during monensin addition and the rate measured during our kinetic analysis is the result of this abbreviated cycling. Biotinylation (Puri et al., 2002) experiments suggest plasma membrane trafficking and argue against this possibility, but perhaps the accumulation of GPP130 in endosomal structures seen in the micrographs is a combination of both recycling and late endosome bypass pathway endosome populations. Also, the extended incubation (20 and 40 minutes) of the cells in the presence of the fluorescent dextran could result in late endosomal staining. The fraction of endosomes exhibiting co-staining between GPP130 and dextran was small, supporting the possibility of a mixed population of early to late endosomes.

Alternatively, the trafficking between the endosomes and Golgi could be affected in the presence of the drug during our experiments. If this were the case, a delayed return transport rate is unlikely the direct result of monensin, as evidenced by lack of a monensin pretreatment effect on Shiga transport cycling (above results). The presence of slowed protein transport between the endosomes and Golgi is more likely the consequence of a limiting factor involved in endosomal exit. A possible effect of pH neutralization is the inability of the receptor to dissociate from the protein (Dinter and Berger, 1998; Marnell et al., 1982). Dissociation of the ligand from the receptor may not occur in the neutralized pH environment therefore retaining the entire complex in the endosome, and suggesting a role for receptor-ligand association in the retention of GPP130 and Shiga toxin fragment protein in endosomes as seen in our experiments (Dinter and Berger, 1998).

The exaggerated presence of GPP130 in the endosomes prior to monensin washout may also explain a delay in transport back to the Golgi upon monensin washout and subsequent return to an acidic environment. As mentioned above, the recruitment of a limiting factor necessary for transport from the endosomes to the Golgi may be restricting the exit of the accumulated GPP130 in the endosomes and subsequent transport back to the Golgi. Given the necessity of accumulation of protein in the endosomes prior to washout in order to ensure quantitatively measurable quantities, it is difficult to determine the rate of transport to the Golgi under normal conditions. Overexpression of GPP130 has also been shown to induce redistribution of the protein to punctate endosomal like-structures (Linstedt et al., 1997). This makes the possibility of a fluorescently tagged fusion GPP130 protein system unlikely because overexpression of the protein and tag is necessary when developing a chimeric cell line.

The spatial properties of intracellular proteins have previously been studied using a variety of methods, including stereology, high-resolution electron microscopy, and fluorescence resonance energy transfer (FRET). Distances between proteins in mitochondria have been measured using stereology (Schwerzmann et al., 1986), while FRET has been used to measure protein-protein interaction distances of bacterial toxins (Majoul, 2004). Due to the high-resolution nature of electron microscopy, the micrographs can also be used to determine the distances between organelles and protein labeled dense regions within. With this chapter, a novel method for the study of spatial protein distributions during kinetic analysis is presented. The LSM analysis of GPP130 return cycling to the Golgi with respect to trans and cis Golgi proteins provided information on possible retrograde cycling properties of GPP130. In particular, the secondary GPP130 peak distance analysis showed the presence of a GPP130 population localized in the trans region as evidenced by its colocalization with rab6, suggesting the possibility of a trans entry point prior to transport to the cis Golgi. However, not all cells sampled displayed a secondary GPP130 peak, with the fraction varying depending on the time point. As shown in Table 3, the fraction of cells with a secondary GPP130 peak was greatest at the 20 minute washout time, while the smallest portion was found at the 60 minute time point when washout is assumed complete and the majority of the protein is localized to the cis Golgi region. These observations may be a result of the three-dimensional conformation of the Golgi in the cell as well as the limited analysis of a single slice of the cell. When the cell is fixed on the coverslip the organelles are set in place. When the cells are imaged, the Golgi is visible in the spatial conformation in which it was fixed, which differs from cell to cell and may make it difficult to visualize all regions of the Golgi. Considering the assumption that retrograde cycling is essentially blocked during monensin addition, the large fraction of cells displaying trans localized GPP130 at 0 minute monensin washout was surprising (Table 3). It is possible that this 0 minute monensin washout trans localized pool of GPP130 is actually caused by the back up of anterograde cycling protein. Because the specifics of transport to the endosomes are not completely understood, the accumulation of GPP130 in the trans region may represent protein waiting to transport to the endosomes. This accumulation may also suggest that there are limiting factors in the anterograde transport of GPP130 to the endosomes and that it is this forward pathway that is saturated, not the exit from the endosomes. Note that the increase in the cell fraction having secondary peaks at 20 minutes following monensin washout may represent the returning fraction of GPP130, but as there are also peaks present at 0 and 60 minutes more investigation is needed before a reliable conclusion can be drawn.

In conclusion, the work presented in this chapter has provided valuable information concerning the kinetic cycling properties of cis Golgi protein GPP130. These results combined with the preliminary data concerning the spatial trafficking properties of GPP130 have contributed to the general knowledge of intracellular trafficking in the secretory pathway and the late endosomal bypass pathway in particular.

Table 1. Comparison of kinetic rate constants for protein transport between the Golgi and endosomes.

Experiment	k_1 (min ⁻¹)	k_{-1} (min ⁻¹)
Monensin Addition (GPP130)	$1.3 \times 10^{-2} \pm 1.0 \times 10^{-3}$	NA
Monensin Washout (GPP130)	$6.3 \times 10^{-4} \pm 4.1 \times 10^{-6}$	$3.4 \times 10^{-2} \pm 1.0 \times 10^{-2}$
Shiga Toxin	NA	$3.4 \times 10^{-2} \pm 7.0 \times 10^{-3}$

HeLa cells expressing GalNAcT2-GFP were fixed and stained for GPP130 (Monensin Addition and Washout) and imaged as stacks using spinning disk confocal microscopy. Cells ($n \geq 10$) were analyzed for three independent trials as described in Materials and Methods for each of the experimental conditions listed above. Fraction of protein (GPP130 or Shiga toxin) in the endosomes was quantified and the results listed are the rate constants for the anterograde (k_1) and retrograde (k_{-1}) trafficking of protein between the Golgi apparatus and endosomes (mean \pm SEM).

NA (non applicable) - Shiga toxin does not cycle from Golgi to endosomes

Table 2. Distance Measurements for rab6, p115, and GPP130

Protein	Δ Distance (rab6-protein) (μm)		
	0 min	20 min	60 min
p115 (cis)	0.82 ± 0.01	0.74 ± 0.01	$0.65 \pm 0.01^*$
primary GPP130 (cis)	0.62 ± 0.04	0.55 ± 0.07	0.46 ± 0.01
secondary GPP130 (trans)	0.06 ± 0.01	0.02 ± 0.02	0.07 ± 0.00

Distance measurements between rab6 and proteins listed at 0, 20, and 60 minutes following monensin washout. Both primary and secondary peaks for GPP130 were analyzed with secondary peaks being characterized by their colocalization with rab6. Results represented are mean \pm SEM ($n=2$ independent experiments of 30 cells each).

p115 and secondary GPP130 distance measurements were significantly different from primary GPP130 distance measurements at all time points as determined from a Student t-test ($p < 0.05$).

* Indicates significant difference between 0 minute p115 distance measurement as determined from Student t-test ($p < 0.05$).

Table 3. Secondary GPP130 Peak Analysis

Secondary Peak Measurement	0 min	20 min	60 min
Intensity Fraction	0.41 ± 0.01	0.43 ± 0.00	0.44 ± 0.01
Cell Fraction	0.33 ± 0.03 *	0.43 ± 0.03 *	0.10 ± 0.00

Intensity and cell fraction measurements for secondary GPP130 peaks are reported for 0, 20, and 60 minutes following monensin washout. Secondary peaks for GPP130 were analyzed for intensity fraction with respect to the primary GPP130 peak and for the fraction of total cells analyzed (n=30) displaying a secondary peak. The intensity fractions reported are only for cells displaying secondary GPP130 peaks. Intensity and cell fraction results represented are mean ± SEM (n=2 independent experiments).

* Indicates significant difference between 60 minute cell fraction measurement as determined from Student t-test ($p < 0.05$).

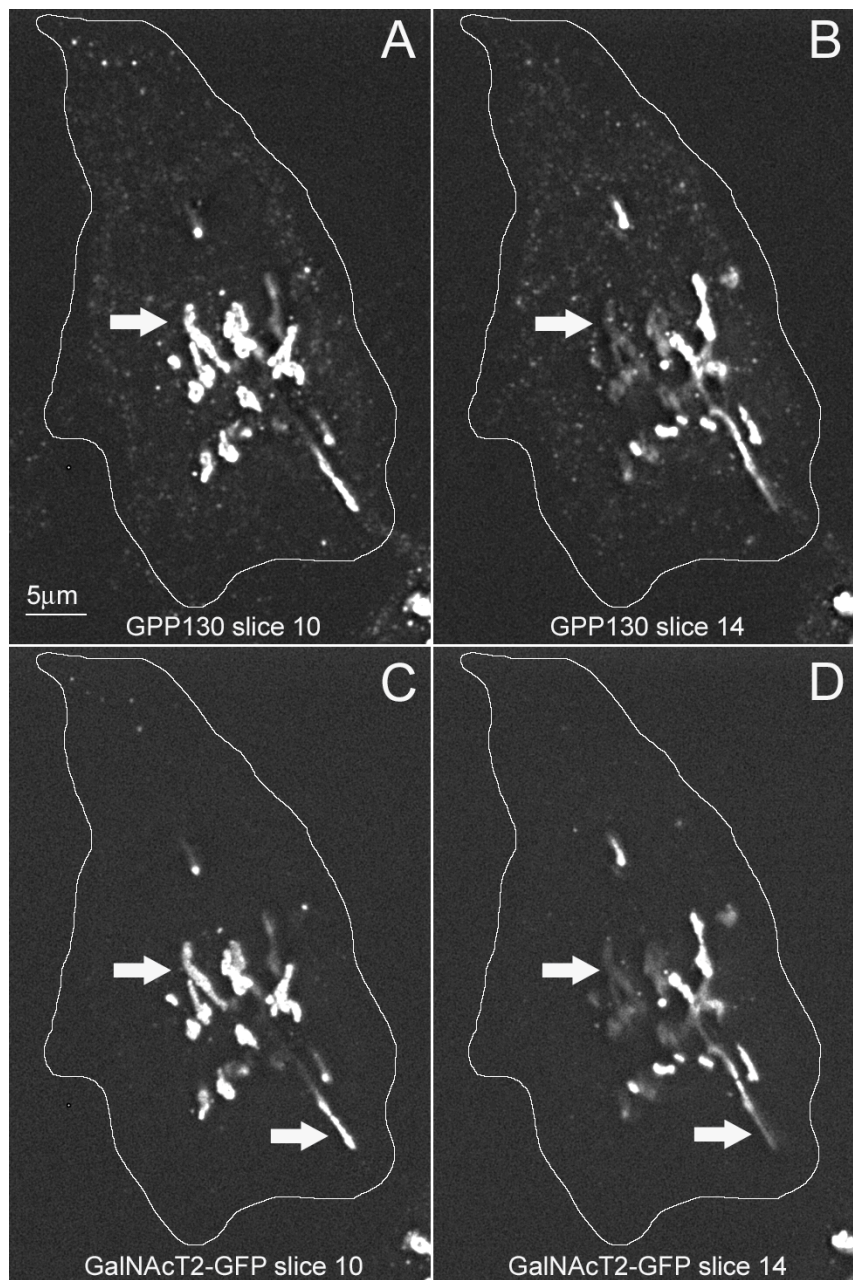


Figure 1. Presence of light spread from adjacent focal planes can interfere with colocalization analysis. Image stacks for GPP130 (A, B) and GalNAcT2-GFP (C, D) were acquired using spinning disk confocal microscopy and deconvolution. Two slices from a single confocal stack are shown for both channels. Even after deconvolution, there appears to be light interference from adjacent planes, as indicated at the arrows in the above figure. The images are shown under saturated grayscale levels so that light spread is more apparent.

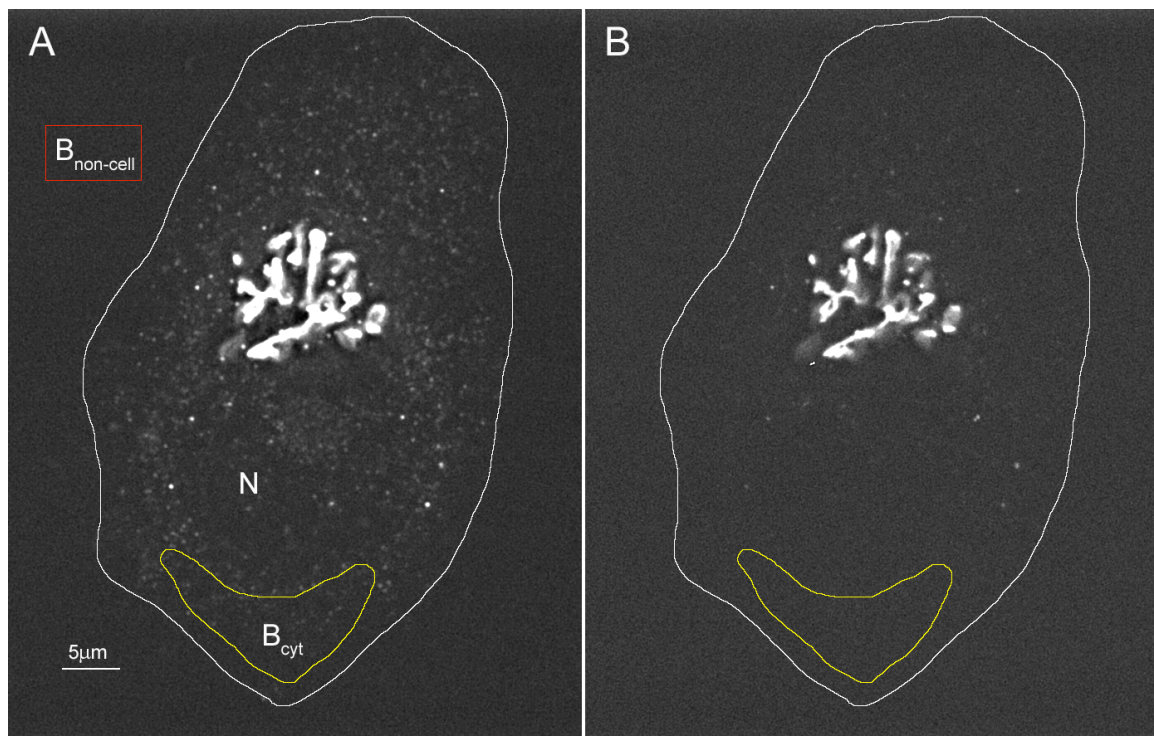


Figure 2. GalNAcT2-GFP cell stained with GPP130. The average background cytoplasmic intensity (B_{cyt} , yellow outline) and non-cell intensity background ($B_{\text{non-cell}}$, red outline) were measured for the GPP130 (A) images. The average background cytoplasmic intensity was also measured for the corresponding GalNAcT2-GFP confocal stack images (B). Cell is outlined in white for both images. The images are shown in extended focus format with best quality composite focus.

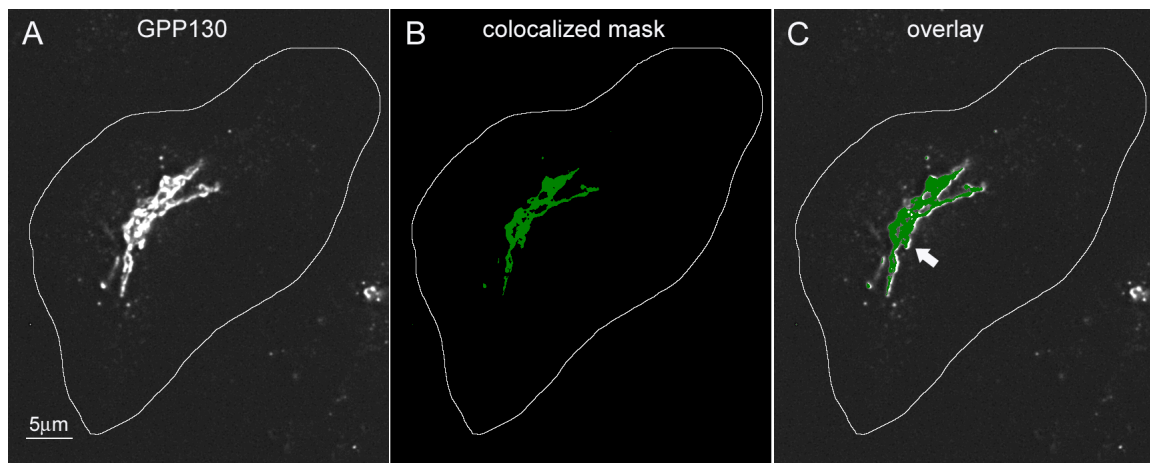


Figure 3. Colocalization Mask used to Identify Golgi GPP130 signal. The colocalization mask generated by IPLab (B) was used to identify colocalized regions in the original GPP130 image (A). The pixel intensities and areas coinciding with the colocalization mask (C) were measured for each slice of an image stack. Pixel shift causes a small shift of the mask (C, arrow), which was accounted for during the analysis as described in the Materials and Methods section. The images shown are a single slice from an acquired confocal stack.

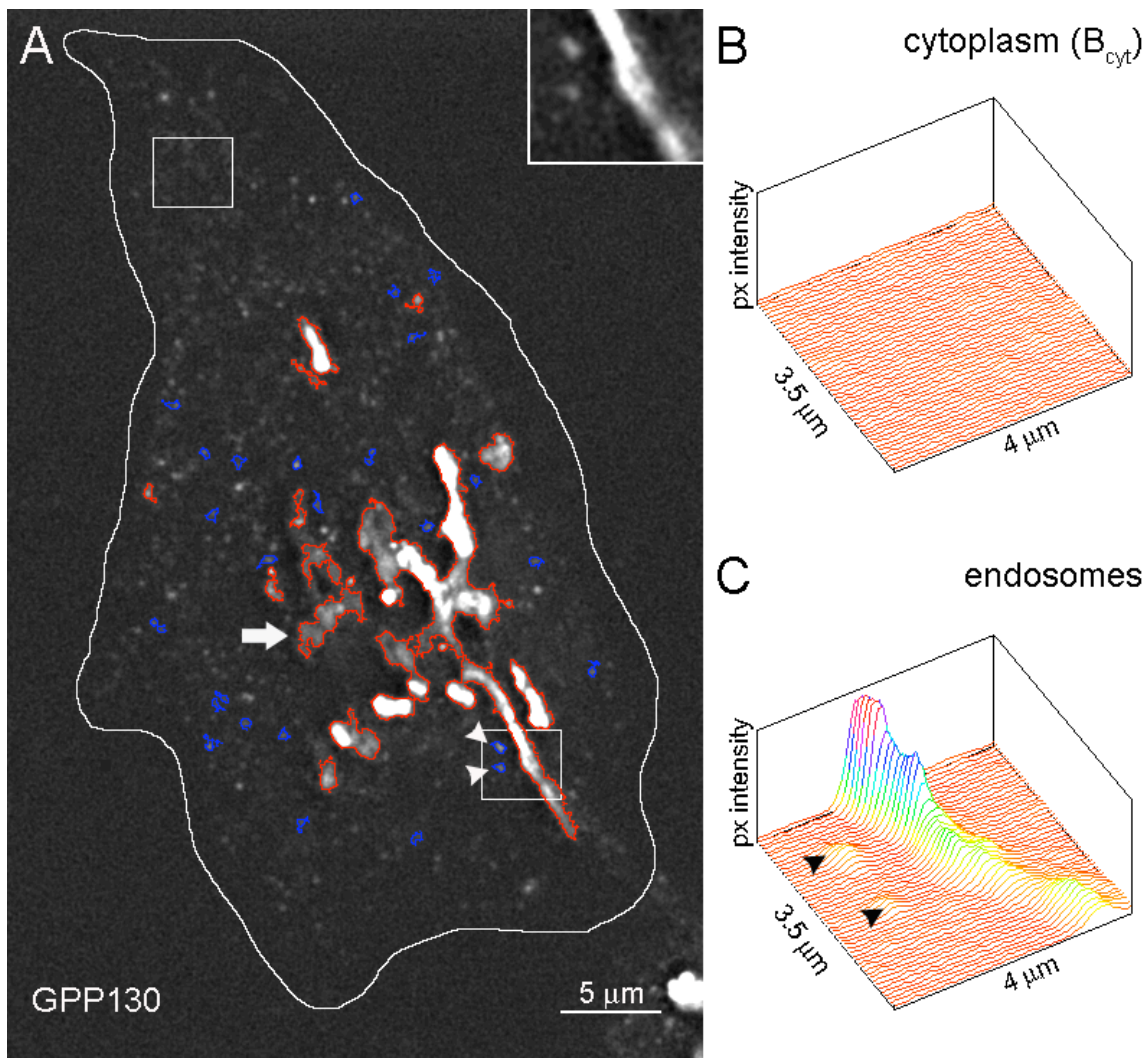


Figure 4. GPP130 Endosomal Staining is Distinguishable from Cytoplasm and Golgi

Staining. GalNAcT2-GFP cells stained for GPP130 (A, cell is outlined in white) were analyzed using size and intensity thresholds in order to distinguish GPP130 positive endosomal structures (A, blue outline) from the cytoplasmic background and measure the total GPP130 in the endosomes and Golgi (A, red outline). The endosomes (A arrowhead and inset) are distinguishable from the general cytoplasmic signal as small regularly shaped regions positive for GPP130 staining. The constant low-level signal characteristic of the cytoplasm is also apparent in a surface plot (B) of the region. Endosome and Golgi regions of GPP130 staining are distinguishable from the cytoplasmic staining as smaller low intensity peaks (C, arrowheads) and high intensity peaks/ridges, respectively. The images shown are for a single slice of a cell stained for GPP130 and acquired as a confocal stack.

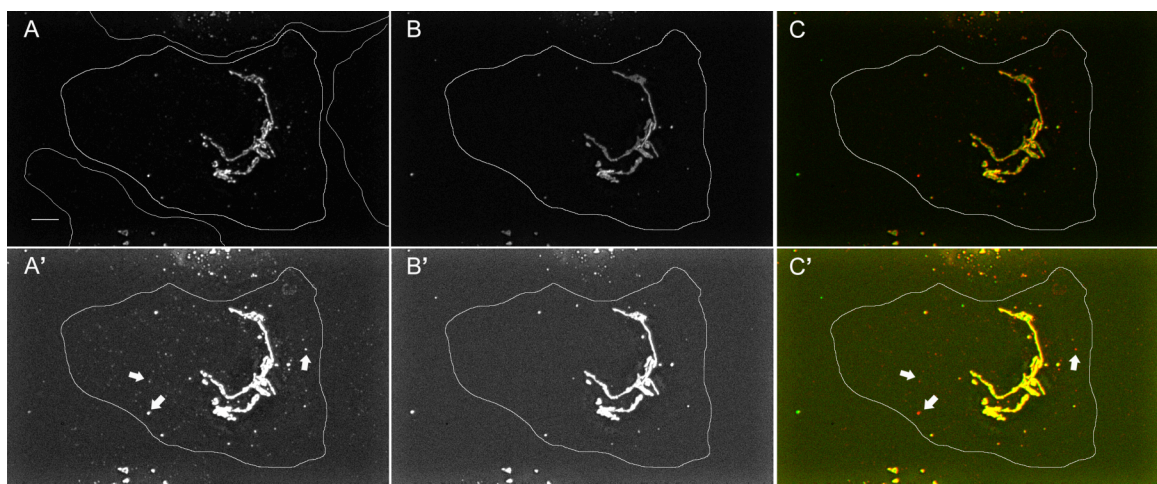


Figure 5. Small GPP130 fraction is found in endosomes at steady-state by confocal fluorescent microscopy. HeLa cells stably expressing GalNacT2-GFP were fixed and stained for GPP130 (A, A'). Fluorescent GalNacT2-GFP (B, B') was detected within the same cells and merged images of both proteins are shown (C, C'). Identical images are shown at normal (A-C, linear mapping of 100-4000 grayscale levels) and high (A'-C', 100-1000 grayscale levels) brightness. Image stacks were acquired using spinning disk confocal microscopy and are compressed into a single plane by composite extended focus. Note that small vesicles of the typical size of endosomes can be seen under high brightness (arrows, A', C'). Bar, 5 μ m.

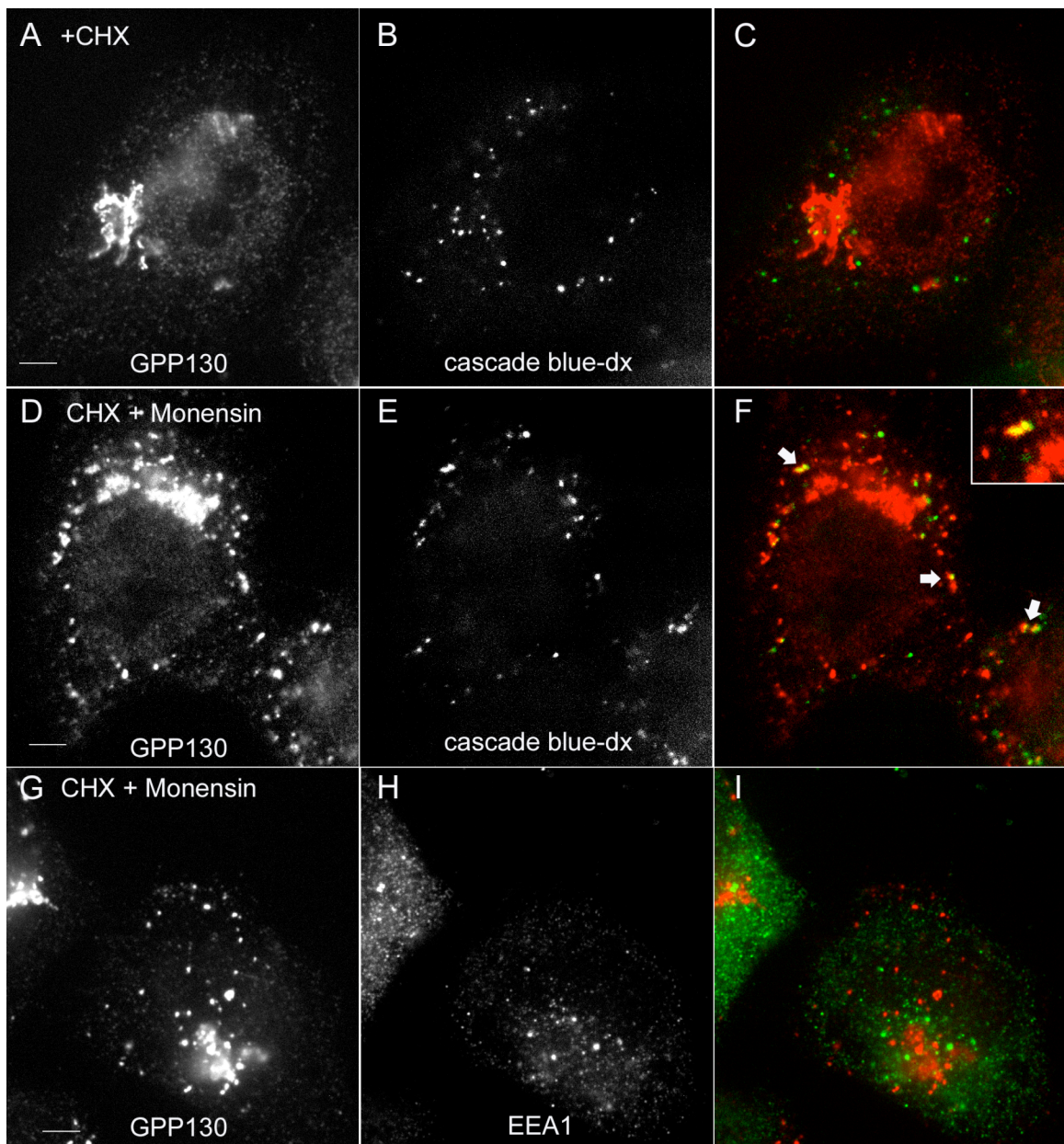


Figure 6. Colocalization of redistributed GPP130 with Cascade blue-dextran, but not with another endosomal marker EEA1. HeLa cells were fixed and stained for GPP130 (A,D) after 40 min incubation with Cascade blue dextran (B,E) both with (A-C) and without (D-F) monensin treatment for 60 min. The dextran was added 10 minutes into the monensin incubation. Merged images (C,F) show the colocalization of redistributed GPP130 and internalized dextran in endosomal like-structures (F inset). Cells were stained for GPP130 (G) and early endosomal marker EEA1 (H) both in the presence of monensin (G-I) and without (data not shown). The image stacks were acquired using spinning disk confocal and are shown in extended focus format with best quality composite focus settings. Bar, 5 μ m.

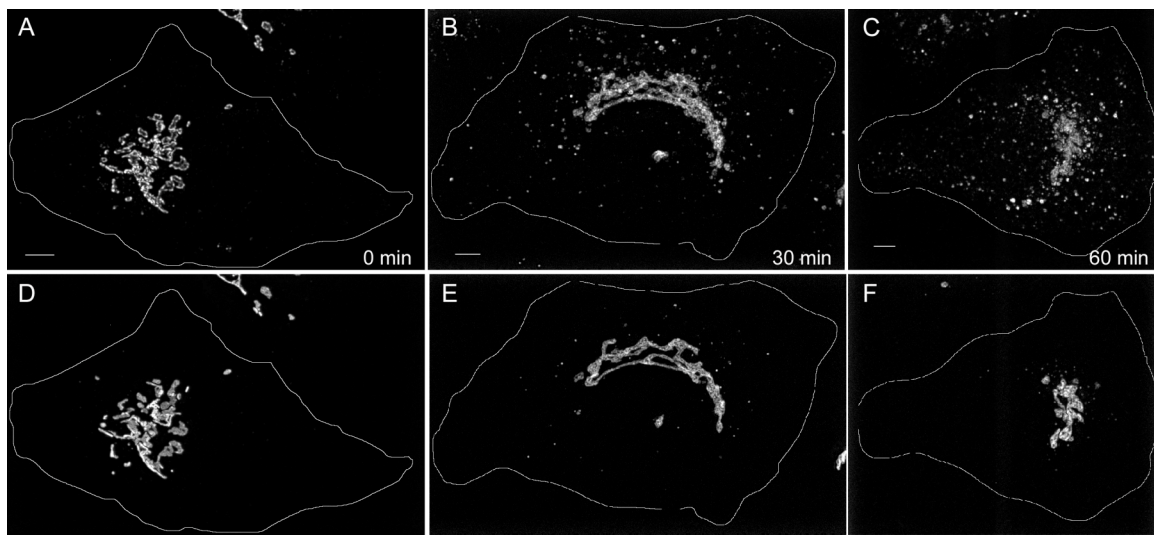


Figure 7. Monensin treatment induces GPP130 redistribution to endosomes. HeLa cells stably expressing GalNAcT2-GFP were fixed and stained for GPP130 at 0 min (A), 30 min (B), and 60 min (C) following monensin treatment. Corresponding images of GalNAcT2-GFP (D-F) are also shown. Images were acquired using spinning disk confocal microscopy and are shown in an extended focus format with best quality composite focus settings. Bar, 5 μ m.

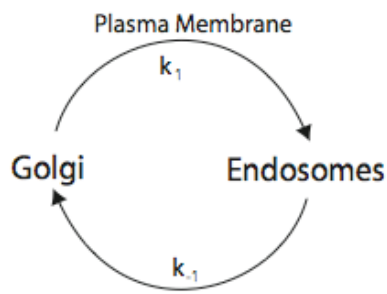


Figure 8. Schematic diagram of GPP130 Intracellular Transport Model. The Golgi and endosomes are considered as two separate compartments connected by first order processes. The rate constants k_1 and k_{-1} describe transport of GPP130 to and from the endosomes, respectively. Note that although transport through the plasma membrane in route to the endosomes likely occurs, it is not included within the model as levels were below detection limits.

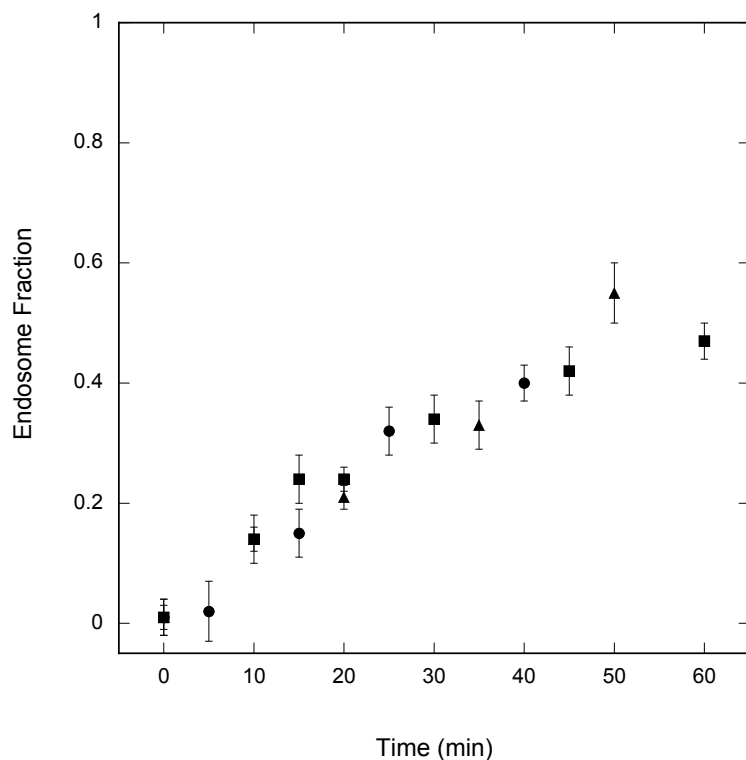


Figure 9. Quantification of GPP130 in endosomes following monensin treatment. HeLa cells stably expressing GalNAcT2-GFP were analyzed for GPP130 distribution following monensin treatment as described in materials and methods. Endosomal fractions from three independent experiments (●, ▲, ■) determined as a function of time following monensin treatments are shown. Symbols represent mean \pm SEM, $n \geq 10$.

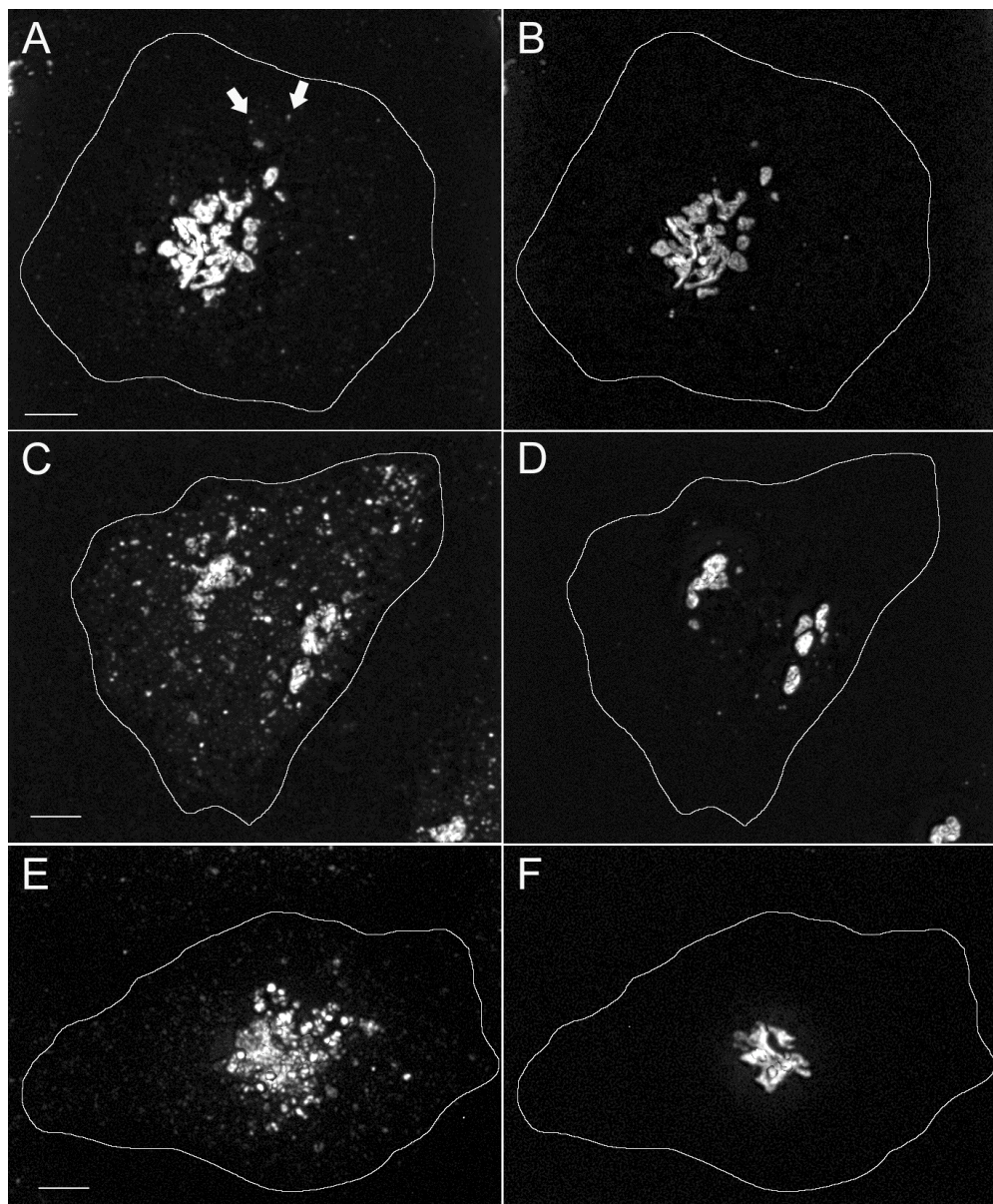


Figure 10. Extended monensin treatment results in accumulation of GPP130 in perinuclear endosomal populations. HeLa cells stably expressing GalNacT2-GFP were fixed and stained for GPP130 at 10 min (A), 30 min (C), and 2 hours (E) following monensin treatment. Corresponding images of GalNAcT2-GFP (B,D,F) are also shown. GPP130 begins to appear in endosomal structures as early as 10 minutes (A arrows). The clustering of endosomes in the Golgi region at 2 hour monensin treatment (E) makes it difficult to distinguish the two populations compared to the peripheral distribution of GPP130 positive endosomes at earlier time points (C). Image stacks were acquired using spinning disk confocal microscopy and are shown in an extended focus format with best quality composite focus settings. Bar, 5 μ m.

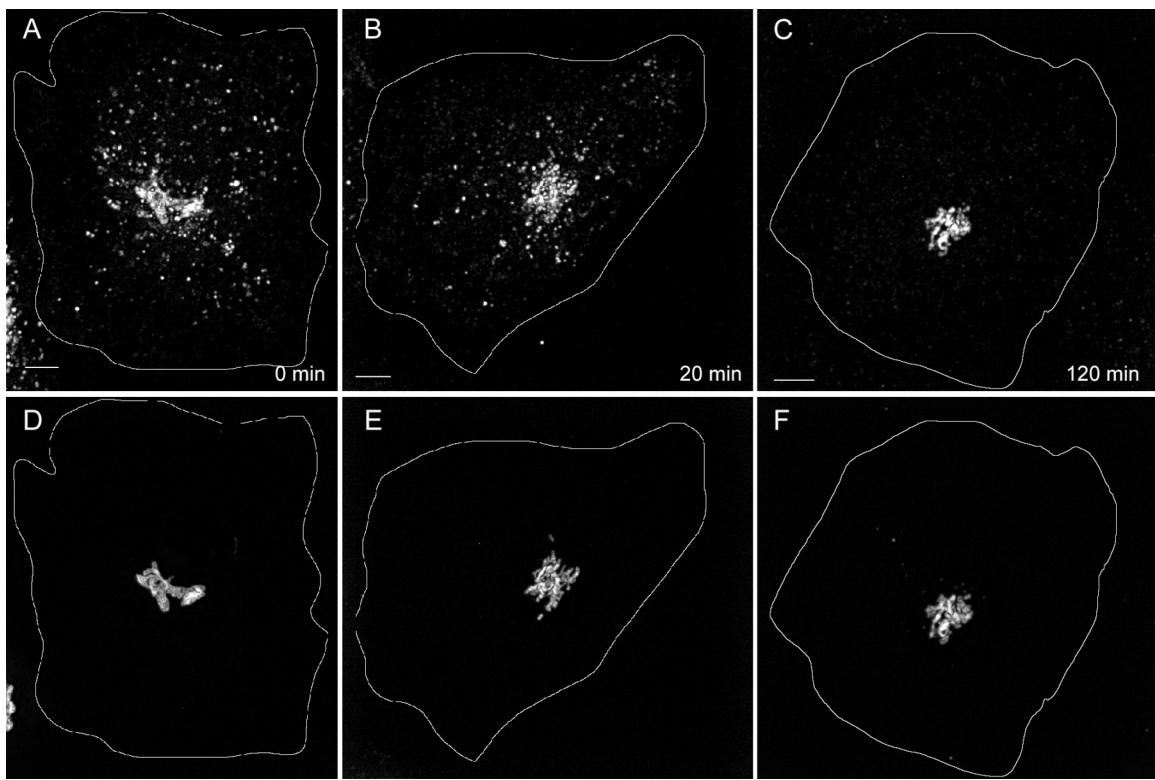


Figure 11. GPP130 returns to the Golgi apparatus following monensin washout. HeLa cells stably expressing GalNAcT2-GFP were treated with monensin for 60 min and then fixed and stained for GPP130 at 0 min (A), 20 min (B), and 120 min (C) following monensin washout. Corresponding images of GalNAcT2-GFP (D-F) are also shown. Image stacks were acquired using spinning disk confocal microscopy and are shown in an extended focus format using best quality composite focus settings. Bar, 5 μ m.

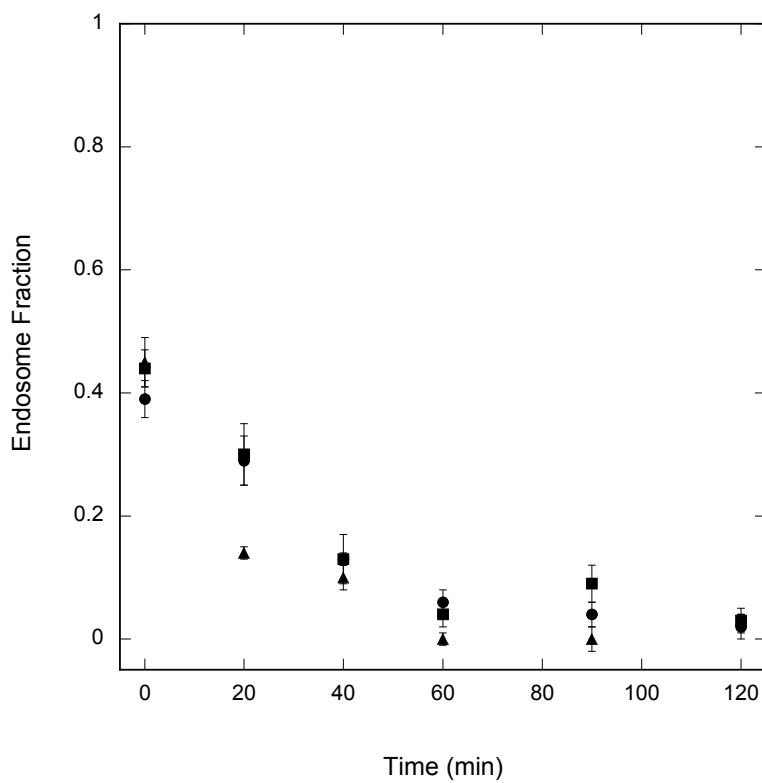


Figure 12. Quantification of GPP130 in endosomes following monensin washout. HeLa cells stably expressing GalNAcT2-GFP were analyzed for GPP130 distribution following monensin treatment for 60 min and subsequent washout as described in materials and methods. Endosomal fractions from three independent experiments (●, ▲, ■) were determined as a function of time following monensin washout are shown. Symbols represent mean \pm SEM, $n \geq 10$.

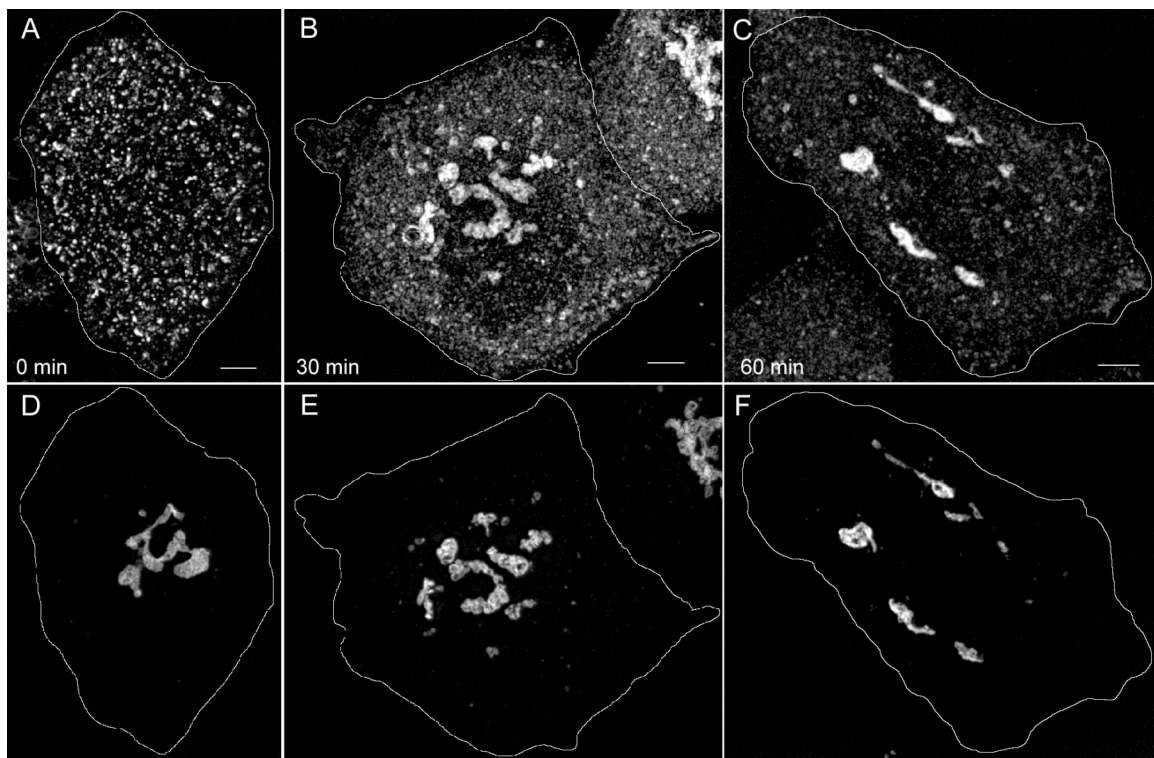


Figure 13. Shiga toxin B-fragment travels to the Golgi apparatus. HeLa cells stably expressing GalNAcT2-GFP were incubated with Cy3-conjugated Shiga toxin B-fragment for 60 min at 19.5°C and then fixed at 0 min (A), 30 min (B), and 120 min (C) following temperature increase to 37°C. Corresponding images of GalNAcT2-GFP (D-F) are also shown. Images were acquired using spinning disk confocal microscopy and are shown in an extended focus format using best quality composite focus settings. Bar, 5 μ m.

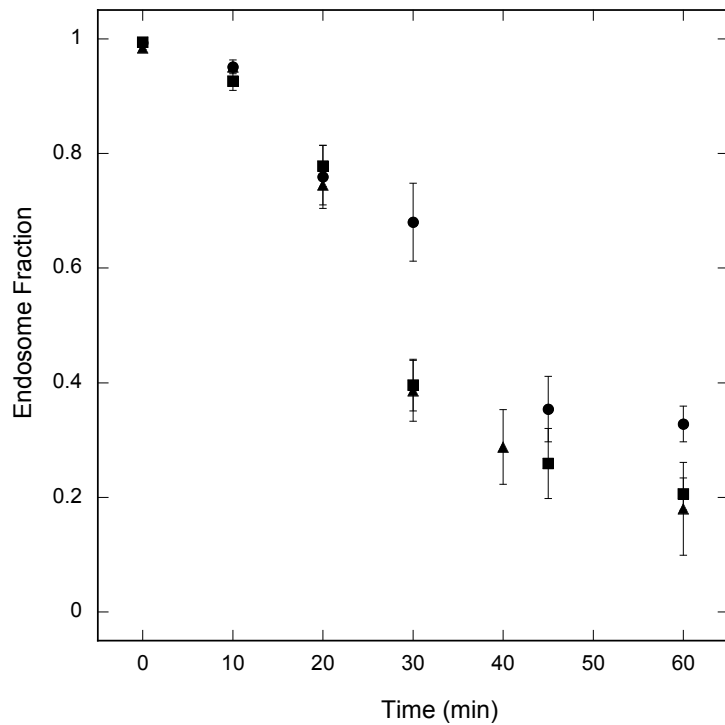


Figure 14. Quantification of Shiga toxin B-fragment in endosomes following 19.5°C temperature block. HeLa cells stably expressing GalNAcT2-GFP were analyzed for Shiga toxin distribution following 19.5°C temperature block for 60 min in the presence of monensin and subsequent temperature increase, as described in materials and methods. Endosomal fractions from three independent experiments (●, ▲, ■) were determined as a function of time following temperature increase to 37°C are shown. Symbols represent mean \pm SEM, $n \geq 10$.

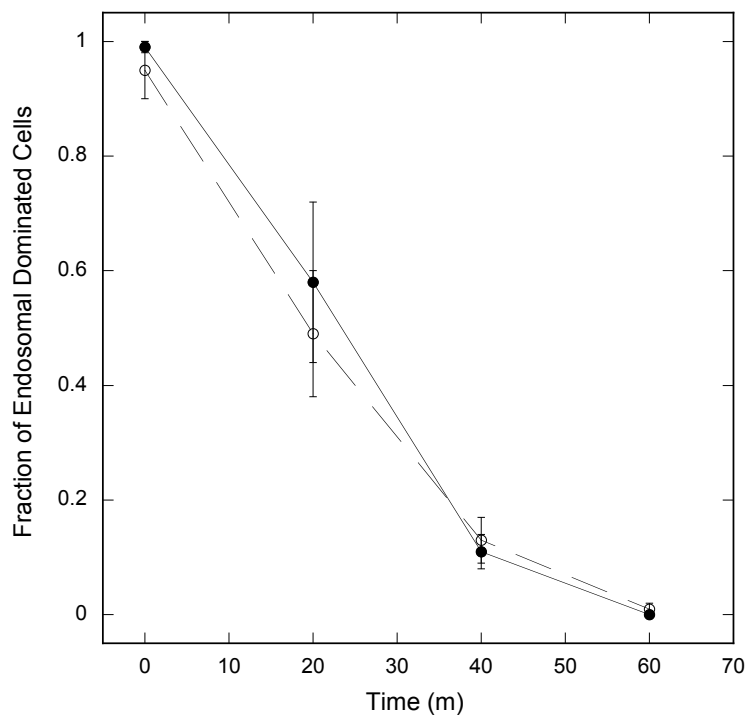


Figure 15. Widefield analysis of Shiga toxin B-fragment in endosomes with and without monensin treatment. HeLa cells stably expressing GalNAcT2-GFP were analyzed for endosomal Shiga toxin distribution following 19.5°C temperature block for 60 min with and without monensin treatment and subsequent temperature increase, as described in materials and methods. The fraction of cells exhibiting a predominantly endosome distribution of Shiga toxin were determined as a function of time following temperature increase to 37°C for three independent experiments with (●) and without (○) monensin treatment. Symbols represent mean \pm SEM, n > 36.

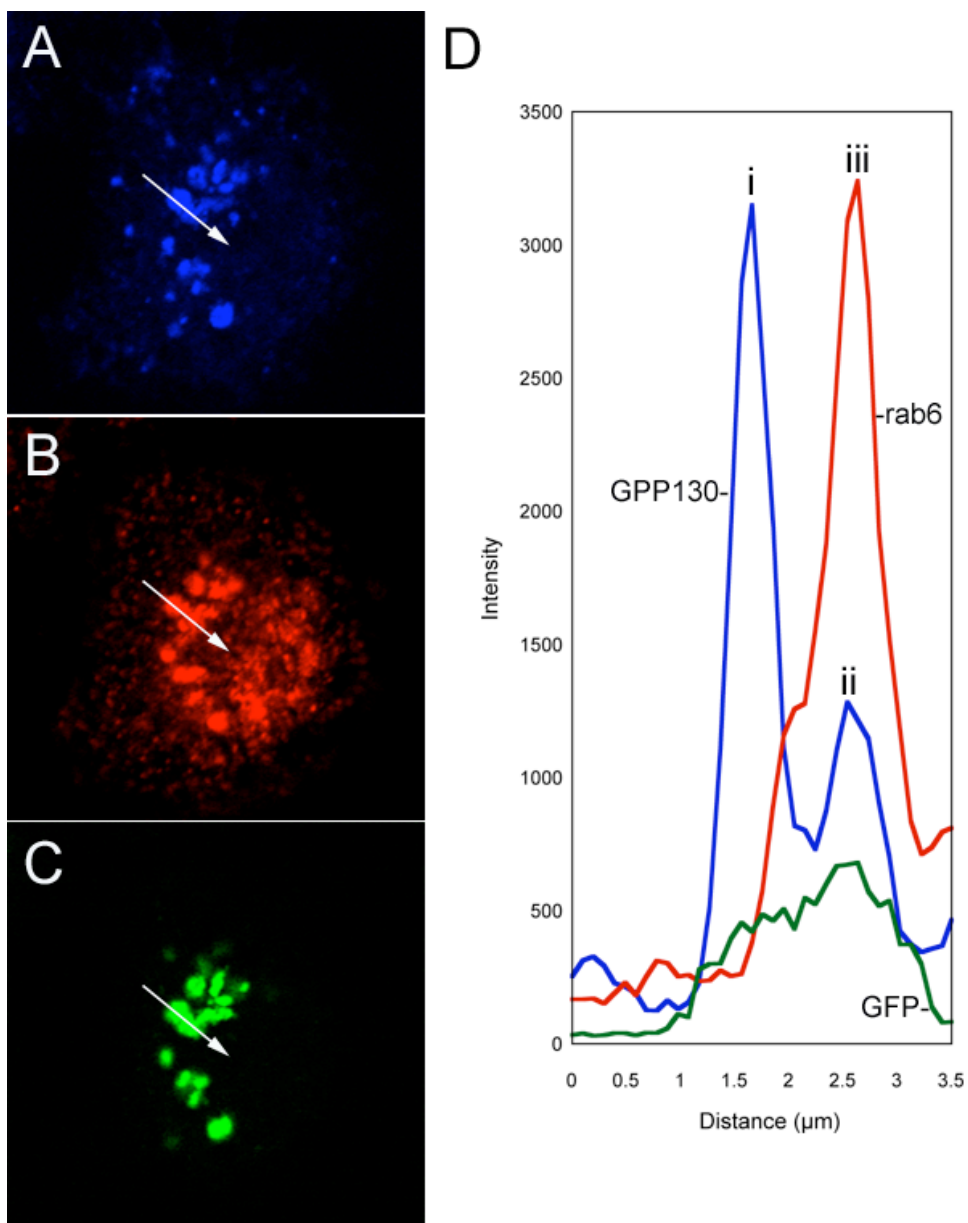


Figure 16. Distance Measurements for rab6 and GPP130 from LSM single-plane images.

LSM images of GalNAcT2-GFP cells at 20 minutes following monensin washout were analyzed for cis Golgi protein GPP130 (A), trans Golgi marker rab6 (B), and GalNAcT2-GFP (C) distances between peak intensities along a line drawn perpendicular to the Golgi (A, B, C arrows). Intensity versus distance was plotted along this line for each of the proteins (D, GPP130=blue, rab6=red, GalNAcT2-GFP=green). Distances between rab6 (D iii) and the primary GPP130 (D i) and secondary GPP130 (D ii) peaks were measured. GalNAcT2-GFP is distributed throughout the Golgi.

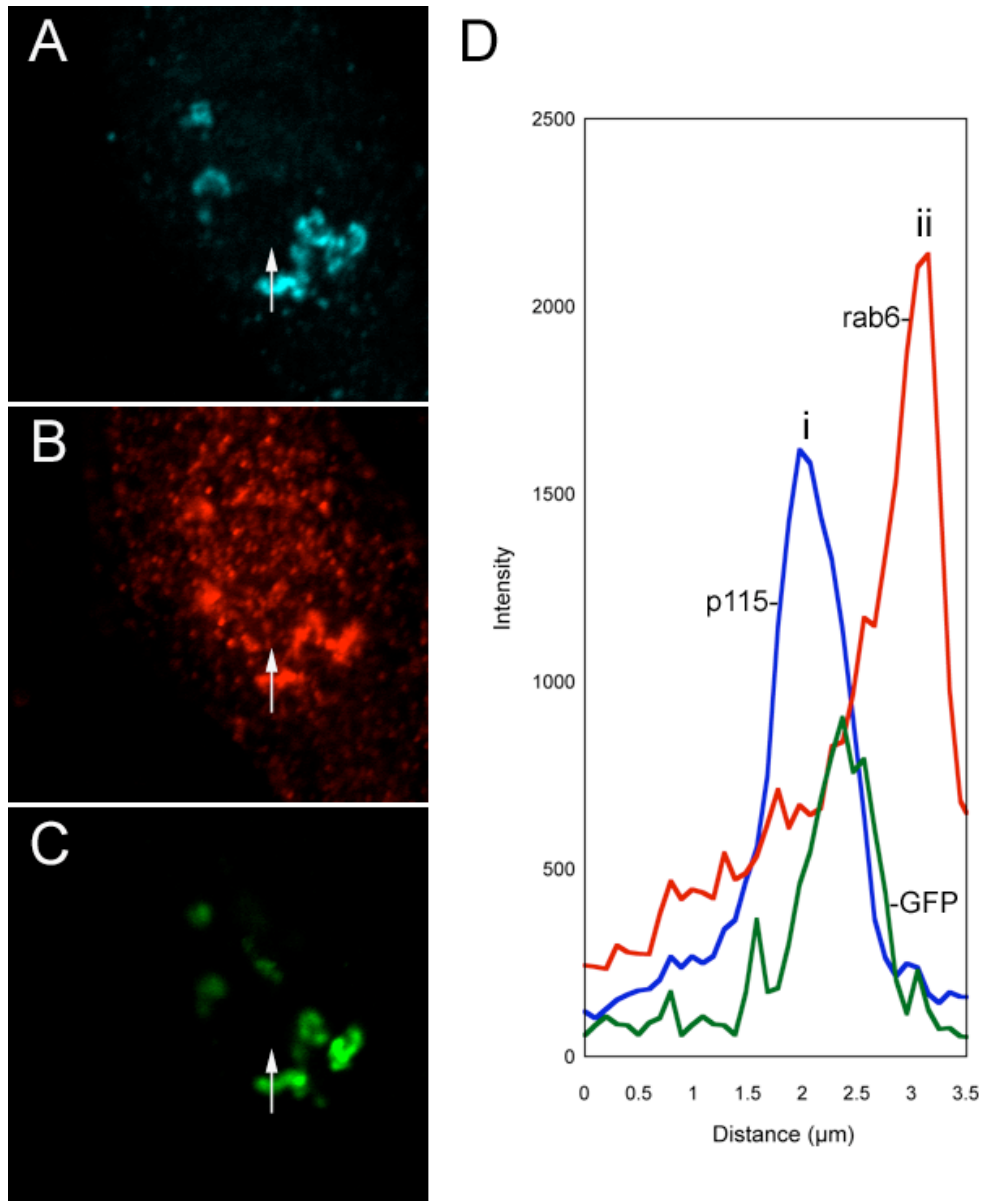


Figure 17. Distance Measurements for rab6 and p115 from LSM single-plane images. LSM images of GalNAcT2-GFP cells at 20 minutes following monensin washout were analyzed for cis Golgi marker p115 (A), trans Golgi marker rab6 (B), and GalNAcT2-GFP (C) distances between peak intensities along a line drawn perpendicular to the Golgi (A, B, C arrows). Intensity versus distance was plotted along this line for each of the proteins (D, p115=blue, rab6=red, GalNAcT2-GFP=green). Distances between rab6 (D ii) and p115 (D i) peaks were measured. GalNAcT2-GFP is distributed throughout the Golgi.

CHAPTER 5 – Conclusions and Future Directions

Research in cellular biology is extremely important to the advancement of our general knowledge about physiology and has many applications including the pharmaceutical industry, medicine, and agriculture. The combination of biology and engineering disciplines has furthered our understanding of basic biological processes and contributed to the advancement and discovery of new information.

5.1 SUMMARY OF RESEARCH

In this dissertation work, two important studies were undertaken. The first focused on developing a method for quantifying the distribution of proteins between the Golgi apparatus and endoplasmic reticulum (ER) using fluorescent microscopy with either antibody detection of endogenous and overexpressed proteins or live-fluorescently tagged overexpression systems (Chapter 3). This method resolved previous controversy in the literature as to the true steady-state distribution of Golgi resident proteins residing in the ER and determined the kinetic transport rates of these proteins by applying a mathematical model to our microscopy data. One important advancement of this work was in examining image data as data arrays and using surface plots to look for important but subtle differences in intensity.

This dissertation also presents work (Chapter 4) detailing the cycling kinetics of Golgi resident protein GPP130 through the late endosome bypass pathway. Using quantitative confocal stack analysis of monensin treated cells and kinetic modeling, the transport rates of GPP130 between the Golgi and endosomes were determined. A discrepancy between the transport rates and the steady-state distribution value led us to validate the endosomal to Golgi measurement using temperature blocked endosomal Shiga toxin B-fragment, a protein known to transport to the Golgi from endosomes (Sandvig and van Deurs, 2002). Excellent agreement with that measured for GPP130 was found. Additionally, the spatial distribution of GPP130 was investigated upon its return to the Golgi following endosomal exit as a first step in spatially characterizing this novel cycling pathway.

5.2 FUTURE STUDIES

Based on the results presented in Chapters 3 and 4, a number of studies come to mind. Several experimental lines based on the previous experiments presented in this dissertation could be used

to further our understanding of protein distribution and trafficking in the secretory and biosynthetic pathways.

As described in Chapter 4, we saw that the pH disrupting drug monensin caused the reversible redistribution of Golgi protein GPP130 to the endosomes. GPP130 transport along this pathway could be investigated in the presence of a different pH disrupting drug, namely bafilomycin. In the presence of bafilomycin, the lumen of intracellular organelles is neutralized, similar to monensin. This neutralization is achieved through the inhibition of vacuolar ATPases responsible for the transport of protons across the membrane (Moriyama and Nelson, 1989). Bafilomycin induced redistribution is unlikely to affect the trafficking of GPP130 to the endosomes in a different manner than monensin. Previous work has shown that bafilomycin does cause accumulation of GPP130 in the endosomes in a manner similar to monensin as evidenced by co-staining with TGN38 protein (Puri et al., 2002) and the uptake of both anti-GPP130 and anti-TGN38 antibodies in the presence of the drug (Puri et al., 2002; Puthenveedu et al., 2003). Rate measurements for transport of GPP130 to the endosomes in the presence of bafilomycin could be compared with the results presented in Chapter 4, although a significant difference is not expected.

As presented in Chapter 4, the transport of Shiga toxin B-fragment to the Golgi was characterized following accumulation in the endosomes as an alternative way to determine the endosome to Golgi trafficking rate constant. The effect of this accumulation in the endosomes and possible saturation of regulatory factors on the exit of protein from the endosomes could be studied by analyzing the rate of transport to the Golgi versus concentration of exogenously added Shiga toxin. If the rate constant measured proved to be dependant on the concentration of toxin fragment in solution, it could be suggested that the model developed in Chapter 4 is incomplete and that a limiting factor involved in exit from the endosomes may exist. An alternative study that would avoid the accumulation of protein in the endosomes altogether involves measuring the rate of transport of Cy3-conjugated Shiga toxin fragment in real time as it travels from the plasma membrane to the Golgi. Using an environmental chamber to control temperature and CO₂-independent DMEM media, Shiga toxin fragment trafficking to the Golgi could be measured, provided the system is sensitive enough to track small portions of the endocytosed toxin. This would allow a single cell to be studied at each time point during the redistribution and could be done without the accumulation of toxin fragment in the endosomes prior to analysis.

The Linstedt laboratory has shown that GPP130 redistributes to ER like structures colocalizing with other integral Golgi membrane proteins during brefeldin A (Linstedt et al., 1997) and nocodazole treatments (Linstedt et al., 1997; Puri et al., 2002). It has not been conclusively shown that GPP130 normally recycles into the ER. Verification that GPP130 cycles to the ER and characterization of the kinetics of this transport would be an extension of the work done in both Chapters 3 and 4. Microinjection has been used to block the exit of protein from the ER. Sar1p GDP-restricted protein prevents COPII coat protein recruitment thereby blocking GPP130 exit from the ER. Using an ER exit block, it should be possible to verify a cycling pathway to the ER and to study the redistribution of GPP130 along this pathway versus time. Following microinjection, depletion of GPP130 signal from the Golgi could be quantified using the techniques presented in Chapter 3 and used to determine the rate constant for transport of GPP130 from the Golgi to the ER. Once the presence of GPP130 recycling through the ER is verified and the retrograde (Golgi to ER) rate determined, brefeldin A washout experiments could be used to measure the anterograde transport (ER to Golgi) of GPP130 returning to the cis Golgi. These experiments would also add an additional compartment to the model used in our analysis for cycling of GPP130. A revised three-compartment model along with the measured anterograde and retrograde transport rate constants for trafficking to the ER and endosomes could be used to predict the complete cycling kinetics of GPP130 in both the secretory and biosynthetic pathways. These experiments would help illuminate the dominant cycling pathway and possibly help illuminate the primary function of the GPP130 protein.

Analysis of GP73, another cis localized Golgi protein structurally related to GPP130 (Puri et al., 2002), redistribution upon pH disruption is an alternative method for studying the trafficking of proteins from the Golgi to the endosomes. GP73 has been shown to transport to the endosomes and return to the Golgi along the late endosome bypass pathway, similar to GPP130. The retrograde transport of the protein has also been shown to be dependant on the presence of GPP130 for endosomal exit (Puri et al., 2002). The quantification of GP73 cis Golgi localized protein during monensin addition and subsequent washout could be compared to the GPP130 analysis presented in Chapter 4. Both proteins have pH sensitive targeting domains suggesting the mechanisms of transport to the endosomes are similar.

The spatial trafficking results presented in this dissertation were the product of a novel method of investigating spatial relationships of proteins between the individual cisternae, however the method requires some modifications. An interpretive problem was the presence of a large number

of secondary (trans localized) GPP130 peaks at the 0 minute washout. One possible explanation is that a small portion of GPP130 is leaking to the Golgi even in the presence of monensin when the exit from the endosomes is presumably blocked. Another, more likely possibility is that the trans peak is the result of GPP130 that has not left the TGN and is in the process of trafficking to the endosomes from the cis Golgi region. This could be verified by tracking the distance between GPP130 and the trans Golgi protein rab6 during monensin addition and subsequent GPP130 redistribution. If the trans peak is the result of GPP130 retained in the TGN, the intensity of protein in the peak should increase with time as GPP130 accumulates in the endosomes. Additionally, quantification of GPP130 in the trans Golgi region in the absence of monensin also needs to be investigated to confirm the small presence of the protein in the trans region at steady-state.

Pulse chase experiments could also be used to track the progress of GPP130 as it travels from the Golgi to the endosomes during monensin treatment. Radioactive methionine labeling of GPP130 and subsequent cell fractionation could be used to quantify the concentration of protein in the Golgi and the endosomes at various time points during monensin treatment. These experiments provide an alternative method for studying a small population of newly synthesized protein as it travels through the Golgi to the endosomes via the plasma membrane. These experiments would provide a method for determining the identity of the trans portion of GPP130 seen in the LSM experiments. If a trans peak of GPP130 is found in the presence of monensin, it can be suggested that the trans pool is a result of protein waiting to be transported to the endosomes. An increase in the concentration of protein in the trans region following monensin washout would indicate returning GPP130 protein while a decrease might suggest the resumption of steady-state cycling with the back up of GPP130 being transported out of the trans region.

As fluorescent microscopy technology improves, the ability of researchers to study individual protein dynamics will also improve as well as increase the knowledge of intracellular protein trafficking. Recent advances in the area of microscopy include the introduction of fluorescence resonance energy transfer (FRET), total internal reflection microscopy (TIRF), high-resolution 4Pi microscopy, and stimulated emission depletion microscopy (STED) (Presley, 2005). FRET microscopy (Jares-Erijman and Jovin, 2003; Stryer and Haugland, 1967) measures the interaction between two proteins in close proximity. These interactions are measured when an excited fluorophore from one protein transfers its energy to an adjacent fluorophore labeled protein and can be used to detect interactions *in vitro*, at the cell surface, or in the cell. FRET has already

been used to investigate the interactions between proteins involved in the formation of COP1 coated vesicles and could potentially prove useful in the understanding the relationship between GPP130 and transport vesicle associated proteins. TIRF microscopy is well suited for the study and visualization of protein kinetics at the plasma membrane. Light from the objective intersects the sample at an extremely shallow angle allowing only the region on or very near the cell-coverslip interface to be visualized. TIRF has a very high signal-to-noise ratio and has already been used to study the fusion of secretory granules and post Golgi-transport intermediates and to track single fluorescent molecules on or very near the cell surface (Koyama-Honda et al., 2005; Lang et al., 1997; Schmoranzer et al., 2000). It could facilitate the study of GPP130 cycling to the plasma membrane during monensin treatment. 4Pi fluorescent microscopy (Hell and Stelzer, 1992) is a high-resolution technique that uses a double objective lens to increase numerical aperture and axial resolution. STED (Klar et al., 2000) is another high-resolution technique that uses non-linear optics to achieve high resolution (nm scale) in both the axial and lateral directions. The resolution limitations of traditional light microscopy make the visualization of subcellular structures such as the Golgi difficult. The possibility to visualize the cell at a resolution of 50 nm or less would dramatically impact our understanding of the dynamics and structure of the Golgi. These advancements could provide the means for reliably distinguishing between the ER and Golgi (Chapter 3) and the Golgi and endosomes (Chapter 4) at the resolution of the organelles. The ability to measure protein-protein interactions could also provide a method for investigating the possibility of interactions between GPP130 and another protein necessary for transport to and from the Golgi. Finally, increased resolution could allow the distribution within the Golgi to be studied and distances between proteins localized to different cisternae more accurately measured.

5.3 CONCLUSIONS

In conclusion, the work presented in this dissertation has provided valuable information concerning the kinetic cycling properties of Golgi resident proteins in both the secretory and late endosomal bypass pathways. These results combined with the preliminary data regarding the spatial trafficking properties of GPP130 have contributed to the understanding of trafficking in the secretory pathway and the late endosomal bypass and ER recycling pathways in particular. The work presented in this dissertation contributes to the general knowledge of intracellular Golgi trafficking in both the biosynthetic and endocytic pathways and in a more general way, exemplifies the value of applying engineering analysis to biological cell studies and outlined important tools with applications to a wide array of cellular systems.

BIBLIOGRAPHY

- Andrieu, N., R. Salvayre, and T. Levade. 1996. Comparative study of the metabolic pools of sphingomyelin and phosphatidylcholine sensitive to tumor necrosis factor. *Eur J Biochem.* 236:738-45.
- Ang, A.L., T. Taguchi, S. Francis, H. Folsch, L.J. Murrells, M. Pypaert, G. Warren, and I. Mellman. 2004. Recycling endosomes can serve as intermediates during transport from the Golgi to the plasma membrane of MDCK cells. *J Cell Biol.* 167:531-43.
- Aten, J.A., J. Stap, P.M. Krawczyk, C.H. van Oven, R.A. Hoebe, J. Essers, and R. Kanaar. 2004. Dynamics of DNA double-strand breaks revealed by clustering of damaged chromosome domains. *Science.* 303:92-5.
- Axelrod, D. 1989. Total internal reflection fluorescence microscopy. *Methods Cell Biol.* 30:245-70.
- Axelsson, M.A., N.G. Karlsson, D.M. Steel, J. Ouwendijk, T. Nilsson, and G.C. Hansson. 2001. Neutralization of pH in the Golgi apparatus causes redistribution of glycosyltransferases and changes in the O-glycosylation of mucins. *Glycobiology.* 11:633-44.
- Axelsson, M.A., and G. Warren. 2004. Rapid, endoplasmic reticulum-independent diffusion of the mitotic Golgi haze. *Mol Biol Cell.* 15:1843-52.
- Bachert, C., T.H. Lee, and A.D. Linstedt. 2001. Luminal endosomal and Golgi-retrieval determinants involved in pH-sensitive targeting of an early Golgi protein. *Mol Biol Cell.* 12:3152-60.
- Balch, W.E., and D.S. Keller. 1986. ATP-coupled transport of vesicular stomatitis virus G protein. Functional boundaries of secretory compartments. *J Biol Chem.* 261:14690-6.
- Balch, W.E., J.M. McCaffery, H. Plutner, and M.G. Farquhar. 1994. Vesicular stomatitis virus glycoprotein is sorted and concentrated during export from the endoplasmic reticulum. *Cell.* 76:841-52.
- Barak, L.S., S.S. Ferguson, J. Zhang, C. Martenson, T. Meyer, and M.G. Caron. 1997. Internal trafficking and surface mobility of a functionally intact beta₂-adrenergic receptor-green fluorescent protein conjugate. *Mol Pharmacol.* 51:177-84.
- Baravalle, G., D. Schober, M. Huber, N. Bayer, R.F. Murphy, and R. Fuchs. 2005. Transferrin recycling and dextran transport to lysosomes is differentially affected by bafilomycin, nocodazole, and low temperature. *Cell Tissue Res.* 320:99-113.
- Barr, F.A. 2005. Purification and functional interactions of GRASP55 with Rab2. *Methods Enzymol.* 403:391-401.
- Barr, F.A., and B. Short. 2003. Golgins in the structure and dynamics of the Golgi apparatus. *Curr Opin Cell Biol.* 15:405-13.
- Becker, B., B. Bolinger, and M. Melkonian. 1995. Anterograde transport of algal scales through the Golgi complex is not mediated by vesicles. *Trends Cell Biol.* 5:305-7.
- Belichenko, P.V., A.A. Fedorov, and A.B. Dahlstrom. 1996. Quantitative analysis of immunofluorescence and lipofuscin distribution in human cortical areas by dual-channel confocal laser scanning microscopy. *J Neurosci Methods.* 69:155-61.
- Bergmann, J.E., K.T. Tokuyasu, and S.J. Singer. 1981. Passage of an integral membrane protein, the vesicular stomatitis virus glycoprotein, through the Golgi apparatus en route to the plasma membrane. *Proc Natl Acad Sci U S A.* 78:1746-50.
- Bevis, B.J., A.T. Hammond, C.A. Reinke, and B.S. Glick. 2002. De novo formation of transitional ER sites and Golgi structures in *Pichia pastoris*. *Nat Cell Biol.* 4:750-6.
- Bonifacino, J.S., and B.S. Glick. 2004. The mechanisms of vesicle budding and fusion. *Cell.* 116:153-66.
- Brismar, H., O. Trepte, and B. Ulvhake. 1995. Spectra and fluorescence lifetimes of lissamine rhodamine, tetramethylrhodamine isothiocyanate, Texas red, and cyanine 3.18

- fluorophores: influences of some environmental factors recorded with a confocal laser scanning microscope. *J Histochem Cytochem.* 43:699-707.
- Brown, R.M., Jr. 1969. Observations on the relationship of the golgi apparatus to wall formation in the marine chrysophycean alga Pleurochrysis scherffelii Pringsheim. *J Cell Biol.* 41:109-23.
- Carlton, J., M. Bujny, B.J. Peter, V.M. Oorschot, A. Rutherford, H. Mellor, J. Klumperman, H.T. McMahon, and P.J. Cullen. 2004. Sorting nexin-1 mediates tubular endosome-to-TGN transport through coincidence sensing of high-curvature membranes and 3-phosphoinositides. *Curr Biol.* 14:1791-800.
- Cartwright, T. 1994. Animal Cells as Bioreactors. Cambridge University Press, New York, New York.
- Chalfie, M., Y. Tu, G. Euskirchen, W.W. Ward, and D.C. Prasher. 1994. Green fluorescent protein as a marker for gene expression. *Science.* 263:802-5.
- Chapman, R.E., and S. Munro. 1994. Retrieval of TGN proteins from the cell surface requires endosomal acidification. *Embo J.* 13:2305-12.
- Charman, W., H. Chan, B. Finnin, and S. Charman. 1999. Drug Delivery: A Key Factor in Relising the Full Therapeutic Potential of Drugs. *Drug Development Research.* 46:316-327.
- Chen, M.X., A.E. McPartlin, L. Brown, Y.H. Chen, H.M. Barker, and P.T. Cohen. 1994. A novel human protein serine/threonine phosphatase, which possesses four tetratricopeptide repeat motifs and localizes to the nucleus. *Embo J.* 13:4278-90.
- Chow, A., D. Toomre, W. Garrett, and I. Mellman. 2002. Dendritic cell maturation triggers retrograde MHC class II transport from lysosomes to the plasma membrane. *Nature.* 418:988-94.
- Chu, L., and D.K. Robinson. 2001. Industrial choices for protein production by large-scale cell culture. *Curr Opin Biotechnol.* 12:180-7.
- Cole, N.B., N. Sciaky, A. Marotta, J. Song, and J. Lippincott-Schwartz. 1996. Golgi dispersal during microtubule disruption: regeneration of Golgi stacks at peripheral endoplasmic reticulum exit sites. *Mol Biol Cell.* 7:631-50.
- Cubitt, A.B., R. Heim, S.R. Adams, A.E. Boyd, L.A. Gross, and R.Y. Tsien. 1995. Understanding, improving and using green fluorescent proteins. *Trends Biochem Sci.* 20:448-55.
- Davidson MW, A.M. Optical Microscopy.
- De Giorgi, F., M. Brini, C. Bastianutto, R. Marsault, M. Montero, P. Pizzo, R. Rossi, and R. Rizzuto. 1996. Targeting aequorin and green fluorescent protein to intracellular organelles. *Gene.* 173:113-7.
- Dinter, A., and E.G. Berger. 1998. Golgi-disturbing agents. *Histochem Cell Biol.* 109:571-90.
- Doms, R.W., G. Russ, and J.W. Yewdell. 1989. Brefeldin A redistributes resident and itinerant Golgi proteins to the endoplasmic reticulum. *J Cell Biol.* 109:61-72.
- Dunphy, W.G., R. Brands, and J.E. Rothman. 1985. Attachment of terminal N-acetylglucosamine to asparagine-linked oligosaccharides occurs in central cisternae of the Golgi stack. *Cell.* 40:463-72.
- Egner, A., S. Verrier, A. Goroshkov, H.D. Soling, and S.W. Hell. 2004. 4Pi-microscopy of the Golgi apparatus in live mammalian cells. *J Struct Biol.* 147:70-6.
- Ehrhardt, D. 2003. GFP technology for live cell imaging. *Curr Opin Plant Biol.* 6:622-8.
- Elsner, M., H. Hashimoto, J.C. Simpson, D. Cassel, T. Nilsson, and M. Weiss. 2003. Spatiotemporal dynamics of the COPI vesicle machinery. *EMBO Rep.* 4:1000-4.
- Engstler, M., L. Thilo, F. Weise, C.G. Grunfelder, H. Schwarz, M. Boshart, and P. Overath. 2004. Kinetics of endocytosis and recycling of the GPI-anchored variant surface glycoprotein in Trypanosoma brucei. *J Cell Sci.* 117:1105-15.

- Erdogan, T. 2005. Achieving the Best Alignment for Fluorescent Images. In *Biophotonics International*. L. Publications, editor. Semrock.
- Farmaki, T., S. Ponnambalam, A.R. Prescott, H. Clausen, B.L. Tang, W. Hong, and J.M. Lucocq. 1999. Forward and retrograde trafficking in mitotic animal cells. ER-Golgi transport arrest restricts protein export from the ER into COPII-coated structures. *J Cell Sci.* 112 (Pt 5):589-600.
- Farquhar, M.G., and G.E. Palade. 1998. The Golgi apparatus: 100 years of progress and controversy. *Trends Cell Biol.* 8:2-10.
- Fleischer, B., S. Fleischer, and H. Ozawa. 1969. Isolation and characterization of Golgi membranes from bovine liver. *J Cell Biol.* 43:59-79.
- Furukawa, S., N. Sakata, H.N. Ginsberg, and J.L. Dixon. 1992. Studies of the sites of intracellular degradation of apolipoprotein B in Hep G2 cells. *J Biol Chem.* 267:22630-8.
- Futter, C.E., C.N. Connolly, D.F. Cutler, and C.R. Hopkins. 1995. Newly synthesized transferrin receptors can be detected in the endosome before they appear on the cell surface. *J Biol Chem.* 270:10999-1003.
- Garcia-Mata, R., T. Szul, C. Alvarez, and E. Sztul. 2003. ADP-ribosylation factor/COPI-dependent events at the endoplasmic reticulum-Golgi interface are regulated by the guanine nucleotide exchange factor GBF1. *Mol Biol Cell.* 14:2250-61.
- Girod, A., B. Storrie, J.C. Simpson, L. Johannes, B. Goud, L.M. Roberts, J.M. Lord, T. Nilsson, and R. Pepperkok. 1999. Evidence for a COP-I-independent transport route from the Golgi complex to the endoplasmic reticulum. *Nat Cell Biol.* 1:423-30.
- Girotti, M., and G. Banting. 1996. TGN38-green fluorescent protein hybrid proteins expressed in stably transfected eukaryotic cells provide a tool for the real-time, *in vivo* study of membrane traffic pathways and suggest a possible role for ratTGN38. *J Cell Sci.* 109 (Pt 12):2915-26.
- Glick, B.S., and V. Malhotra. 1998. The curious status of the Golgi apparatus. *Cell.* 95:883-9.
- Green, S.A., and R.B. Kelly. 1992. Low density lipoprotein receptor and cation-independent mannose 6-phosphate receptor are transported from the cell surface to the Golgi apparatus at equal rates in PC12 cells. *J Cell Biol.* 117:47-55.
- Griffiths, G. 1993. Fine structure immunocytochemistry. Springer-Verlag, Berlin. pp. 375-380.
- Griffiths, G., and K. Simons. 1986. The trans Golgi network: sorting at the exit site of the Golgi complex. *Science.* 234:438-43.
- Hanakam, F., R. Albrecht, C. Eckerskorn, M. Matzner, and G. Gerisch. 1996. Myristoylated and non-myristoylated forms of the pH sensor protein hisactophilin II: intracellular shuttling to plasma membrane and nucleus monitored in real time by a fusion with green fluorescent protein. *Embo J.* 15:2935-43.
- Haustein, E., and P. Schwille. 2004. Single-molecule spectroscopic methods. *Curr Opin Struct Biol.* 14:531-40.
- Hedman, K., K.L. Goldenthal, A.V. Rutherford, I. Pastan, and M.C. Willingham. 1987. Comparison of the intracellular pathways of transferrin recycling and vesicular stomatitis virus membrane glycoprotein exocytosis by ultrastructural double-label cytochemistry. *J Histochem Cytochem.* 35:233-43.
- Hell, S.W., and E.H. Stelzer. 1992. Fundamental improvement of resolution with a 4Pi-confocal microscope using two-photon excitation. *Opt. Commun.* 93:277-282.
- Hendricks, L.C., S.L. McClanahan, M. McCaffery, G.E. Palade, and M.G. Farquhar. 1992. Golgi proteins persist in the tubulovesicular remnants found in brefeldin A-treated pancreatic acinar cells. *Eur J Cell Biol.* 58:202-13.
- Henkel, A.W., L.L. Simpson, R.M. Ridge, and W.J. Betz. 1996. Synaptic vesicle movements monitored by fluorescence recovery after photobleaching in nerve terminals stained with FM1-43. *J Neurosci.* 16:3960-7.
- Henry, C. 2000. The next pharmaceutical century. In *Chem Eng News.* 85-100.

- Herscovitz, H., A. Kritis, I. Talianidis, E. Zanni, V. Zannis, and D.M. Small. 1995. Murine mammary-derived cells secrete the N-terminal 41% of human apolipoprotein B on high density lipoprotein-sized lipoproteins containing a triacylglycerol-rich core. *Proc Natl Acad Sci U S A.* 92:659-63.
- Hidalgo, J., R. Garcia-Navarro, F. Gracia-Navarro, J. Perez-Vilar, and A. Velasco. 1992. Presence of Golgi remnant membranes in the cytoplasm of brefeldin A-treated cells. *Eur J Cell Biol.* 58:214-27.
- Hirschberg, K., C.M. Miller, J. Ellenberg, J.F. Presley, E.D. Siggia, R.D. Phair, and J. Lippincott-Schwartz. 1998. Kinetic analysis of secretory protein traffic and characterization of golgi to plasma membrane transport intermediates in living cells. *J Cell Biol.* 143:1485-503.
- Houdebine, L.M. 2000. Transgenic animal bioreactors. *Transgenic Res.* 9:305-20.
- Houdebine, L.M. 2002a. Antibody manufacture in transgenic animals and comparisons with other systems. *Curr Opin Biotechnol.* 13:625-9.
- Houdebine, L.M. 2002b. Vector Design for Transgene Expression Transgenic Animal Technology. Academic Press, New York, New York. 419-458 pp.
- Humphrey, J.S., P.J. Peters, L.C. Yuan, and J.S. Bonifacino. 1993. Localization of TGN38 to the trans-Golgi network: involvement of a cytoplasmic tyrosine-containing sequence. *J Cell Biol.* 120:1123-35.
- Inouye, S., and F.I. Tsuji. 1994. Aequorea green fluorescent protein. Expression of the gene and fluorescence characteristics of the recombinant protein. *FEBS Lett.* 341:277-80.
- Ivessa, N.E., C. De Lemos-Chiarandini, D. Gravotta, D.D. Sabatini, and G. Kreibich. 1995. The Brefeldin A-induced retrograde transport from the Golgi apparatus to the endoplasmic reticulum depends on calcium sequestered to intracellular stores. *J Biol Chem.* 270:25960-7.
- Jares-Erijman, E.A., and T.M. Jovin. 2003. FRET imaging. *Nat Biotechnol.* 21:1387-95.
- Jesch, S.A., and A.D. Linstedt. 1998. The Golgi and endoplasmic reticulum remain independent during mitosis in HeLa cells. *Mol Biol Cell.* 9:623-35.
- Jiang, S., and B. Storrie. 2005. Cisternal rab proteins regulate Golgi apparatus redistribution in response to hypotonic stress. *Mol Biol Cell.* 16:2586-96.
- Jin, M., G.G. Sahagian, Jr., and M.D. Snider. 1989. Transport of surface mannose 6-phosphate receptor to the Golgi complex in cultured human cells. *J Biol Chem.* 264:7675-80.
- Johannes, L., D. Tenza, C. Antony, and B. Goud. 1997. Retrograde transport of KDEL-bearing B-fragment of Shiga toxin. *J Biol Chem.* 272:19554-61.
- Jokitalo, E., N. Cabrera-Poch, G. Warren, and D.T. Shima. 2001. Golgi clusters and vesicles mediate mitotic inheritance independently of the endoplasmic reticulum. *J Cell Biol.* 154:317-30.
- Kaether, C., and H.H. Gerdes. 1995. Visualization of protein transport along the secretory pathway using green fluorescent protein. *FEBS Lett.* 369:267-71.
- Kahn, T.W., R.N. Beachy, and M.M. Falk. 1997. Cell-free expression of a GFP fusion protein allows quantitation in vitro and in vivo. *Curr Biol.* 7:R207-8.
- Kallen, K.J., P. Quinn, and D. Allan. 1993. Monensin inhibits synthesis of plasma membrane sphingomyelin by blocking transport of ceramide through the Golgi: evidence for two sites of sphingomyelin synthesis in BHK cells. *Biochim Biophys Acta.* 1166:305-8.
- Kaparissides, C., S. Alexandridou, K. Kotti, and S. Chaitidou. 2006. Recent Advances in Novel Drug Delivery Systems. *Journal of Nanotechnology Online.* 2:1-11.
- Karyłowski, O., A. Zeigerer, A. Cohen, and T.E. McGraw. 2004. GLUT4 is retained by an intracellular cycle of vesicle formation and fusion with endosomes. *Mol Biol Cell.* 15:870-82.
- Kasap, M., S. Thomas, E. Danaher, V. Holton, S. Jiang, and B. Storrie. 2004. Dynamic nucleation of Golgi apparatus assembly from the endoplasmic reticulum in interphase hela cells. *Traffic.* 5:595-605.

- Keller, P., D. Toomre, E. Diaz, J. White, and K. Simons. 2001. Multicolour imaging of post-Golgi sorting and trafficking in live cells. *Nat Cell Biol.* 3:140-9.
- Kim, J.H., L. Johannes, B. Goud, C. Antony, C.A. Lingwood, R. Daneman, and S. Grinstein. 1998. Noninvasive measurement of the pH of the endoplasmic reticulum at rest and during calcium release. *Proc Natl Acad Sci U S A.* 95:2997-3002.
- Klar, T.A., S. Jakobs, M. Dyba, A. Egner, and S.W. Hell. 2000. Fluorescence microscopy with diffraction resolution barrier broken by stimulated emission. *Proc Natl Acad Sci U S A.* 97:8206-10.
- Klausner, R.D., J.G. Donaldson, and J. Lippincott-Schwartz. 1992. Brefeldin A: insights into the control of membrane traffic and organelle structure. *J Cell Biol.* 116:1071-80.
- Kornfeld, R., and S. Kornfeld. 1985. Assembly of asparagine-linked oligosaccharides. *Annu Rev Biochem.* 54:631-64.
- Koster, A.J., and J. Klumperman. 2003. Electron microscopy in cell biology: integrating structure and function. *Nat Rev Mol Cell Biol.* Suppl:SS6-10.
- Koyama-Honda, I., K. Ritchie, T. Fujiwara, R. Iino, H. Murakoshi, R.S. Kasai, and A. Kusumi. 2005. Fluorescence imaging for monitoring the colocalization of two single molecules in living cells. *Biophys J.* 88:2126-36.
- Kreis, T.E. 1986. Microinjected antibodies against the cytoplasmic domain of vesicular stomatitis virus glycoprotein block its transport to the cell surface. *Embo J.* 5:931-41.
- Kreitzer, G., J. Schmoranzer, S.H. Low, X. Li, Y. Gan, T. Weimbs, S.M. Simon, and E. Rodriguez-Boulan. 2003. Three-dimensional analysis of post-Golgi carrier exocytosis in epithelial cells. *Nat Cell Biol.* 5:126-36.
- Landmann, L. 2002. Deconvolution improves colocalization analysis of multiple fluorochromes in 3D confocal data sets more than filtering techniques. *J Microsc.* 208:134-47.
- Lang, T., I. Wacker, J. Steyer, C. Kaether, I. Wunderlich, T. Soldati, H.H. Gerdes, and W. Almers. 1997. Ca²⁺-triggered peptide secretion in single cells imaged with green fluorescent protein and evanescent-wave microscopy. *Neuron.* 18:857-63.
- Lee, M.C., E.A. Miller, J. Goldberg, L. Orci, and R. Schekman. 2004. Bi-directional protein transport between the ER and Golgi. *Annu Rev Cell Dev Biol.* 20:87-123.
- Lim, C.R., Y. Kimata, M. Oka, K. Nomaguchi, and K. Kohno. 1995. Thermosensitivity of green fluorescent protein fluorescence utilized to reveal novel nuclear-like compartments in a mutant nucleoporin NSP1. *J Biochem (Tokyo).* 118:13-7.
- Linstedt, A.D. 1999. Stacking the cisternae. *Curr Biol.* 9:R893-6.
- Linstedt, A.D., A. Mehta, J. Suhan, H. Reggio, and H.P. Hauri. 1997. Sequence and overexpression of GPP130/GIMPc: evidence for saturable pH-sensitive targeting of a type II early Golgi membrane protein. *Mol Biol Cell.* 8:1073-87.
- Lippincott-Schwartz, J., N. Cole, and J. Presley. 1998. Unravelling Golgi membrane traffic with green fluorescent protein chimeras. *Trends Cell Biol.* 8:16-20.
- Lippincott-Schwartz, J., L.C. Yuan, J.S. Bonifacino, and R.D. Klausner. 1989. Rapid redistribution of Golgi proteins into the ER in cells treated with brefeldin A: evidence for membrane cycling from Golgi to ER. *Cell.* 56:801-13.
- Lock, J.G., and J.L. Stow. 2005. Rab11 in recycling endosomes regulates the sorting and basolateral transport of E-cadherin. *Mol Biol Cell.* 16:1744-55.
- Love, H.D., C.C. Lin, C.S. Short, and J. Ostermann. 1998. Isolation of functional Golgi-derived vesicles with a possible role in retrograde transport. *J Cell Biol.* 140:541-51.
- Lucocq, J.M., E.G. Berger, and G. Warren. 1989. Mitotic Golgi fragments in HeLa cells and their role in the reassembly pathway. *J Cell Biol.* 109:463-74.
- Lucocq, J.M., J.G. Pryde, E.G. Berger, and G. Warren. 1987. A mitotic form of the Golgi apparatus in HeLa cells. *J Cell Biol.* 104:865-74.
- Lucocq, J.M., and G. Warren. 1987. Fragmentation and partitioning of the Golgi apparatus during mitosis in HeLa cells. *Embo J.* 6:3239-46.

- Majoul, I. 2004. Analysing the action of bacterial toxins in living cells with fluorescence resonance energy transfer (FRET). *Int J Med Microbiol.* 293:495-503.
- Mallard, F., C. Antony, D. Tenza, J. Salamero, B. Goud, and L. Johannes. 1998. Direct pathway from early/recycling endosomes to the Golgi apparatus revealed through the study of shiga toxin B-fragment transport. *J Cell Biol.* 143:973-90.
- Mallet, W.G., and F.R. Maxfield. 1999. Chimeric forms of furin and TGN38 are transported with the plasma membrane in the trans-Golgi network via distinct endosomal pathways. *J Cell Biol.* 146:345-59.
- Mardones, G.A., C.M. Snyder, and K.E. Howell. 2006. Cis-Golgi matrix proteins move directly to endoplasmic reticulum exit sites by association with tubules. *Mol Biol Cell.* 17:525-38.
- Marnell, M.H., M. Stookey, and R.K. Draper. 1982. Monensin blocks the transport of diphtheria toxin to the cell cytoplasm. *J Cell Biol.* 93:57-62.
- Marshall, J., R. Molloy, G.W. Moss, J.R. Howe, and T.E. Hughes. 1995. The jellyfish green fluorescent protein: a new tool for studying ion channel expression and function. *Neuron.* 14:211-5.
- Maul, G.G., and B.R. Brinkley. 1970. The golgi apparatus during mitosis in human melanoma cells in vitro. *Cancer Res.* 30:2326-35.
- Mellman, I., and K. Simons. 1992. The Golgi complex: in vitro veritas? *Cell.* 68:829-40.
- Miaczynska, M., L. Pelkmans, and M. Zerial. 2004. Not just a sink: endosomes in control of signal transduction. *Curr Opin Cell Biol.* 16:400-6.
- Michalet, X., A.N. Kapanidis, T. Laurence, F. Pinaud, S. Doose, M. Pflughoefft, and S. Weiss. 2003. The power and prospects of fluorescence microscopies and spectroscopies. *Annu Rev Biophys Biomol Struct.* 32:161-82.
- Miles, S., H. McManus, K.E. Forsten, and B. Storrie. 2001. Evidence that the entire Golgi apparatus cycles in interphase HeLa cells: sensitivity of Golgi matrix proteins to an ER exit block. *J Cell Biol.* 155:543-55.
- Misteli, T., and G. Warren. 1995. Mitotic disassembly of the Golgi apparatus in vivo. *J Cell Sci.* 108 (Pt 7):2715-27.
- Miyawaki, A., J. Llopis, R. Heim, J.M. McCaffery, J.A. Adams, M. Ikura, and R.Y. Tsien. 1997. Fluorescent indicators for Ca²⁺ based on green fluorescent proteins and calmodulin. *Nature.* 388:882-7.
- Miyawaki, A., A. Sawano, and T. Kogure. 2003. Lighting up cells: labelling proteins with fluorophores. *Nat Cell Biol.* Suppl:S1-7.
- Mollenhauer, H.H., D.J. Morre, and L.D. Rowe. 1990. Alteration of intracellular traffic by monensin; mechanism, specificity and relationship to toxicity. *Biochim Biophys Acta.* 1031:225-46.
- Molloy, S.S., L. Thomas, J.K. VanSlyke, P.E. Stenberg, and G. Thomas. 1994. Intracellular trafficking and activation of the furin proprotein convertase: localization to the TGN and recycling from the cell surface. *Embo J.* 13:18-33.
- Moore, J.C. 1974. The Golgi tendon organ and the muscle spindle. *Am J Occup Ther.* 28:415-20.
- Moriyama, Y., and N. Nelson. 1989. H⁺-translocating ATPase in Golgi apparatus. Characterization as vacuolar H⁺-ATPase and its subunit structures. *J Biol Chem.* 264:18445-50.
- Murphy, D.B. 2001. Fundamentals of light microscopy and electronic imaging. John Wiley & Sons, New York.
- Murray, A.W., and M.W. Kirschner. 1989. Dominoes and clocks: the union of two views of the cell cycle. *Science.* 246:614-21.
- Nakamura, N., C. Rabouille, R. Watson, T. Nilsson, N. Hui, P. Slusarewicz, T.E. Kreis, and G. Warren. 1995. Characterization of a cis-Golgi matrix protein, GM130. *J Cell Biol.* 131:1715-26.

- Natarajan, R., and A.D. Linstedt. 2004. A cycling cis-Golgi protein mediates endosome-to-Golgi traffic. *Mol Biol Cell*. 15:4798-806.
- Nilsson, T., M. Pypaert, M.H. Hoe, P. Slusarewicz, E.G. Berger, and G. Warren. 1993. Overlapping distribution of two glycosyltransferases in the Golgi apparatus of HeLa cells. *J Cell Biol*. 120:5-13.
- Nishi, T., and M. Forgac. 2002. The vacuolar (H⁺)-ATPases--nature's most versatile proton pumps. *Nat Rev Mol Cell Biol*. 3:94-103.
- Nishikawa, S., J.L. Brodsky, and K. Nakatsukasa. 2005. Roles of molecular chaperones in endoplasmic reticulum (ER) quality control and ER-associated degradation (ERAD). *J Biochem (Tokyo)*. 137:551-5.
- Niswender, K.D., S.M. Blackman, L. Rohde, M.A. Magnuson, and D.W. Piston. 1995. Quantitative imaging of green fluorescent protein in cultured cells: comparison of microscopic techniques, use in fusion proteins and detection limits. *J Microsc*. 180 (Pt 2):109-16.
- Nyquist, H. 1928. Certain topics in telegraph transmission theory. *Trans AIEE*. 47:617-644.
- Orci, L., M. Stammes, M. Ravazzola, M. Amherdt, A. Perrelet, T.H. Sollner, and J.E. Rothman. 1997. Bidirectional transport by distinct populations of COPI-coated vesicles. *Cell*. 90:335-49.
- Orlandi, P.A., P.K. Curran, and P.H. Fishman. 1993. Brefeldin A blocks the response of cultured cells to cholera toxin. Implications for intracellular trafficking in toxin action. *J Biol Chem*. 268:12010-6.
- Orzech, E., S. Cohen, A. Weiss, and B. Aroeti. 2000. Interactions between the exocytic and endocytic pathways in polarized Madin-Darby canine kidney cells. *J Biol Chem*. 275:15207-19.
- Ostermann, J., L. Orci, K. Tani, M. Amherdt, M. Ravazzola, Z. Elazar, and J.E. Rothman. 1993. Stepwise assembly of functionally active transport vesicles. *Cell*. 75:1015-25.
- Palade, G. 1975. Intracellular aspects of the process of protein synthesis. *Science*. 189:347-58.
- Paulson, J.C., and K.J. Colley. 1989. Glycosyltransferases. Structure, localization, and control of cell type-specific glycosylation. *J Biol Chem*. 264:17615-8.
- Peet, J.A., A. Bragin, P.D. Calvert, S.S. Nikonorov, S. Mani, X. Zhao, J.C. Besharse, E.A. Pierce, B.E. Knox, and E.N. Pugh, Jr. 2004. Quantification of the cytoplasmic spaces of living cells with EGFP reveals arrestin-EGFP to be in disequilibrium in dark adapted rod photoreceptors. *J Cell Sci*. 117:3049-59.
- Pelham, H.R. 1991. Multiple targets for brefeldin A. *Cell*. 67:449-51.
- Pelham, H.R. 1997. Membrane transport. Green light for Golgi traffic. *Nature*. 389:17, 19.
- Pelham, H.R. 1998. Getting through the Golgi complex. *Trends Cell Biol*. 8:45-9.
- Pelham, H.R. 2001. Traffic through the Golgi apparatus. *J Cell Biol*. 155:1099-101.
- Pelletier, L., E. Jokitalo, and G. Warren. 2000. The effect of Golgi depletion on exocytic transport. *Nat Cell Biol*. 2:840-6.
- Perret, E., A. Lakkaraju, S. Deborde, R. Schreiner, and E. Rodriguez-Boulan. 2005. Evolving endosomes: how many varieties and why? *Curr Opin Cell Biol*. 17:423-34.
- Pfeffer, S.R., and J.E. Rothman. 1987. Biosynthetic protein transport and sorting by the endoplasmic reticulum and Golgi. *Annu Rev Biochem*. 56:829-52.
- Phillips, G.N., Jr. 1997. Structure and dynamics of green fluorescent protein. *Curr Opin Struct Biol*. 7:821-7.
- Potter, S.M., C.M. Wang, P.A. Garrity, and S.E. Fraser. 1996. Intravital imaging of green fluorescent protein using two-photon laser-scanning microscopy. *Gene*. 173:25-31.
- Prasher, D.C., V.K. Eckenrode, W.W. Ward, F.G. Prendergast, and M.J. Cormier. 1992. Primary structure of the *Aequorea victoria* green-fluorescent protein. *Gene*. 111:229-33.
- Presley, J.F. 2005. Imaging the secretory pathway: the past and future impact of live cell optical techniques. *Biochim Biophys Acta*. 1744:259-72.

- Presley, J.F., N.B. Cole, T.A. Schroer, K. Hirschberg, K.J. Zaal, and J. Lippincott-Schwartz. 1997. ER-to-Golgi transport visualized in living cells. *Nature*. 389:81-5.
- Pressman, B.C. 1968. Ionophorous antibiotics as models for biological transport. *Fed Proc*. 27:1283-8.
- Puranam, K.L., D.W. Laird, and J.P. Revel. 1993. Trapping an intermediate form of connexin43 in the Golgi. *Exp Cell Res*. 206:85-92.
- Puri, S., C. Bachert, C.J. Fimmel, and A.D. Linstedt. 2002. Cycling of early Golgi proteins via the cell surface and endosomes upon luminal pH disruption. *Traffic*. 3:641-53.
- Puri, S., and A.D. Linstedt. 2003. Capacity of the Golgi apparatus for biogenesis from the endoplasmic reticulum. *Mol Biol Cell*. 14:5011-8.
- Puthenveedu, M.A., J.R. Bruns, O.A. Weisz, and A.D. Linstedt. 2003. Basolateral cycling mediated by a luminal domain targeting determinant. *Mol Biol Cell*. 14:1801-7.
- Rabouille, C., N. Hui, F. Hunte, R. Kieckbusch, E.G. Berger, G. Warren, and T. Nilsson. 1995. Mapping the distribution of Golgi enzymes involved in the construction of complex oligosaccharides. *J Cell Sci*. 108 (Pt 4):1617-27.
- Rambour, A., Y. Clermont, L. Hermo, and D. Segretain. 1987. Tridimensional architecture of the Golgi apparatus and its components in mucous cells of Brunner's glands of the mouse. *Am J Anat*. 179:95-107.
- Randazzo, P.A., Y.C. Yang, C. Rulka, and R.A. Kahn. 1993. Activation of ADP-ribosylation factor by Golgi membranes. Evidence for a brefeldin A- and protease-sensitive activating factor on Golgi membranes. *J Biol Chem*. 268:9555-63.
- Rhee, S.W., T. Starr, K. Forsten-Williams, and B. Storrie. 2005. The steady-state distribution of glycosyltransferases between the Golgi apparatus and the endoplasmic reticulum is approximately 90:10. *Traffic*. 6:978-90.
- Rindler, M.J., I.E. Ivanov, H. Plesken, and D.D. Sabatini. 1985. Polarized delivery of viral glycoproteins to the apical and basolateral plasma membranes of Madin-Darby canine kidney cells infected with temperature-sensitive viruses. *J Cell Biol*. 100:136-51.
- Rivas, R.J., and H.P. Moore. 1989. Spatial segregation of the regulated and constitutive secretory pathways. *J Cell Biol*. 109:51-60.
- Rizzuto, R., M. Brini, F. De Giorgi, R. Rossi, R. Heim, R.Y. Tsien, and T. Pozzan. 1996. Double labelling of subcellular structures with organelle-targeted GFP mutants in vivo. *Curr Biol*. 6:183-8.
- Rose, J.K., and J.E. Bergmann. 1983. Altered cytoplasmic domains affect intracellular transport of the vesicular stomatitis virus glycoprotein. *Cell*. 34:513-24.
- Roth, J. 1991. Localization of glycosylation sites in the Golgi apparatus using immunolabeling and cytochemistry. *J Electron Microsc Tech*. 17:121-31.
- Roth, J., and E.G. Berger. 1982. Immunocytochemical localization of galactosyltransferase in HeLa cells: codistribution with thiamine pyrophosphatase in trans-Golgi cisternae. *J Cell Biol*. 93:223-9.
- Rothman, J.E. 1994. Mechanisms of intracellular protein transport. *Nature*. 372:55-63.
- Rothman, J.E., and F.T. Wieland. 1996. Protein sorting by transport vesicles. *Science*. 272:227-34.
- Röttger, S., J. White, H.H. Wandall, J.C. Olivo, A. Stark, E.P. Bennett, C. Whitehouse, E.G. Berger, H. Clausen, and T. Nilsson. 1998. Localization of three human polypeptide GalNAc-transferases in HeLa cells suggests initiation of O-linked glycosylation throughout the Golgi apparatus. *J Cell Sci*. 111 (Pt 1):45-60.
- Saino, T., and Y. Satoh. 2004. Application of real-time confocal laser scanning microscopy to observe living cells in tissue specimens. *J Electron Microsc (Tokyo)*. 53:49-56.
- Sandvig, K., O. Garred, K. Prydz, J.V. Kozlov, S.H. Hansen, and B. van Deurs. 1992. Retrograde transport of endocytosed Shiga toxin to the endoplasmic reticulum. *Nature*. 358:510-2.

- Sandvig, K., S. Olsnes, J.E. Brown, O.W. Petersen, and B. van Deurs. 1989. Endocytosis from coated pits of Shiga toxin: a glycolipid-binding protein from *Shigella dysenteriae* 1. *J Cell Biol.* 108:1331-43.
- Sandvig, K., and B. van Deurs. 2002. Transport of protein toxins into cells: pathways used by ricin, cholera toxin and Shiga toxin. *FEBS Lett.* 529:49-53.
- Saraste, J., and E. Kuismanen. 1984. Pre- and post-Golgi vacuoles operate in the transport of Semliki Forest virus membrane glycoproteins to the cell surface. *Cell.* 38:535-49.
- Schirmer, J., and K. Aktories. 2004. Large clostridial cytotoxins: cellular biology of Rho/Ras-glucosylating toxins. *Biochim Biophys Acta.* 1673:66-74.
- Schmoranzer, J., M. Goulian, D. Axelrod, and S.M. Simon. 2000. Imaging constitutive exocytosis with total internal reflection fluorescence microscopy. *J Cell Biol.* 149:23-32.
- Schwarzmann, K., L.M. Cruz-Orive, R. Eggman, A. Sanger, and E.R. Weibel. 1986. Molecular architecture of the inner membrane of mitochondria from rat liver: a combined biochemical and stereological study. *J Cell Biol.* 102:97-103.
- Seemann, J., E. Jokitalo, M. Pypaert, and G. Warren. 2000. Matrix proteins can generate the higher order architecture of the Golgi apparatus. *Nature.* 407:1022-6.
- Shimomura, O., F.H. Johnson, and Y. Saiga. 1962. Extraction, purification and properties of aequorin, a bioluminescent protein from the luminous hydromedusan, *Aequorea*. *J Cell Comp Physiol.* 59:223-39.
- Soler, E., A. Le Saux, F. Guinut, B. Passet, R. Cohen, C. Merle, A. Charpilienne, C. Fourgeux, V. Sorel, A. Piriou, I. Schwartz-Cornil, J. Cohen, and L.M. Houdebine. 2005. Production of two vaccinating recombinant rotavirus proteins in the milk of transgenic rabbits. *Transgenic Res.* 14:833-44.
- Sonnickson, B., R. Watson, H. Clausen, T. Misteli, and G. Warren. 1996. Sorting by COP I-coated vesicles under interphase and mitotic conditions. *J Cell Biol.* 134:1411-25.
- Stephens, D.J., and V.J. Allan. 2003. Light microscopy techniques for live cell imaging. *Science.* 300:82-6.
- Stoorvogel, W. 1998. Analysis of the endocytic system by using horseradish peroxidase. *Trends Cell Biol.* 8:503-5.
- Storrie, B. 2005. Maintenance of Golgi apparatus structure in the face of continuous protein recycling to the endoplasmic reticulum: making ends meet. *Int Rev Cytol.* 244:69-94.
- Storrie, B., and T. Nilsson. 2002. The Golgi apparatus: balancing new with old. *Traffic.* 3:521-9.
- Storrie, B., R. Pepperkok, and T. Nilsson. 2000. Breaking the COPI monopoly on Golgi recycling. *Trends Cell Biol.* 10:385-91.
- Storrie, B., R. Pepperkok, E.H. Stelzer, and T.E. Kreis. 1994. The intracellular mobility of a viral membrane glycoprotein measured by confocal microscope fluorescence recovery after photobleaching. *J Cell Sci.* 107 (Pt 5):1309-19.
- Storrie, B., J. White, S. Rottger, E.H. Stelzer, T. Suganuma, and T. Nilsson. 1998. Recycling of golgi-resident glycosyltransferases through the ER reveals a novel pathway and provides an explanation for nocodazole-induced Golgi scattering. *J Cell Biol.* 143:1505-21.
- Stryer, L., and R.P. Haugland. 1967. Energy transfer: a spectroscopic ruler. *Proc Natl Acad Sci U S A.* 58:719-26.
- Subramanian, K., and T. Meyer. 1997. Calcium-induced restructuring of nuclear envelope and endoplasmic reticulum calcium stores. *Cell.* 89:963-71.
- Swaminathan, K., P. Flynn, R.J. Reece, and R. Marmorstein. 1997. Crystal structure of a PUT3-DNA complex reveals a novel mechanism for DNA recognition by a protein containing a Zn₂Cys₆ binuclear cluster. *Nat Struct Biol.* 4:751-9.
- Swedlow, J.R. 2003. Quantitative fluorescence microscopy and image deconvolution. *Methods Cell Biol.* 72:349-67.
- Tang, B.L., Y. Wang, Y.S. Ong, and W. Hong. 2005. COPII and exit from the endoplasmic reticulum. *Biochim Biophys Acta.* 1744:293-303.

- Tarrago-Trani, M.T., and B. Storrie. 2004. A method for the purification of Shiga-like toxin 1 subunit B using a commercially available galabiose-agarose resin. *Protein Expr Purif.* 38:170-6.
- Tartakoff, A.M. 1983. Perturbation of vesicular traffic with the carboxylic ionophore monensin. *Cell.* 32:1026-8.
- Tartakoff, A.M., and P. Vassalli. 1977. Plasma cell immunoglobulin secretion: arrest is accompanied by alterations of the golgi complex. *J Exp Med.* 146:1332-45.
- Thilo, L., E. Stroud, and T. Haylett. 1995. Maturation of early endosomes and vesicular traffic to lysosomes in relation to membrane recycling. *J Cell Sci.* 108 (Pt 4):1791-803.
- Tsien, R.Y. 1998. The green fluorescent protein. *Annu Rev Biochem.* 67:509-44.
- Van Cott, K.E., and W.H. Velander. 1998. Transgenic animals as drug factories: a new source of recombinant protein therapeutics. *Expert Opin Investig Drugs.* 7:1683-90.
- Vertel, B.M., L.M. Walters, and D. Mills. 1992. Subcompartments of the endoplasmic reticulum. *Semin Cell Biol.* 3:325-41.
- Wacker, I., C. Kaether, A. Kromer, A. Migala, W. Almers, and H.H. Gerdes. 1997. Microtubule-dependent transport of secretory vesicles visualized in real time with a GFP-tagged secretory protein. *J Cell Sci.* 110 (Pt 13):1453-63.
- Wallace, W., L.H. Schaefer, and J.R. Swedlow. 2001. A workingperson's guide to deconvolution in light microscopy. *Biotechniques.* 31:1076-8, 1080, 1082 passim.
- Ward, T.H., R.S. Polishchuk, S. Caplan, K. Hirschberg, and J. Lippincott-Schwartz. 2001. Maintenance of Golgi structure and function depends on the integrity of ER export. *J Cell Biol.* 155:557-70.
- Warren, G. 1993. Membrane partitioning during cell division. *Annu Rev Biochem.* 62:323-48.
- Waters, M.G., D.O. Clary, and J.E. Rothman. 1992. A novel 115-kD peripheral membrane protein is required for intercisternal transport in the Golgi stack. *J Cell Biol.* 118:1015-26.
- Watson P, S.D. 2005. ER-to-Golgi trasport: Form and formationof vesicular and tubular carriers. *Biochimica et Biophysica Acta.* 1774:304-315.
- Webb RH, D.C. 1995. The pixelated image. *Handbook of Biological Confocal Microscopy.* Plenum Press, New York, New York. 55-67 pp.
- Wustner, D. 2005. Mathematical analysis of hepatic high density lipoprotein transport based on quantitative imaging data. *J Biol Chem.* 280:6766-79.
- Yamashina, S. 1995. Dynamic structure and function of Golgi apparatus in the salivary acinar cells. *J Electron Microsc (Tokyo).* 44:124-34.
- Yang, F., L.G. Moss, and G.N. Phillips, Jr. 1996. The molecular structure of green fluorescent protein. *Nat Biotechnol.* 14:1246-51.
- Yang, W., and B. Storrie. 1998. Scattered Golgi elements during microtubule disruption are initially enriched in trans-Golgi proteins. *Mol Biol Cell.* 9:191-207.
- Yano, M., M. Kanazawa, K. Terada, C. Namchai, M. Yamaizumi, B. Hanson, N. Hoogenraad, and M. Mori. 1997. Visualization of mitochondrial protein import in cultured mammalian cells with green fluorescent protein and effects of overexpression of the human import receptor Tom20. *J Biol Chem.* 272:8459-65.
- Yokoe, H., and T. Meyer. 1996. Spatial dynamics of GFP-tagged proteins investigated by local fluorescence enhancement. *Nat Biotechnol.* 14:1252-6.
- Zaal, K.J., C.L. Smith, R.S. Polishchuk, N. Altan, N.B. Cole, J. Ellenberg, K. Hirschberg, J.F. Presley, T.H. Roberts, E. Sigga, R.D. Phair, and J. Lippincott-Schwartz. 1999. Golgi membranes are absorbed into and reemerge from the ER during mitosis. *Cell.* 99:589-601.
- Zemanova, L., A. Schenk, M.J. Valler, G.U. Nienhaus, and R. Heilker. 2003. Confocal optics microscopy for biochemical and cellular high-throughput screening. *Drug Discov Today.* 8:1085-93.

APPENDIX 1: STEREOLOGY

Stereology is a classical method used to estimate the area, volume, or length fraction of an object relative to a sample space using simple ratios of measurable quantities (Griffiths, 1993). The basic theory of stereology relies on the principle of random sampling and states that the larger or more frequent occurrence of an object in the total sample space increases the probability of it being randomly measured. This principle only holds true if a sufficient number of **random** values is measured. (Figure 1)

The amount of gold labeling in most immunocytochemical experiments is related to the volume, surface area, or length of the structure being measured (Griffiths, 1993). Our studies were focused on determining the relative particle densities of GalNAcT2-VSV in the ER, Golgi, and Golgi tubules. It has been proven that the profile area of an object relative to the total sample area is equal to the ratio of the volumes of the measured object and total reference space (Weibel 1980). The most efficient method for estimating the total area of the sample sections is point counting. By using a systematic system of test points (grid, see Figure 1) the fraction of sample point hits for an object ($\sum \text{Golgi}_{\text{intersections}}$) relative to the total point hits for the sample space ($\sum \text{cell}_{\text{intersections}}$), is related to the area fraction of that object (Weibel 1980, Mayhew 1983) as shown in:

$$\frac{\sum \text{Golgi}_{\text{intersections}}}{\sum \text{cell}_{\text{intersections}}} = \frac{\text{Golgi}_{\text{area}}}{\text{cell}_{\text{area}}} \quad (1)$$

Additionally, if the magnification of the micrographs relative to the sampling grid size is known, it is possible to determine the area of the sampled space from the number of grid intersections (Figure 2) which can then be used to quantitate the particle density in gold-labeling experiments.

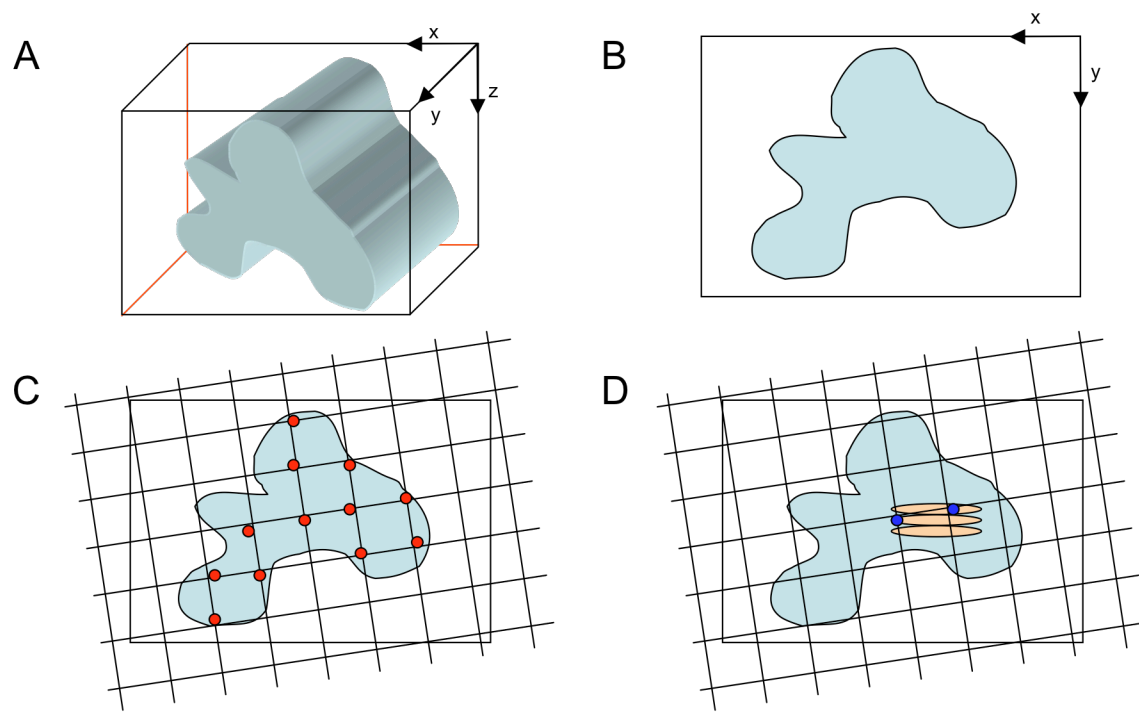


Figure 1. Stereology. A structure is embedded in a 3-D reference space (A) and a random section is shown (B). This random section is sampled using a grid and the point counting method. The total intersections of the reference space are shown in red (C) while the intersections of the object of interest (D orange) are marked in blue. The relative area fraction of the object is the ratio of the mean of N measured sections (blue intersections) and the total space (red intersections). N must be large for this to be true.

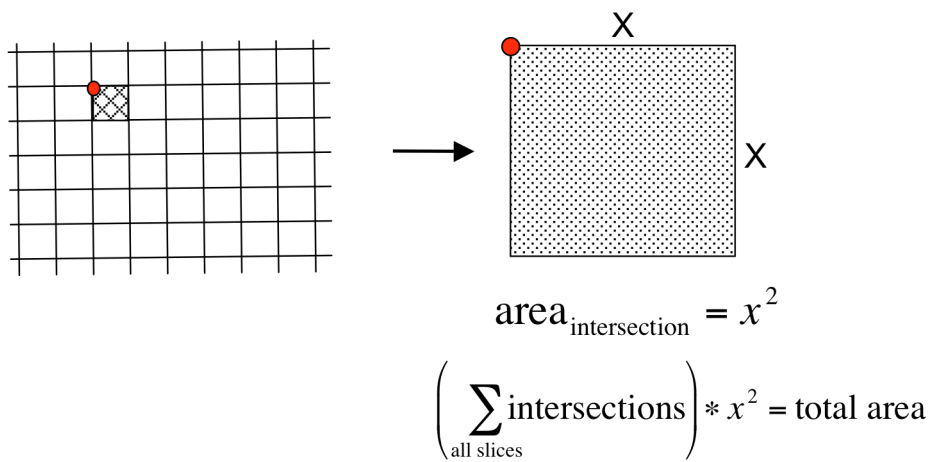


Figure 2. Stereology Grid. A single intersection represents the area of one grid square. If the dimensions of the grid square are known relative to actual distance on the micrographs (x), the area of object can be found (x^2). The sum of the intersections for the object (\sum intersections) over all the micrographs multiplied by the area of a single intersection (x^2) gives the total area for that object in the space measured.

APPENDIX 2: ELECTRON MICROGRAPH ANALYSIS

Our electron microscopy (EM) analysis included two parts; (1) calculation of GalNAcT2-VSV *protein labeling densities* in the Golgi cisternae, tubules, and ER and (2) calculation of relative *protein distributions* of GalNAcT2-VSV in the Golgi apparatus and ER. Higher magnification images (34,000x) were analyzed to determine the protein densities using both gold particle quantification and stereology. Particle density, our measure of protein density is defined as:

$$\text{particle density } (\delta) = \frac{\text{gold particles } (\#)}{\text{area } (\mu\text{m}^2)} \quad (1)$$

At the 34,000 magnification we were able to distinguish both the Golgi cisternae and tubular structures as well as the ER (See Chapter 3 Figure 2). Also, this high magnification allowed us to reliably identify the gaps between the cisternae. For this reason, we measured the areas values (using stereology) for the Golgi cisternae with and without the regions between (UA_{block} and $UA_{cisternae}$, respectively).

The lower magnification images (16,000x and 10,000x) were analyzed to determine the relative protein distributions of the GalNAcT2-VSV protein in the Golgi and ER. Again stereology was used to quantify the relative areas of the Golgi (LA_{block}) and ER (LA_{ER}). It is important to note that at the lower magnifications it is not possible to distinguish the tubules or space between cisternae. To compensate, we used ratios of the area values measured at the upper magnification ($UA_{cisternae}$, UA_{block} , $UA_{tubules}$, UA_{block}) to determine the cisternal and tubular areas ($LA_{cisternae}$ and $LA_{tubules}$, respectively) as defined by:

$$LA_{cisternae} (\mu\text{m}^2) = \left(\frac{UA_{cisternae}}{UA_{block}} \right) * LA_{block} \quad (2 \& 3)$$

$$LA_{tubules} (\mu\text{m}^2) = \left(\frac{UA_{tubules}}{UA_{block}} \right) * LA_{block}$$

The total Golgi area (LA_{Golgi}) is the sum of the cisternal and tubular calculated values.

$$LA_{Golgi} (\mu\text{m}^2) = LA_{cisternae} + LA_{tubules} \quad (4)$$

To determine the relative amounts of GalNAcT2-VSV protein in the Golgi and ER we used the protein density calculated at the higher magnification (δ_{Golgi} , δ_{ER}) and the relative areas calculated at the lower magnifications (LA_{Golgi} and LA_{ER}) using:

$$Golgi_{\text{GalNAcT2-VSV}} = \frac{\delta_{\text{Golgi}} * LA_{\text{Golgi}}}{(\delta_{\text{Golgi}} * LA_{\text{Golgi}}) + (\delta_{\text{ER}} * LA_{\text{ER}})} \quad (5 \& 6)$$

$$ER_{\text{GalNAcT2-VSV}} = 1 - Golgi_{\text{GalNAcT2-VSV}}$$

APPENDIX 3: PIXEL SHIFT

Proper alignment between images is an important consideration whenever multiple channels are superimposed (merge channels) such as when the spatial relationship of two molecules within a cell is being examined. Even a small change in the XY-coordinates recorded by the camera can result in a misrepresentation of the interactions and/or relative positions of the two molecules. This is particularly true if you are using the computer to correlate overlap as done in this dissertation. Planar imperfections on the surface of the optical filters can cause a shift in the image acquired by the camera when switching between filter sets, hence the term pixel shift. This shift is the result of beam deviation that is usually caused by a non-zero wedge angle in the filter coating (non-parallelism) (Erdogan, 2005). If there are imperfections on the surface of the filters, the emerging beam will deviate from its incident path (Figure 1A).

For the portion of my experiments involving the spinning disk confocal system, the multi-channel images were acquired by switching between the fluorescein isothiocyanate (FITC) and tetramethylrhodamine isothiocyanate (TRITC) filter sets that corresponded to the two fluorophores of interest, GFP and Cy3 respectively. To determine if pixel shift was occurring, WT HeLa cells were stained with anti-GM130 primary antibody followed by both cyanine 2 (Cy2) and cyanine 3 (Cy3) secondary antibodies. Cy3 and Cy2 fluorophores were chosen because they corresponded to the TRITC and FITC channels, respectively, used in my experiments. The resulting images showed an ~ 1-2 pixel shift between channels in the lateral direction (Figure 1B) corresponding to a distance of ~150nm. As a comparison, at the resolution of the light microscope, the Golgi appears as an ~6 μm long and ~2 μm wide ribbon-like structure (Storrie et al., 1998). Manufacturing standards reported a standard deviation of ± 1 pixel shift in the XY-plane allowing us to conclude that our results are within the limitations of the filters. The figure below shows the FITC (Cy2, green), TRITC (Cy3, red) images merged (yellow) before and after (Figure 1C) pixel shift is corrected for a WT cell stained with GM130. The pixel shift was corrected by moving the Cy2 channel (green) 2 pixels with respect to the Cy3 channel (red). This pixel shift was not corrected in our studies involving the colocalization of GPP130 and GalNAcT2-GFP, but instead was compensated in the analysis by scaling the time points with respect to the zero time point (100% colocalization).

Similar experiments were performed for the laser scanning confocal microscope (LSM510). A LSM confocal scans the sample sequentially point-by-point, line-by-line, and then assembles the

pixel information in one image. A photomultiplier tube is used for detection of the photons emitted at each pixel scanned versus the camera used by the spinning disk. Combined, these factors help reduce the appearance of pixel shift. However, the system still includes both dichroic mirrors and filters capable of introducing a shift when multiple channel configurations are used. For these reasons, cells were stained with anti-GM130 primary antibody and Cy3 and Cy5 secondary antibodies to measure the pixel shift for these corresponding channels (Figure 1D). The distance corresponding to the pixel shift found was measured for each individual experiment and subtracted from the distance measurements for other proteins imaged using the same channels. Suggestions for reducing the presence of a pixel shift between channels with the LSM510 are to (1) be sure that pinholes are the same size for all channels, (2) properly oversample, and (3) acquire images in line with the light path (usually center of the field-of-view).

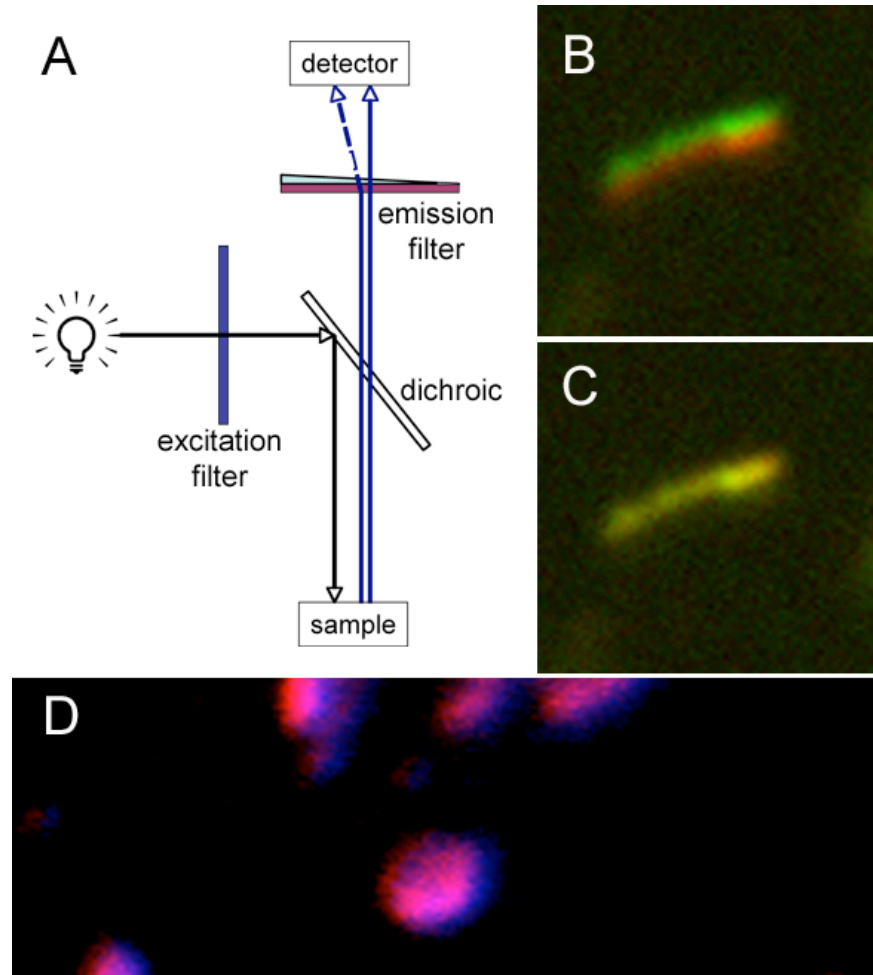


Figure 1. Pixel Shift. Simplified diagram of the optical light path (A) demonstrating the effect of filter imperfections on beam deviation. Immunofluorescence staining of the Golgi protein GM130 with Cy2 (green) and Cy3 (red) secondary antibodies is shown before (B) and after (C) pixel shift correction for spinning disk confocal images. The pixel shift associated with the LSM 510 was measured using similar anti-GM130 staining with Cy3 (magenta) and Cy5 (blue) secondary antibodies as shown in D.

APPENDIX 4: MICROSCOPY TERMS

Included in this appendix is a brief summary of terms and concepts relating to light microscopy and deconvolution.

Wavelength (λ): The distance between repeating units of a wave pattern. Excitation (λ_{ex}) and emission (λ_{em}) wavelengths for fluorophores referenced in this dissertation are listed in Table 1. Note that the emission wavelength is always longer than the excitation wavelength.

Refractive Index (n): The factor by which the wave is slowed in a material. The medium refractive index is that of the embedding or mounting medium. Please see Table 2 for a list of the refractive indexes of common materials.

Numerical Aperture (NA): Measure of the ability of a microscope objective to gather light and resolve fine specimen detail at a fixed object distance.

Point Spread Function (PSF): The point spread function is defined as the image of a single point object, including the spreading/blurring due to components (filters, lenses) in the optical path. The image acquired by the microscope is the sum of the individual PSFs of an object. Each PSF measured represents a location and intensity corresponding to a point source.

Resolution: The ability of a microscope to distinguish between small objects or the minimum distance between distinguishable objects in an image.

Airy Disc: The bright region in the center of a diffraction pattern resulting from light passing through a uniformly illuminated circular aperture. The diameter of the center disc is related to the wavelength of the illuminating light and the size of the circular aperture. The criterion for resolving two objects is that the center of the first object Airy disc must be separate from the edge of the second object Airy disc (see Figure 1).

Pinhole: The pinhole aperture that is used to exclude light from out of focus focal planes. In laser scanning confocal microscopy, a pinhole in front of the light source can be used to direct the excitation light to a point/plane of the specimen. A second pinhole situated in front of the detector

is used to block the emitted light from adjacent focal planes above and below the point of interest. With spinning disk confocal microscopy, the same pinhole is used for the excitation and emission wavelengths. This is accomplished using a disc with multiple pinholes that is rotated at high speed. The backprojected pinhole radius used during deconvolution refers to the size of the pinhole as it appears in the specimen focal plane and is the physical pinhole size divided by the total magnification of the detection system (objective and internal magnifications). Optimal pinhole size is usually set as 1 Airy unit, or the diameter of the Airy disc, and gives the best signal-to-noise ratio. Pinhole spacing is a term used during deconvolution to define the distance between the backprojected pinholes of a spinning disk microscope.

Signal-to-Noise Ratio (SNR): A measure of the signal strength relative to the background noise. The higher the ratio, the more the desired signal is separated from undesirable background information.

Nyquist Sampling: Minimal sampling distance at which an image or signal must be recorded to ensure that all the signal information is represented in the measured sample. If a signal is undersampled, the fine details of an object are misrepresented as belonging to adjacent larger structures. Therefore, to ensure proper oversampling of an object, the following equations are used to determine minimum sampling distances in the lateral (xy) and axial (z) dimensions for confocal microscopy.

$$\Delta_{x,y} = \frac{\lambda_{ex}}{8n(\sin\alpha)}$$

$$\Delta_z = \frac{\lambda_{ex}}{2n(1-\cos\alpha)} \quad (1,2, \& 3)$$

$$\alpha = \sin^{-1}\left(\frac{NA}{n}\right)$$

where n is the refractive index, λ_{ex} is the excitation wavelength, and NA is the numerical aperture.

Table 1. Excitation and Emission wavelengths

Fluorophore	Excitation Wavelength (λ_{ex})	Emission Wavelength (λ_{em})
Cascade Blue	375	410
GFP	489	509
Cy2	489	506
Cy3	548	562
Cy5	650	670-700

Table 2. Refractive Index of Common Materials

Material	Refractive Index (n)
Air	1.0
Water	1.33
Oil	1.56

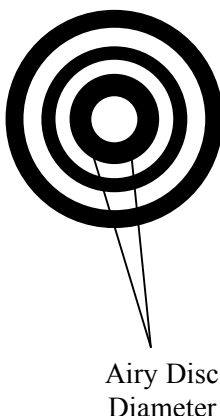


Figure 1. Airy Disc. Diffraction pattern of a point light source. The center bright spot is referred to as the Airy disc and is surrounded by multiple diffraction patterns. The diameter of the center spot is equal to one Airy unit.

TREGEI STARR

PROFESSIONAL GOALS

My research experience combines chemical engineering and cell biology disciplines with the purpose of understanding and developing computational models for the further study of intracellular processes. I am seeking a position that will allow me to combine my engineering and biological sciences experience in an open and exciting research environment.

EDUCATION

PhD Chemical Engineering

Virginia Polytechnic Institute and State University, Blacksburg, VA
Expected Graduation Date: May 2006

MENG Chemical Engineering

Virginia Polytechnic Institute and State University, Blacksburg, VA
December 2004

BS Chemical Engineering w/ Biotech Specialization

Illinois Institute of Technology, Chicago, IL
December 2001

PROFESSIONAL EXPERIENCE

July 2004

4th International Summer School on Biocomplexity: “From System to Gene” Dartmouth College Hanover, NH, participant

Responsibilities: Participated in a summer school program focused on exploring developing areas of bioengineering research.

Feb- Aug 2002

Virginia Polytechnic Institute and State University—Blacksburg, VA

Responsibilities: Worked as a general lab technician performing cell culture work, Western Blot analysis, cell fractionation, and radioactive binding studies.

May –Dec 2000 & May–Aug 2001

GE Plastics - Mt. Vernon, IN, Co-op student

Responsibilities: Acted as project leader for projects in both the chemical process and finishing operations. Maintained business objectives and goals while driving projects to completion. Used problem solving in a Six Sigma environment to accomplish goals in an efficient and timely manner.

May – Aug 1999

ARCO Alaska - Prudhoe Bay, AK, Internship

Responsibilities: Process chemical engineering intern at gas/oil separation flow-station on the North Slope, AK.

AWARDS/ SCHOLARSHIPS

1997 –2002: NEXT/ Camras Full Tuition Scholarship
1997 – 2001: Deans List
2002 – 2005: Davenport Graduate Fellowship
2003 – National Science Foundation Honorable Mention
2004 – Scholarship Recipient to 3rd International Summer School on Biocomplexity

PRESENTATIONS

Sung Rhee, Tregei Starr, Brian Storrie. “Quantitative Approaches to Image Analysis: Examples from the Golgi Apparatus” Arkansas Biosciences Symposium – *September 2005* (poster presentation)

Sung Rhee, Tregei Starr, Brian Storrie, Kimberly F. Williams. “Golgi enzymes have a steady state distribution of ~90:10 Golgi apparatus versus ER by both high resolution fluorescence microscopy and immunogold labeling” Annual Meeting American Society for Cell Biology (ASCB) – *December 2004* (poster presentation)

Tregei Starr, Brian Storrie, Kimberly F. Williams. “A Study Comparing Visualization Methods for Intracellular Proteins” American Institute of Chemical Engineers (AIChE) National Convention – *November 2003* (oral presentation)

Tregei Starr, Brian Storrie, Kimberly F. Williams. “A Study Comparing Visualization Methods for Intracellular Proteins” Southeastern Biomedical Engineering Conference (SBEC) - *September 2003* (oral presentation)

PUBLICATIONS

S. Rhee., T. Starr, K. Forsten-Williams, and B. Storrie. “The steady state distribution of glycosyltransferases between the Golgi Apparatus and the ER is ~90:10” Traffic 2005; 6: 1-13